# Probing Spins in Molecular Structures on Superconducting Surfaces

**Jung-Ching Liu**

Basel, 2024

Genehmigt von der Philosophisch-Naturwissenschaftlichen Fakultät
auf Antrag von:

Prof. Dr. Ernst Meyer
Prof. Dr. Martino Poggio
Prof. Dr. Katharina J. Franke

Basel, den 14. November 2023

Prof. Dr. Marcel Mayor, Dekan

To all the stories that touched my soul and inspired my own.

# Abstract

A quantum computer is considered to overtake classical computers from its ability of parallel information processing. However, qubits fabricated from quantum states are easily perturbed by their environment, leading to short decoherence time and limited gate operations. To extend decoherence time, qubits based on topological superconductivity are promising candidates thanks to their immunity against external perturbations. This dissertation aims on the fundamental understanding of condensed matter systems to realize topological superconductivity by targeting the observation of Majorana zero modes using low-temperature scanning probe microscopy. To accomplish this goal, we fabricate spin lattices *via* on-surface reactions on superconducting substrates (Nb and Pb). We first demonstrate the synthesis of atomically precise nanographenes on the superconducting Ag/Nb(110), and characterize their structures with atomic force microscopy at low temperatures. Our approach opens the route to couple $\pi$-magnetism to superconducting states. We then compare the spin signature of Fe atoms in the coordinated organometallic frameworks on Pb(111) and on Ag(111). On both substrates, we observe spin-flip excitations due to magnetocrystalline anisotropy. We last investigate an electron-spin superlattice fabricated by self-assembly of radical molecules on Pb(111). Using superconducting tips, we probe by tunneling spectroscopy Yu-Shiba-Rusinov states arising from the coupling of such spin-1/2 system with the superconductor. The observation of low-energy modes near boundaries of this two-dimensional magnetic island is consistent with the signature of Majorana zero modes.

# Content

# Contents

# Contents

# Introduction

Fast and enormous computer calculations are needed to address the complexity of systems that involve a huge number of parameters. From weather forecasting to the prediction of climate change, simulating molecules for drug discovery, or cryptology for cybersecurity, such simulations are beyond the scope of classical computers due to the impractical amount of time required.

In classical computing, the binary-code algorithm, which relies on the on-off operation of transistors, limits the capacity of the calculation process. To improve the computational performance, the semiconductor industry currently targets the miniaturization of the transistor size to increase their density for computer chips. This trend follows Moore's law–an empirical observation that the number of transistors in an integrated circuit is doubled every year, while the cost of computers is halved [1]. Nowadays, the smallest transistor in production is 3 nm in size [2]. This, however, is now challenging Moore's law, since a smaller transistor approaches the atomic size. This dimension confronts the problem of quantum tunneling, leading to the leakage of current and lose the on-off control on the transistor. To keep improving the computational power for vast calculations, a new type of computing is in urgent need.

In a quantum computer, quantum states, which rely on the superposition of two or more basic states, are used as bits. A quantum state has multiple statuses depending on the weight of each component. The superposition remains until a measurement is performed on the system. Different quantum states can couple with each other through interference or entanglement. With these properties, quantum states are considered as ideal candidates for bits (or *qubits*) of a quantum computer, expected to perform multiple-code algorithm that enables parallel computation of input values. The first qubit proposal was made by Loss and DiVincenzo [3], stating that spins are proper candidates as qubits, as an electron spin state can be viewed as the superposition of "spin-up" and "spin-down" basis states. Most importantly, spins confined in quantum dots (QDs) are able to be gated. In addition to spin-QDs, other quantum systems

have also been proposed as qubits, such as superconducting circuits [4] and trapped ions [5].

However, practical issues arise during the operation of quantum computing. As raised by DiVincenzo, seven criteria have to be fulfilled to bridge the gap between qubits and quantum information processing [6]. Among these criteria, scientists confront the problem of short decoherence time of qubits. Since operating Boolean gates relies on the coherent interaction between qubits, the tight coupling of the system to the environment causes superposition states to collapse due to external perturbations (such as electronic noise or radiation) [7]. The writing and reading cycles of qubits also need to be done within the decoherence time.

In search of qubits with long decoherence time, scientists target topologically protected quantum systems. Topologically protected states/modes emerge upon the realization of topological superconductivity (TSC), which have their experimental signatures of Majorana zero modes (MZMs). Majorana fermion were proposed by Ettore Majorana, which defines a particle being its own antiparticle [8]. In 2001, Kitaev proposed an one-dimensional (1D) model based on $s$-wave superconductivity that shows spinless fermions and unpaired MZMs at two ends of the chain, known as Majorana bound states (MBSs) [9]. This model has taken Majorana fermions, originally dedicated for neutrinos and cold dark matters in particle physics, to condensed matter systems, making it possible to be realized in the laboratory scale [10].

Majorana fermions are also non-Abelian anyons, meaning that they may form collective composite particles with degenerate ground states [7, 11]. Manipulating anyons and exchange their positions could lead to the hopping between degenerate ground states, which is known as the "braiding" process [7]. Non-Abelian exchange statistics makes MZM-bearing anyons potential media for topological qubits. Topological quantum computers are considered fault tolerant, since information is encoded nonlocally in quasiparticle states, making them robust against error caused by local disturbance [12]. Braiding gates based on the manipulation of anyons were proposed in several studies [12–14]. Its feasibility, however, remains elusive.

To realize TSC in condensed matter systems, Lutchyn *et al.* [15] and Oreg *et al.* [16] proposed that by combining spin-orbit coupling, superconductivity, and a Zeeman field in the solid-state system, an equivalent spinless chain is able to be generated. Based on this model, the first observation of MZMs was demonstrated in the hybrid system of a superconductor and a semiconducting nanowire [17]. In addition to this prototype, atomic spin chains on a $s$-wave superconductor have been found to exhibit spinless $p$-wave pairing [18–22].

The study of such exotic spin-spin and spin-substrate coupling at the atomic scale requires high spatial and energy resolution. Scanning probe microscopy (SPM) thus plays an important role in the realization and investigation of TSC. Atomic force microscopy (AFM) is able to resolve the surface topography in atomic scale by detecting forces acting in the tip-sample junction [23]. With the implementation of a tuning fork sensor and a CO-terminated tip at low temperatures, chemical bonds of organic mole-

cules or nanostructures can be further revealed [24,25]. Scanning tunneling microscopy (STM) was invented based on the quantum tunneling effect, which can also reconstruct the surface morphology with atomic resolution [26]. Scanning tunneling spectroscopy (STS) is able to probe local electron density of states [27], unveiling signatures of spin-spin and spin-substrate coupling. Furthermore, SPM also enables tip manipulation of atoms or molecules, and thus the *in situ* build-up of nanostructures. In recent studies, charge state control of a molecule has been achieved by using the local electric field of a SPM-tip [28–30], opening the use of single molecules as QDs. Therefore, SPM is an incontrovertible tool to disentangle structural and electronic properties of nanostructures on surfaces. In this context, its use to construct and characterize TSC is ubiquitous.

In this dissertation, we focus on the investigation of the coupling between a single spin/spin lattice with a normal metal/superconductor using SPM, namely STM and AFM. Chapter 1 introduces concepts and technical background of SPM. Chapter 2 covers the physical concepts closely relevant to the thesis: (1) the fabrication of spin lattices, (2) different magnetism origins, and (3) the behavior of magnetic moments on different surfaces and their exchange interactions *via* the substrate. Chapter 3 describes specification of the microscopes used in this work, and details about the sample preparation. In Chapter 4, we demonstrate the first direct synthesis of atomically precise nanographene on a superconducting substrate. In Chapter 5, we fabricate a magnetic lattice through the coordination between small organic molecules and transition metal elements (Fe). The resulting organometallic structure and the spin-flip excitations observed on normal metal and on a superconductor are discussed. Chapter 6 presents islands of molecular electron acceptors prepared on a conventional superconductor, on which we find signatures of topologically protected edge modes.

# 1

# Scanning Probe Microscopy

With the progress in the research of quantum physics, microscopes based on quantum phenomena were developed to examine interactions in the atomic/molecular level in real space with high spatial resolution and surface sensitivity. This microscopic technique is known as *scanning probe microscopy (SPM)*. In addition to the microscopic function, the spectroscopic operation of SPM is able to probe local electronic properties or distinguish different types of elements on the surface. Moreover, due to the atomic resolution, SPM is also considered as an efficient tool to manipulate atoms or molecules on the substrate. In this chapter, we will introduce the working principle and recent progress of two SPM techniques – scanning tunneling microscopy and atomic force microscopy.

## 1.1 Scanning Tunneling Microscopy

The first tunneling experiment was performed by Binnig, Rohrer, Gerber, and Weibel in 1982 [26], demonstrating the feasibility to measure tunneling current from a metallic substrate through a controllable vacuum junction thickness. The technical success in tunneling current measurement paved the way to the invention of scanning tunneling microscopy (STM), which acquired the first topographic images of $CaIrSn_4(110)$ and $Au(110)$ in 1982 [31]. Moreover, the real space atomic resolution image obtained by STM reveals the silicon (Si) (111)-($7 \times 7$) surface reconstruction that has long puzzled experimental measurement and theoretical modeling due to its large unit cell [32]. With the development of STM, Binning and Rohrer were awarded the Nobel Prize in Physics in 1986 [33].

Following pioneering results in 1980s, STM was later applied to a variety of research in surface sciences. For instance, the STM investigation on the $TiO_2(110)$ surface shows the diffusion of oxygen vacancies at elevated temperatures [34]. With high spatial resolution, the ability of atom manipulation with a STM tip was first demonstrated

by moving xenon atoms on the cold Ni(110) surface [35], followed by building artificial atoms by constructing quantum corrals [36].

In this section, the numerical approximation of the tunneling effect will first be introduced. A brief description of STM operation and the implementation of the ultra-high vacuum system to STM will also be discussed.

## 1.1.1 Quantum tunneling
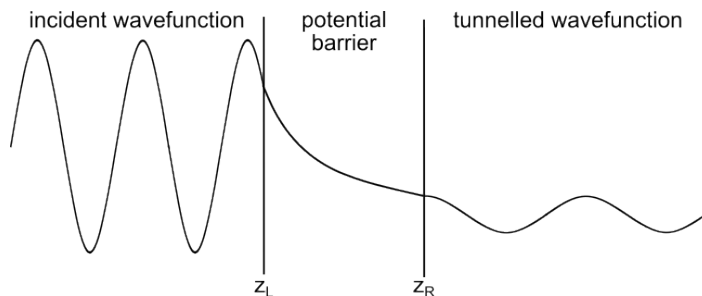


**Figure 1.1:** *A scheme illustrating quantum tunneling through a 1D potential barrier. The incident wavefunction decays exponentially in the potential barrier. The remaining wavefunction at the other side of the barrier generates a probability for the particle to tunnel through.*

The basis of STM lies in the detection of the tunneling current. The quantum tunneling effect occurs when an incident particle confronts a potential barrier (Fig. 1.1). The incident wavefunction carried by the particle decays exponentially across a thin potential barrier while a large portion is reflected. The remaining wavefunction at the other side of the barrier leads to a probability for the particle to tunnel through due to the particle-wave dualism.

Based on the first order of Bardeen's approximation, Tersoff and Hamann developed a theoretical approach to simulate tunneling effect in STM. The tunneling current is expressed as following [37]:

$$I = \frac{2\pi e}{\hbar} \sum_{t,s} f(E_t)[1 - f(E_s + eV)]|\mathcal{M}_{ts}|^2 \delta(E_t - E_s), \qquad (1.1)$$

where $f(E)$ is the Fermi-Dirac distribution $f(E) = \frac{1}{1+e^{E/kT}}$, $V$ is the applied bias, $\mathcal{M}$ is the tunneling matrix between states of the tip ($\varphi_t$) and the sample surface ($\varphi_s$), $E_{t,s}$ is the energy of state $\varphi_{t,s}$ without tunneling, and the delta function describes the conservation of energy for elastic tunneling. With the assumption of small applied bias, low temperature and a *s*-wave dispersion of a point probe (Fig. 1.2), the tunneling current can be re-written as [37]:

$$I \propto \sum_{s} |\varphi_s(\vec{r_0})|^2 \delta(E_s - E_F), \qquad (1.2)$$
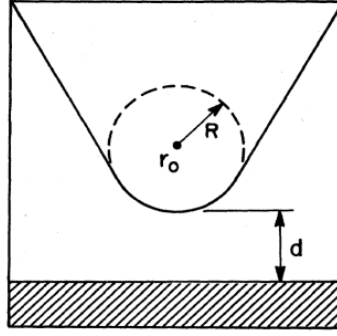
**Figure 1.2:** *The simplified tunneling geometry proposed by Tersoff and Hamann.* *The Tersoff-Hamann approximation for the tunneling current is based on a locally spherical tip with s-wave approximation. Reprinted with the permission from [37].*

describing the tunneling current with the tip at position $\vec{r_0}$. In Equ. 1.2, by definition, the right-hand-side corresponds to the local density of states (LDOS) at $E_F$ of the sample surface at the tip position $\vec{r_0}$ ($\rho_s(\vec{r_0}, E_F)$). It can be thus concluded that the tunneling current is only proportional to surface LDOS at a certain tip position, and the information STM acquires is a contour of LDOS of the surface.

In addition, in Equ. 1.2, $\varphi_s(\vec{r_0})$ is the surface wavefunction at $\vec{r_0}$, which decays exponentially with the in $z$-direction normal to the surface [38], meaning that

$$\varphi_s(\vec{r}) \propto e^{-\kappa z}, \tag{1.3}$$

where $\kappa = \sqrt{2m\phi}/\hbar$ is the inverse decay length of the wavefunction in vacuum, and $\phi$ is the work function. Then, the charge density at $\vec{r_0}$ with $R$ the radius of the point probe, and $d$ the rip-sample distance can be found as:

$$|\varphi_s(\vec{r_0})|^2 \propto e^{-2\kappa(R+d)}. \tag{1.4}$$

Therefore, the tunneling current, being proportional to the surface LDOS, also decays exponentially with respect to the distance $z = R + d$:

$$I \propto e^{-2\kappa z}. \tag{1.5}$$

In the same publication, Tersoff and Hamann applied this numerical method to simulate the $(2 \times 1)$ and $(3 \times 1)$ reconstructions Au(110), and found nice agreement with the experimental results acquired by Binning *et al.* [37, 39].
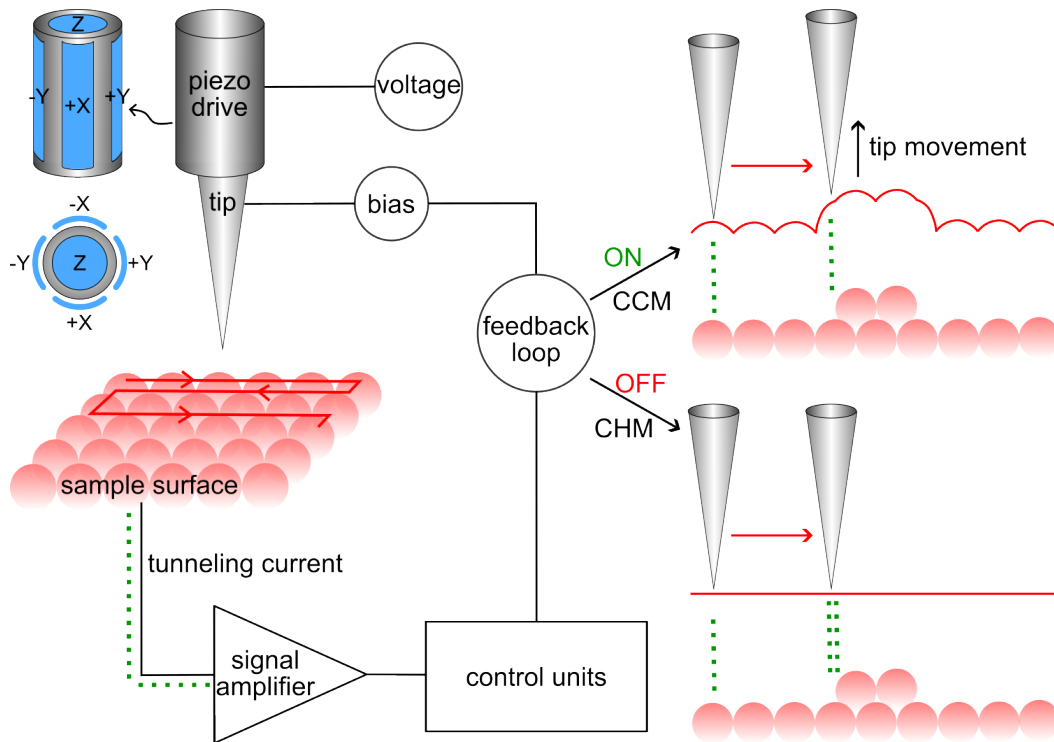
**Figure 1.3:** *A scheme that shows critical components for scanning and operation modes of STM. The position of the STM tip is controlled by a piezo drive, whose shape is determined by the voltage applied on five pieces of piezoelectric materials. During scanning, the CCM and CHM are two modes used for acquiring STM images with and without the feedback loop.*

## 1.1.2 Operation of STM

Figure 1.3 is the scheme that shows critical components for obtaining a STM image. The tip scans across the sample surface line by line and pixel by pixel. The movement of the tip is driven by a cylinder attached with five pieces of piezoelectric materials. Since the dimension of a piezoelectric material can be tuned by the magnitude and polarity of the applied voltage, the shape of the cylinder and thus the tip position are changed accordingly. During the scan, a bias is usually applied to either the tip or the sample to enhance the tunneling effect. The consequent tunneling current then passes through an amplifier to magnify the signal, which is then sent to the controlling electronics for processing and displaying.

The feedback loop is a built-in function of control units, which gives two operation modes for probing the surface morphology according to its on/off status (right half of Fig. 1.3). First, in constant height mode (CHM), the feedback loop is switched off and the tip stays at the same height through the scanning process. The topography is then reconstructed based on different amount of tunneling current detected at each pixel. In CHM, there is a high demand for the flatness of the surface, since the tip is subject to damage while encountering bulky protrusions without the feedback loop.

Another operation mode is constant current mode (CCM), and it is commonly used for acquiring STM images. CCM is operated with the feedback loop, which enables tip movement according to the surface roughness to maintain the current setpoint ($I_t$). The topography is reconstructed by tracing the tip position in this mode.

### 1.1.3 Ultra-high vacuum system

In order to prevent surface oxidation, an ultra-high vacuum (UHV) system is usually implemented for SPM, enabling the vacuum level below $1 \times 10^{-9}$ mbar. Typically, a microscope is divided into several chambers, each of which has a different vacuum level and is separated from one another by a valve (see Section 3.1-3.3 for the specification of different microscopes). To reach UHV, a "bake-out" process of chambers at about 130°C is first performed to remove water vapor. Simultaneously, different types of pumps are operating to reach UHV. First, a primary pump is applied to reduce the chamber pressure from 1 atmosphere to about $10^{-2}$ mbar, followed by the operation of turbo molecular pumps which enables the pressure in the range of $10^{-9}$ mbar. In the chamber for sample analysis, a higher demand of the vacuum level can be attained by a ion getter pump which can reduce the pressure to $10^{-10}$ mbar or even lower. In addition, in the chamber for sample preparation, the pressure may worsen due to the frequent sample preparation. An additional titanium sublimation pump can be applied to capture residual gas molecules to recover UHV. The instantaneous pressure is readout by the ionization gauge.

## 1.2 Scanning Tunneling Spectroscopy

In addition to probing the surface topography, STM can also acquire information of local electronic properties by applying its spectroscopic function, which is *scanning tunneling spectroscopy (STS)*. To perform STS, the tip is parked above the target position at a fixed height, and a bias sweep is applied on either the tip or the sample. The amount of the tunneling current is detected at each bias value. In acquired $I - V$ curves, a sharp increase of the current means that an additional tunneling channel is available under a certain bias, indicating a state at the corresponding energy. The local differential conductance can be obtained by applying a lock-in amplifier, which modulates the bias and demodulates the detected tunneling current. The obtained conductance spectra directly reflect LDOS, known as *differential conductance spectra* or *dI/dV spectra* (Fig. 1.4a).

The lock-in technique also enhances the signal-to-noise ratio of the STS measurement. A lock-in amplifier superimposes a sinusoidal alternating current (AC) voltage modulation $V_r = V_m cos(\omega_r t)$ ($V_m$ is the modulation amplitude, and $\omega_r$ is the modulation frequency) to each applied bias of the sweep [40]. The input signal embedded with noise $V_s = Rcos(\omega_s t + \theta_s)$ is sent to the signal mixer for the multiplication with the reference signal that has the frequency $\omega_r$. By demodulating the detected tun-

neling current, only the signal and noise at frequency $\omega_r$ remain [41]. Cleaner $\mathrm{d}I/\mathrm{d}V$ signals can be obtained by applying proper low-pass filter. Note that the tunneling current also responds to the AC component of the bias, thus the choice of $V_m$ is critical as a large voltage modulation could hamper the visibility of states that have small width. The instrumental contribution in the lineshape broadening is known as *lock-in broadening.*

Although in Equ. 1.2, the tunneling current is only proportional to the surface LDOS, the tip DOS ($\rho_t$) can also modify the tunneling current given that the assumption of Tersoff-Hamann approximation is not applicable. For instance, in the case that a non-*s*-wave tip is used, or a large bias is applied. By taking $\rho_t$ into account, the experimental $\mathrm{d}I/\mathrm{d}V$ spectra are the convolution of $\rho_t$ and the $\rho_s$ [38, 42]:

$$
\begin{aligned}
\frac{dI}{dV}(V) \propto\; & e\rho_t(0)\rho_s(eV)T(eV, eV) \\
& + \int_0^{eV} \rho_t(\pm eV \mp E)\rho_s(E)\frac{dT(E, eV)}{dV}dE,
\end{aligned}
\tag{1.6}
$$

where $V$ is the applied bias, and $T$ is the transmission coefficient. The transmission coefficient has a monotonic increase as the bias increases [38]. Thus the first term in Equ. 1.6 dominates the spectral lineshape at a fixed tip position.

The surface DOS as a function of position can be mapped by collecting $\mathrm{d}I/\mathrm{d}V$ signal at a fixed applied bias, and moving the tip pixel-by-pixel and line-by-line through the surface in the constant height mode. The acquired DOS distribution image is called
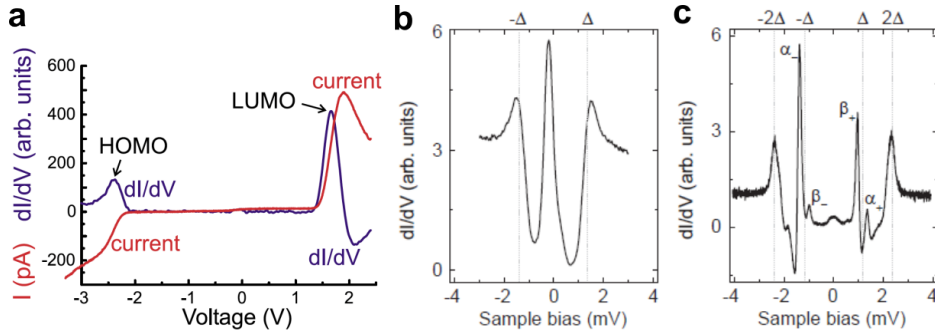


**Figure 1.4:** *Exemplary d$I$/d$V$ spectra measured with a metallic tip and a SC tip. **a,** The d$I$/d$V$ spectrum measured on a pentacene molecule adsorbed on the NaCl/Cu(111) substrate with a metallic tip at 5 K. The spectrum clearly resolves the highest occupied molecular orbital (HOMO) and the lowest unoccupied molecular orbital (LUMO) of the molecule. Reprinted with the permission from [27]. **b,** The d$I$/d$V$ spectrum measured on a Mn adatom on the superconducting Pb(111) with a metallic tip at 1.2 K. The metallic tip DOS smears out the resolution of in-gap states. **c,** The same sample as **b** but measured with a SC-tip at 4.8 K. The superconductivity DOS can largely enhance the visibility of small energy states ($\alpha_\pm$ and $\beta_\pm$ in the spectrum). **b-c** reprinted with the permission from [43].*

the *differential conductance map* or *dI/dV map*. By setting the applied bias at which a conductance peak arises, the corresponding atomic/molecular state orbital can be directly imaged [27].

Note that the working temperature can also cause linewidth broadening given that either the tip or the sample is metallic. Since Fermi-Dirac distribution tends to broaden at an elevated temperature, thermal-excited electrons at the Fermi edge could contribute to the tunneling event to a certain state, which could smear out the resolution of the $dI/dV$ spectrum [44]. This unwanted contribution by thermal-excited electrons is known as the *thermal broadening effect.* To consider the thermal broadening effect, one has to further convolve the Fermi-Dirac function to Equ. 1.6.

Due to thermal broadening and instrumental constraints, the emergence of small energy states may be hindered from the spectra with the usage of a metallic tip, since a metal is subject to the thermal broadening effect. To circumvent the limitation of temperature, the implementation of a superconducting tip (SC-tip) could be a solution. The DOS of a superconductor exhibits sharp coherence peaks and particle-hole symmetry, it is thus an ideal tip material to enhance the energy resolution of superconducting samples. Figures 1.4b, c show a stark contrast in energy resolution between the application of a metallic tip and a SC-tip. By measuring with a SC-tip (Fig. 1.4c), in-gap states generated on a magnetic adatom on a superconductor (see Section 2.3.3 for theoretical details) can be clearly resolved at 4.8 K comparing to the 1.2 K measurement with a metallic tip (Fig. 1.4a) [43].

## 1.3 Atomic Force Microscopy

In 1986, atomic force microscopy (AFM) was first demonstrated by Binnig, Quate, and Gerber [23], and was awarded the Kavli Prize in Nanoscience in 2016 for its versatile scientific investigation in the field of physics, chemistry, biology, and materials science [45]. AFM probes the sample surface by detecting forces acting in the tip-sample junction. The atomic resolution AFM image acquired on the Si(111) surface under UHV also shows $(7 \times 7)$ reconstruction, which confirms the result of STM [32,46].

While the tunneling current is monotonic with respect to the distance (Equ. 1.5), there are multiple forces acting at the tip-sample junction in AFM, and each of them behave differently with respect to the distance [25]. The force component responsible for atomic resolution is only relevant at small distance regime and is highly sensitive to the change in distance. To extract this force component, a phase-locked loop (PLL) is required.

In this dissertation, we target the investigation of organic molecules or nanostructures. To better resolve chemical bonds, we utilize a variation technique of AFM – the frequency-modulation AFM. In this section, we first introduce different forces arising in the atomic scale, followed by a focus on the working principle of the frequency-modulation AFM and the functionalization of the tip that further enhances the image

resolution.

## 1.3.1  Force interaction in the tip-sample junction
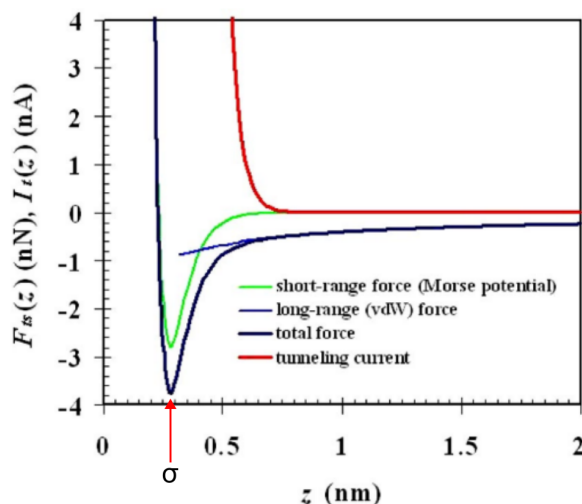


**Figure 1.5:** *Graph of the distance dependency of the tunneling current and forces acting at the atomic scale. The long-range force has a minor change with respect to the tip-sample distance. On the contrary, in the distance of few angstroms, the short-range force changes abruptly in magnitude and direction, and thus contributes to the atomic resolution. The local minima of the total force curve marks the "equilibrium distance" ($\sigma$). Adapted with the permission from [47].*

The force curve in Fig. 1.5 describes the trend of the different forces with respect to the tip-sample distance $z$. The negative force marks the attractive component, while the positive force represents the repulsive interaction. Forces at the atomic scale can be divided into two contributions: long-range and the short-range forces. Long-range forces include van der Waals (vdW) force, electrostatic, and magnetic forces, which exist in a large range up to 100 nm [47]. Short-range forces becomes relevant within the tip-sample distance of only few angstroms, referring to chemical bonding forces.

The total force can be described by Lennard-Jones potential under the criterion of two charge neutral atoms or molecules [47]:

$$V_{LJ}(z) = -E_{bond}(2\frac{\sigma^6}{z^6} - \frac{\sigma^{12}}{z^{12}}), \tag{1.7}$$

thus the tip-sample force ($F_{ts}$) can be derived as

$$F_{ts}(z) = \frac{-\partial V_{LJ}}{\partial z} = \frac{12E_{bond}}{\sigma}(\frac{\sigma^{13}}{z^{13}} - \frac{\sigma^7}{z^7}), \tag{1.8}$$

where $E_{bond}$ is the bonding energy, and $\sigma$ is the equilibrium distance which locates at the minima of the force curve (Fig. 1.5). From Equ. 1.7, the component $z^{-6}$ refers to the attractive force (which has the vdW force as the major contribution), and the $z^{-12}$ indicates the repulsive one. The vdW force is mainly the result of the interaction between induced dipoles, known as London interaction. Following the statement above, the atom-atom vdW pair potential can be expressed as the following [48]:

$$V_{vdW}(z) = -\frac{C}{z^6}, \tag{1.9}$$

where $C$ is the coefficient of the atom pair potential. Here, $C$ is determined by the *Hamaker constant* $A_H = \pi^2 C \rho_1 \rho_2$ ($\rho_1$ and $\rho_2$ are the atom densities of the two bodies). By taking the derivative, the vdW force ($F_{vdW}$) is

$$F_{vdW}(z) = -\frac{6C}{z^7}. \tag{1.10}$$

However, the Hamaker constant is further dependent on the geometry and the material of the considered system [48]. For instance, a spherical tip results in a proportional relation to $1/z^2$, and a pyramidal tip gives a $1/z$ relation [49].

In the case of a conducting tip and sample, the electrostatic force has to be taken into account. Consider a spherical tip with radius $R$ [50]:

$$F_{el}(z) = -\frac{\pi \epsilon_0 R U^2}{z}, \tag{1.11}$$

where $\epsilon_0$ is the vacuum permittivity and $U$ the electrostatic potential difference.

From Fig. 1.5, the short-range force becomes relevant when the tip-sample distance is less than 1 nm. At such short distance, the overlap of sample and tip wavefunctions leads to the formation of covalent bonds, and the force required to break the bond is the chemical bonding force. As shown in the force curve, the chemical bonding force experiences an abrupt change with a minimal change in the distance. Thus, it is the main contribution to the atomic resolution of AFM. The chemical bonding force ($F_{chem}$) can be derived from the Morse potential [47]:

$$F_{chem}(z) = \frac{-\partial E_{chem}}{\partial z} = -2E_{bond}\kappa(e^{-\kappa(z-\sigma)-e^{-2\kappa(z-\sigma)}}), \tag{1.12}$$

with $\kappa$ the decay length. However, in the regime $z < \sigma$, the repulsive electrostatic force from the inner shell electrons comes to effect, leading to a rapid switch of the total force from the attractive to the repulsive interaction.

In addition to atomic resolution, AFM also possess chemical identification [51] and the charge state resolution [52], since the force interaction differs from element to element even with the identical tip-sample distance.

## 1.3.2 Operation of AFM

Two common operation modes of AFM are the amplitude-modulation (AM) and the frequency-modulation (FM) modes. In the AM-AFM mode, or the *tapping mode*, the cantilever is driven by a shaker piezo and oscillating at a constant frequency with an amplitude setpoint $A_{set}$. Due to the force acting at the tip-sample junction, the change in the oscillation amplitude is sent to the feedback loop to maintain $A_{set}$. The amplitude shift is monotonic to distance in the operation range $z \gtrsim \sigma$, and is relatively simpler in the extraction of surface topographic information [25]. AM-AFM is thus the widely used AFM imaging technique in the ambient condition.

The FM-AFM mode relies on the shift of oscillation frequency from the eigenfrequency of the cantilever $f_0 = \frac{1}{2\pi}\sqrt{k/m^*}$, where $k$ is the spring constant of the cantilever. A PLL is used to keep the cantilever oscillating at $f_0$ with a constant amplitude $A$. Given that the oscillation amplitude is much smaller then the force interaction range ($A \ll \lambda$), the frequency shift of the cantilever is proportional to the force gradient [25]:

$$\Delta f = f_0 \frac{k_{ts}}{2k} = f_0 \frac{-\partial F_{ts}}{\partial z}, \tag{1.13}$$

where $k_{ts}$ is the spring constant of the tip-sample junction. On the contrary, if a large oscillation amplitude is considered ($A > \lambda$), the normalized frequency shift $\gamma_{ts} \approx 0.4 F_{ts}\sqrt{\lambda}$ is involved [25]:

$$\Delta f = f_0 \frac{k_{ts}}{k} \frac{1}{A^{3/2}} \gamma_{ts}. \tag{1.14}$$

Similar to AM-AFM, FM-AFM usually operates at tip-sample distances $z \gtrsim \sigma$, which falls in the attractive force regime with $\Delta f < 0$ (see Equ. 1.13).

Based on the FM-AFM, Giessibl *et al.* developed a qPlus sensor, which is composed of a tip attached on a tuning fork made of piezoelectric quartz, making it possible to perform STM and FM-AFM with the same microscope [25]. In this thesis, bond-resolved AFM images of organic molecules are acquired with a qPlus sensor under the operation of FM-AFM.

## 1.3.3 CO-functionalized tip

The Tersoff-Hamann approximation points out that the surface topography acquired by STM is proportional to LDOS with the assumption of a $s$-wave tip state (see Section 1.1.1). A general approximation considering different tip states was proposed by Chen as the *derivative rule*, which suggest that a $p$-wave tip state is able to probe the spatial gradient of the surface wavefunction [54,55].
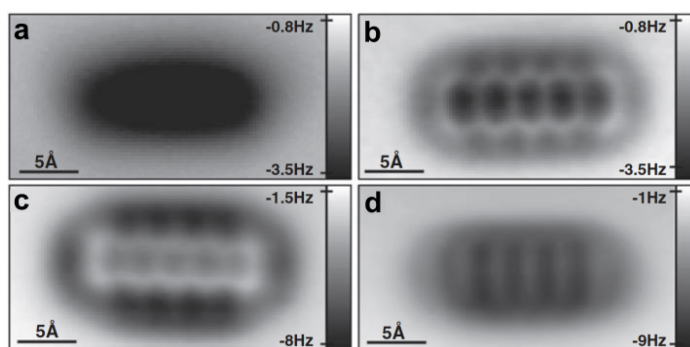
**Figure 1.6:** *Images acquired by FM-AFM show different contrast with different tip terminations. **a,** A pentacene molecule deposited on the NaCl/Cu(111) substrate probed with a Ag-tip. **b,** The same molecule probed with a CO-tip. **c,** The petacene molecule probed with a Cl-tip. **d,** The image acquired by a pentacene-tip. **a-d** reprinted with the permission from [53].*

Functionalizing the tip with a molecule is an efficient way to modify the tip wavefunction from the metallic $s$-wave tip to other tip sates. The STM image of a CO-terminated tip (CO-tip) exhibits the $p$-wave nature of the tip, since $2\pi^*$ degenerate states are the frontier states of a CO molecule and significant tunneling events occurs to these states [24]. With regard to the FM-AFM measurement, the $p$-wave nature of the CO-tip is also found to have the optimal chemical bond resolution. As demonstrated by Gross *et al.* [53], bond resolution of an organic molecule acquired by FM-AFM with a CO-tip is greatly enhanced (Fig. 1.6b), comparing to a metallic $s$-wave tip (Fig. 1.6a) or other tip terminations (Figs. 1.6c-d). The ideal geometry of a CO-tip lies in the vertical position of CO with respect to the sample surface. A canted CO molecule could change the bond length in an AFM image [56].

## 1.4  Summary

As the main investigation method of this thesis, this chapter discusses the theoretical background of SPM as well as a general description of SPM operation. The ground breaking invention of STM allows the visualization of the sample surface with atomic resolution. By performing STS, information of local electronic properties can be obtained, which reveals intriguing physical properties. AFM is another atom-resolved imaging technique that provides chemical information by measuring the force curves. To better resolve organic molecules, FM-AFM is developed with the application of a qPlus sensor. Decorating a CO molecule at the tip apex during the FM-AFM measurement, chemical bonds can be clearly visualized through probing with a $p$-wave tip state.

# 2

# Spins on Surfaces

$\mathrm{N}$OISE and external disturbance are known to be the largest challenges in quantum computing. A novel type of qubits that are protected by topology could largely extend their decoherence time. These so-called *topological qubits* has their scientific fundament in topologically protected edge states/modes in hybrid systems combining ferromagnets and conventional superconductors. The understanding of the interplay between spin lattices and superconductivity is thus in urgent need.

In this chapter, approaches for the fabrication of spin lattices will be discussed, followed by the introduction of three sources of magnetism: orbital magnetism contributed by transition metal elements, spins in carbon-based aromatic nanostructures due to unpaired $\pi$-electrons, and spins arose from molecular electron acceptors. Interactions between spins and normal metals and superconductors are then discussed. In the last section, the concept of topological superconductivity is briefly introduced, as it is an exotic physical property that could emerged from the coupling between magnetic moments and superconducting states.

## 2.1 From Single Spins to Spin Lattices

Possessing the spatial resolution down to atomic level, manipulating magnetic adsorbates with a SPM tip is an intuitive approach to construct a spin lattice [57]. Due to the time-consuming operation and the lattice restriction from the underlying substrate, we seek for methods that can build ordered spin structures with higher flexibility and convenience. On-surface reaction is a bottom-up approach to fabricate nanostructures with atomic precision. Here, we focus on the strategies to fabricate ordered spin structures with different on-surface reactions using pre-designed molecule precursors.
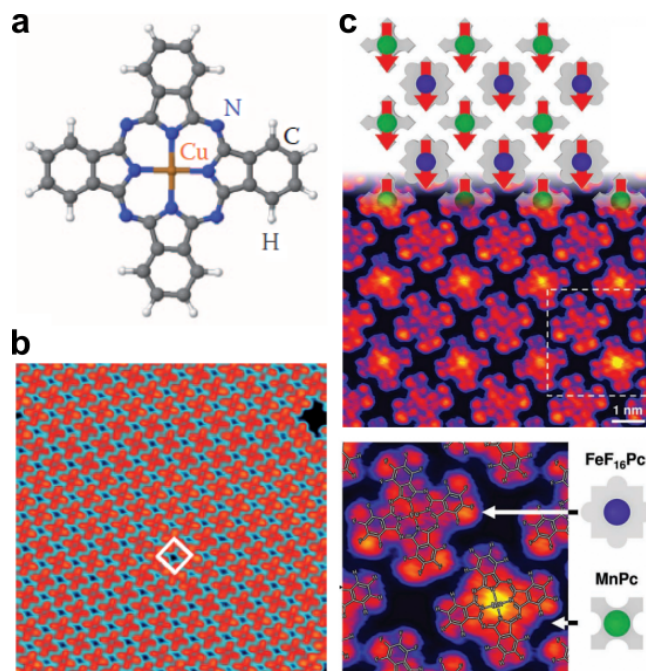
**Figure 2.1:** *Self-assembly of different MPc molecules on normal metal substrates. **a,** The chemical structure of a CuPc molecule. **b,** The self-assembled CuPc monolayer on the Ag(100) surface. Reprinted with the permission from [58]. **c,** The co-deposition of $FeF_{16}Pc$ and MnPc on the $c(2 \times 2)$ oxygen-reconstructed Co(001) surface forms a chessboard-like assembly through hydrogen-bonds. Reprinted with the permission from [59].*

## 2.1.1 Designing supramolecular and covalent spin lattices

**Self-assembly of magnetic atoms.** An approach to arrange single spins is to attach ligands to transition metal ions and form magnetic molecules. Such magnetic molecules are able to sustain their structure at the sublimation temperatures in UHV. Upon the deposition on the substrate, magnetic molecules spontaneously form an ordered monolayer through the van der Waals interaction, with the assembly pattern following the substrate registry [63, 64]. Metal phthalocyanine (MPc), which is composed of a transition metal ion core and an aromatic macrocyclic ligand (see CuPc in Fig. 2.1a as an example), is one of the well-studied magnetic molecules on surfaces [58,59,63,65,66]. In addition to single MPc molecule assemblies (Fig. 2.1b) [58], co-evaporating two types of MPc with different core ions and modified ligands can also form a self-organized "chessboard" pattern (Fig. 2.1c) [59]. However, the weak van der Waals or hydrogen-bond interactions, which are the main binding mechanisms in molecular assemblies, could alter the reaction pathway comparing to the much stronger covalent bonding [67].

**Organometallic (OM) coordination.** Coordination chemistry is another approach to form spin lattices. Organic molecules with negatively charged functional groups are able to coordinate with transition metal ions and organize spins into ordered magnetic
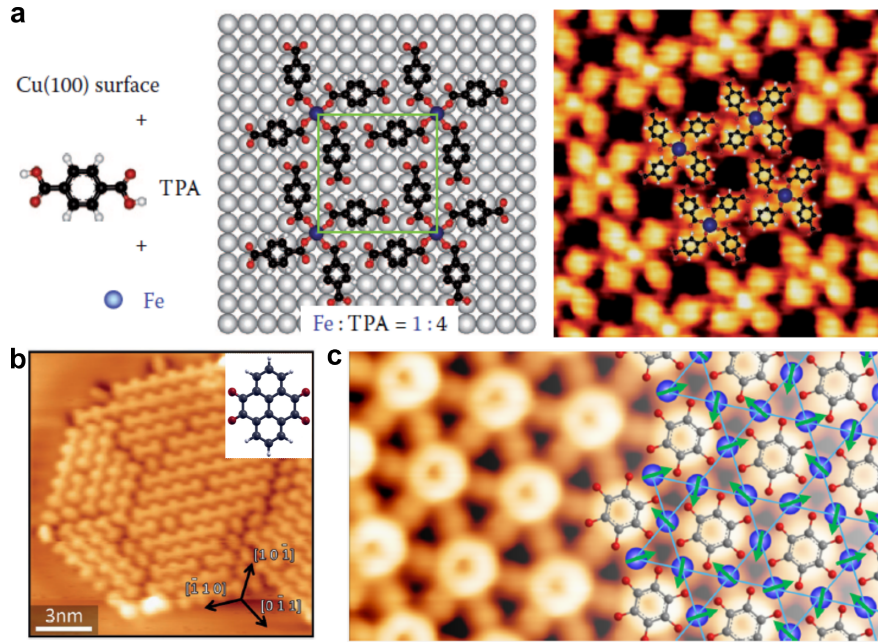
**Figure 2.2:** *OM networks through the coordination of transition metal ions with organic molecules.* **a,** *Clover-shaped motifs is composed of a Fe and four terephthalic acid molecules on Cu(111), which further self-assemble into a 2D network. Reprinted with the permission from [60].* **b,** *A grid of 1D magnetic chain can be fabricated by coordinating Fe with pyrene-4,5,9,10-tetraone (shown in the inset) on Cu(111). Reprinted with the permission from [61].* **c,** *A Kagome lattice of Fe on Au(111) is synthesized with the coordination with benzene-1,2,3,4,5,6-hexaol molecules. Reprinted with the permission from [62].*

networks. Such functional groups include charged atoms like $O^{2-}$, $S^{2-}$, $Cl^-$, or groups with electron doners, such as $OH^-$ [68]. These functional groups provide directional bonding with metal ions with a moderate strength that leads to certain morphologies [67]. Factors such as different combinations of metal ions and functional groups, intermolecular interactions, and the coupling with the substrate have to be taken into account to determine the structural and electronic properties of the OM network.

Due to the small steric hindrance of the peripheral functional groups, it is possible that one transition metal ion coordinate with multiple molecules, which can further self-assemble into a monolayer through hydrogen-bonds (Fig. 2.2a) [60, 69]. A grid of 1D magnetic chains with reduced magnetic moments on each metal ion site (Fig. 2.2b) [61], or a Kagome magnetic lattice exhibiting spin frustration (Fig. 2.2c) [62] can also be fabricated through coordination chemistry.

**Covalent spin structures.** Ullmann coupling is one of the well-known on-surface reactions to synthesize carbon-based nanographenes (NGs) and graphene nanoribbons (GNRs). Since the synthesis of atomically precise GNRs on Au(111) in 2010 (Fig. 2.3b) [71], the bottom-up fabrication of NGs has become popular for synthesiz-
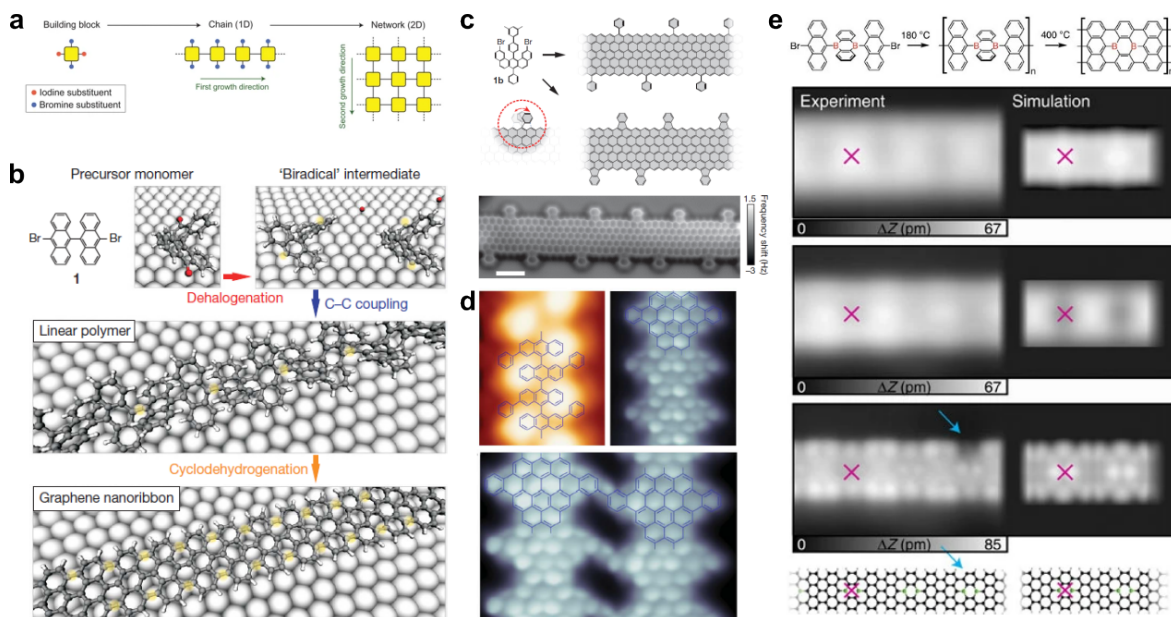
Figure 2.3: *Different GNR morphologies obtained by Ullmann coupling. a,*
*A scheme explaining the pathway of Ullmann coupling, which start from single molecule*
*precursors to a 1D or 2D framework via thermal treatment. Reprinted with the per-*
*mission from [70].* ***b,*** *7-carbon-wide armchair GNRs can be synthesized by subliming*
*10,10'-dibromo-9,9'-bianthracene molecules on Au(111) and undergoing two stages of*
*annealing. Reprinted with the permission from [71].* ***c,*** *Synthesis and the AFM im-*
*age of an edge-modified 6-carbon-wide zigzag GNR. The scale bar is 1 nm. Reprinted*
*with the permission from [72].* ***d,*** *Different synthesis stages of a nanoporous graphene.*
*Reprinted with the permission from [73].* ***e,*** *The reaction pathway and structural char-*
*acterization at different tunneling conditions of B-doped armchair GNRs. Reprinted*
*with the permission from [74].*

ing complex graphene structures [75], comprising well-defined edges (Fig. 2.3c) [72],
topological defects (Fig. 2.3d) [73, 76], or hetero-atomic dopants down to the single
atom limit (Fig. 2.3e) [74]. Such on-surface reaction requires the sublimation of pre-
defined halogenated organic precursors in ultra-high vacuum (UHV) onto crystalline
substrates, followed by a thermally triggered surface-assisted polymerization. The
crucial part of the polymerization is to initiate dehalogenation, which leads to the
formation of organometallic intermediates. A subsequent annealing releases precursor
radicals and enforces cyclodehydrogenation processes.

The morphology of the final reaction product depends on the type of halogen atoms
on the initial precursors and the choice of the substrate. Due to high stability of some
halogen substituents (such as chlorine), cyclodehydrogenation could take place within
the precursor prior to dehalogenation, and deviates the reaction from the conventional
Ullmann coupling [77]. In addition, the different reactivity of substrates (Cu(111)
> Ag(111) > Au(111) for instance) leads to different alignment patterns after the
sublimation of the same precursor. Later, this leads to different reaction products

after thermal treatments [71, 78–80]. Other than these thermodynamic causes, kinetic factors such as the heating rate is also possible to deviate the final product from the conventional reaction pathway [81].

## 2.1.2 Magnetism with different mechanisms
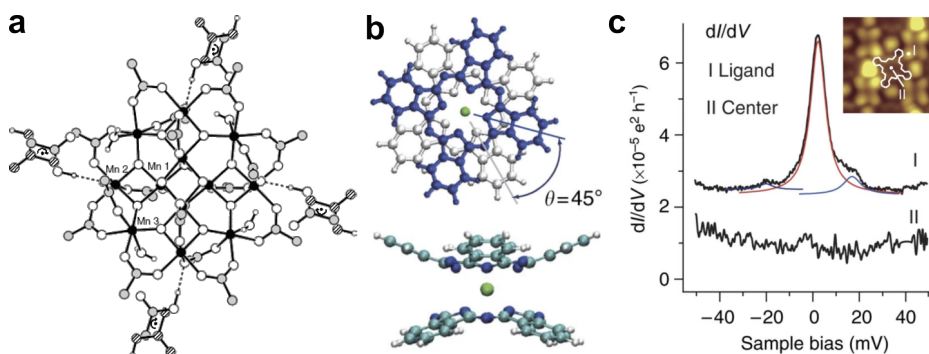


Figure 2.4: *Transition metal clusters and double-decker molecules are considered as SMMs. a, The chemical structure of $Mn_{12}O_{12}(CH_3COO)_{16}$. The black circles are Mn, O are white, C are grey, and H are small white circles. Reprinted with the permission from [68]. b, A top view (top) and the side view (bottom) of a bis(phthalocyaninato)terbium(III) (TbPc$_2$). c, The self-assembly of TbPc$_2$ on Au(111) shows Kondo resonance on the dI/dV spectrum. Figures b-c reprinted with the permission from [82].*

**Magnetism from transition metal elements.**   $3d$ transition metal elements, such as Cr, Mn, Fe, Co and Ni, have magnetic moment due to the electron orbital moment. Directly depositing transition metal atoms on a surface is a straightly forward approach to study the interaction between magnetic moments and various substrate electron DOS. However, the strong orbital hybridization with the substrate often alters intrinsic magnetic properties of single atoms, and a thin insulating decoupling layer is usually needed [64].

Capsuling transition metal ions with ligands can effectively protect the atomic spin. Some types of molecules with multiple metal ion sites could elongate the spin relaxation time by generating large magnetocrystalline anisotropy energy. These molecules resemble single ferromagnets, and are known as *single-molecule magnets (SMMs)* [64,68,83]. Examples of SMMs include $Mn_{12}$-acetate complexes ($Mn_{12}O_{12}(RCOO)_{16}$) (Fig. 2.4a) and double-decker molecules (Fig. 2.4b-c) [82,83].

**π-magnetism in carbon nanostructures.**   Polycyclic aromatic hydrocarbons (PAHs) are composed of fused benzene rings with only carbon (C) and hydrogen (H) atoms. The structure is stabilized by the π-bond resonance, which is induced by the overlapping of parallel aligned $p_z$-orbitals of carbon. The honeycomb lattice of PAHs is
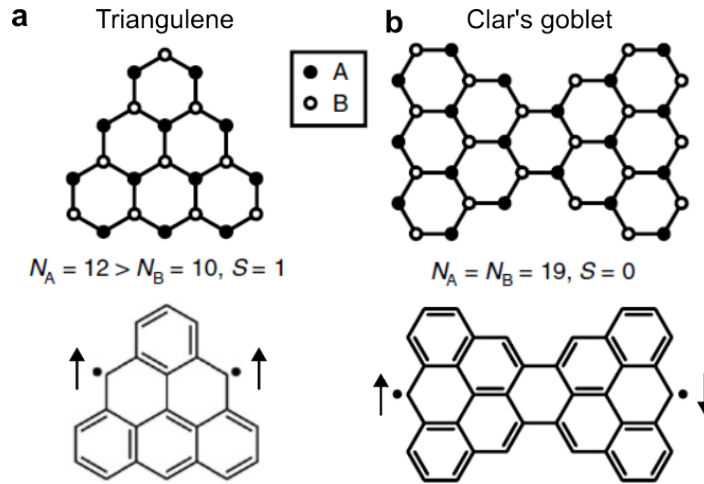
**Figure 2.5:** ***Localized spins in PAHs. a,*** *Two unpaired spins arise on a triangulene due to sublattice imbalance.* ***b,*** *Two unpaired spins couple antiferromagnetically on a Clar's goblet due to topological frustration. In the upper penal, solid and hallow circles represent carbon atoms in A and B sublattices respectively. Adapted with the permission from [86, 87].*

bipartite, the number of carbon atoms in each sublattice is denoted as $N_A$ and $N_B$ respectively. If $N_A$ and $N_B$ are equivalent, these PAHs are close-shell Kekulé structures with no net spin. On the other hand, a net spin arises on an open-shell Kekulé structure when sublattice imbalance ($N_A \neq N_B$) occurs. The net spin of the open-shell PAH can be then estimated by Lieb's theorem [84, 85]: $S = |N_A - N_B|/2$. Triangular zigzag (ZZ) PAHs, or known as *triangulenes*, are examples that show spins through sublattice imbalance (Fig. 2.5a). In addition, net spins on PAHs can also arise due to topological frustration without sublattice imbalance. In those structures, it is impossible to assign all $p_z$-orbitals into pairs and form $\pi$-bonds, thus some $\pi$-electrons are left unpaired [85]. It is found that Clar's goblet is one of these particular topologies which hosts two antiferromagnetically coupled spins at two edges (Fig. 2.5b) [86].

Similar to PAHs, ZZ segments at GNR edges are able to host unpaired spins due to sublattice imbalance [88]. As introduced in section 2.1.1, carbon-based GNRs can be synthesized into designed structures *via* Ullmann coupling, including the fabrication of a long-range pattern of ZZ segments at edges. With the bottom-up approach, the spin-spin spacing is able to be precisely controlled while ensuring the spin-1/2 quasi-1D chain with minimal spin-orbit coupling (SOC). Moreover, in some specific orders of ZZ segments, it is possible to generate non-trivial topological phase at the junction of GNR patterns [89–91]. In addition to GNRs, connecting triangulenes through covalent bonds is an approach to realize spin chains based on $\pi$-magnetism. In the study by Mishra *et al.* [92], triangulene chains are able to exhibit spin-substrate (see Section 2.2.1 for Kondo effect) and spin-spin coupling (see Section 2.2.2 for spin-flip excitation) on the Au(111) substrate.
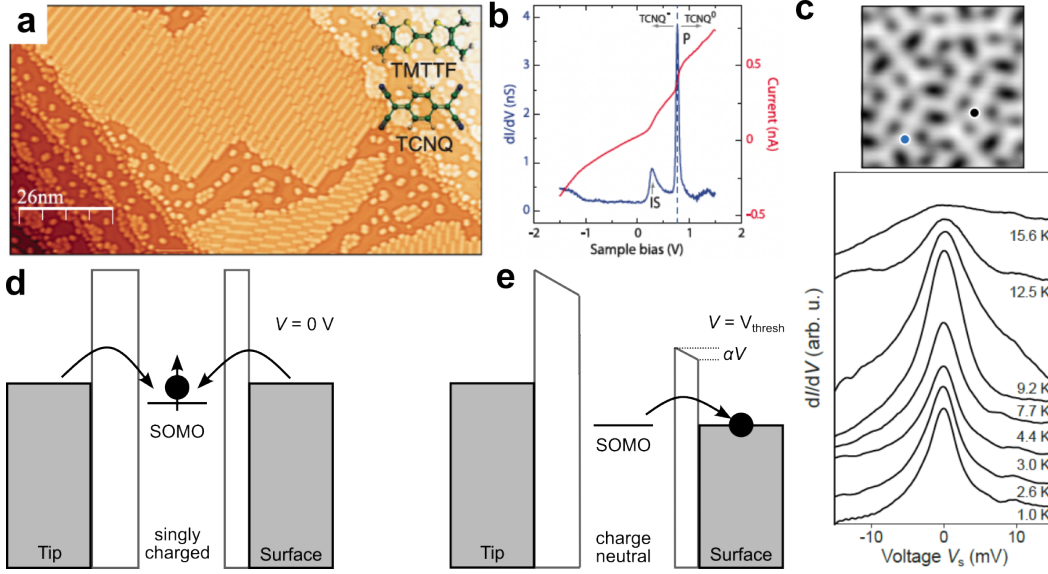
**Figure 2.6:** *Exemplary systems and dI/dV spectra of molecular acceptors on surfaces.* ***a,*** *A STM image of the assembly of the electron-acceptor tetracyanoquinodimethane (TCNQ) and the electron-donor tetramethyltetrathiafulvalene (TMTTF) on Au(111).* ***b,*** *An exemplary dI/dV measured on a charged TCNQ, showing the molecular-induced interface state "IS" and the signature of the discharging event "P". Figures **a-b** are reprinted with the permission from [28].* ***c,*** *The 4,5,9,10-tetrabromo-1,3,6,8-tetraazapyrene (TBTAP) assembly on Ag(111) exhibits Kondo resonance peak around $E_F$, confirming the spin-1/2 state of a charged TBTAP molecule. Reprinted with the permission from [30].* ***d-e,*** *The DJTB model illustrating the charge transfer mechanism at the molecule-substrate junction.*

**Electronic spin in a molecular acceptor.** A self-assembled and metal-free magnetic framework can be realized by depositing designed molecular electron-acceptors on surfaces. Such molecular acceptors enable charge localization and an integer number of charge transfer, making it an ideal candidate of a single molecular transistor [28]. This type of molecules consists of an electron-accepting backbone and subtiuents that can reduce the coupling with the metallic substrate [29,30].

In recent studies, such molecules can be treated as quantum dots (QDs), and their charge states are able to be controlled by the field imposed by the STM tip [28,30,93]. In the STS study, the discharging event of molecular acceptors is shown as a sharp conductance peak as in Fig. 2.6b. The peak-like Kondo lineshape (see Section 2.2.1) observed a molecular acceptor confirms the spin-1/2 state from the additional electron being trapped in the molecule (Fig. 2.6c).

The mechanism of charge transfer, or *gating*, can be explained by the double-junction tunneling barrier (DJTB) (Fig. 2.6d-e). Due to the double potential barriers generated at the tip-molecule and molecule-substrate junctions, the bias $V$ applied by the tip is reduced to the potential shift of $\alpha V$ with respect to the chemical potential of the substrate at the molecule, where $\alpha$ is the lever arm, representing the efficiency
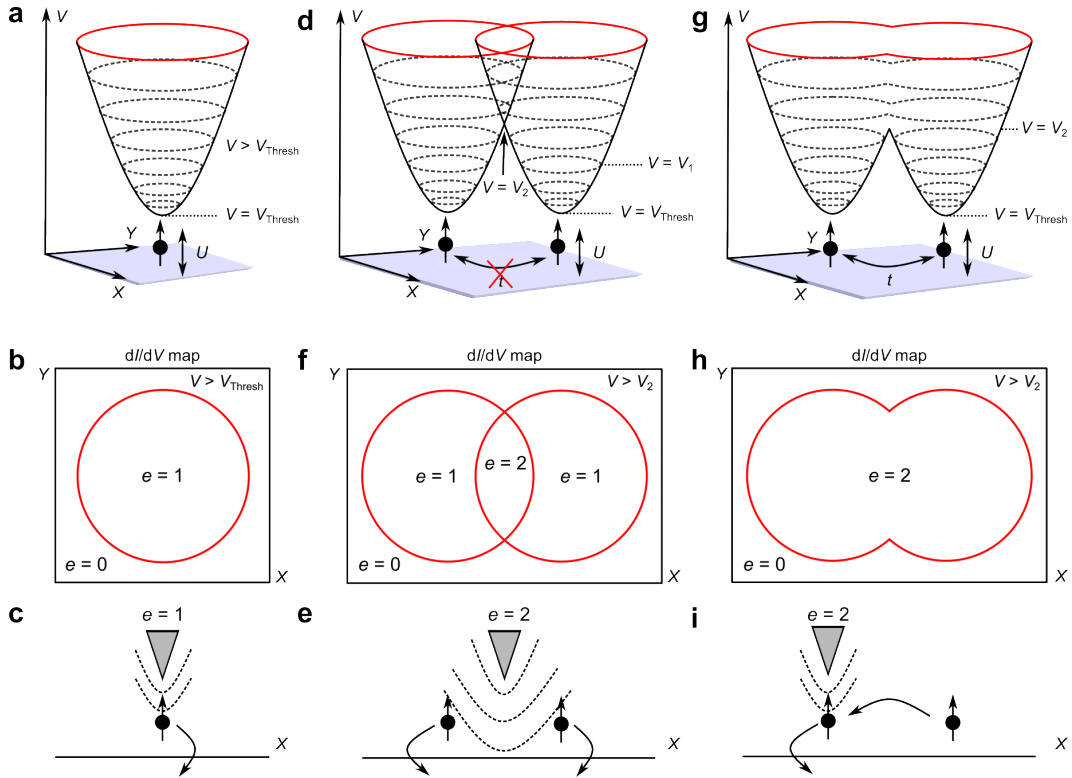
**Figure 2.7:** *A scheme illustrating the formation of Coulomb rings by tip-induced field.* **a,** *A molecular QD system with on-site Coulomb interaction $U$ can be discharged by the electric field imposed by the tip when $V \geq V_{thresh}$.* **b,** *With a constant tip-sample separation, the discharge event appears as a dot or ring in the $dI/dV$ map depending on the applied bias. Inside the ring, the tip efficiently couples with the QD and triggers the single discharge ($e = 1$) as depicted in* **c.** **d,** *Two non-interacting QDs with on-site Coulomb interaction $U$ can also be discharged by the tip-field $V \geq V_{thresh}$. At $V = V_2$, paraboloids centered to each QD start crossing, leading to the intersection of the Coulomb rings in $dI/dV$ map as shown in* **e.** *The region $e = 2$ marks the $(X, Y)$ positions of the tip that allow the discharge of both QDs as in* **f.** **g,** *Two interacting QDs with on-site Coulomb interaction $U$ and hopping exchange $t$ can be discharged by tip-gating when $V \geq V_{thresh}$. In contrast to the non-interacting case, applying $V = V_2$ leads to the fusion of the Coulomb rings in the $dI/dV$ map (**h**). In the region $e = 2$, discharge of both QDs occurs if the tip is not located directly above one QD. The ring fusion is the fingerprint of electron hoping between neighboring molecular sites (**i**).*

of discharging the molecule. At first approximation, $\alpha$ is also linearly dependent on the applied bias and the relative $(X, Y, Z)$ position of the tip to the molecule.

In the case of a single molecule, a single discharging event appears as $V$ reaches $V_{thresh}$ at the constant tip-sample distance $z$ (bottom of the parabola in Fig. 2.7a), showing a dot in the constant-height $dI/dV$ map. When $V > V_{thresh}$, the dot expands to a ring as marked by the red circle at the top of the parabola in Fig. 2.7a, and the ring diameter linearly increases with $V$ since the stronger electric field is able

to discharge more efficiently in the lateral dimension. Discharging rings occurred at different applied bias form concentric rings in the paraboloid in Fig. 2.7a right above the charge on the surface. The consequent ring defines the boundary of single-charge ($e$= 1 region) and zero-charge ($e$= 0) removal (Fig. 2.7b).

In the case of two non-interacting QDs, the same on-site Coulomb interaction $U$ leads to the identical $V_{thresh}$, which further results in similar series of discharging rings at QD sites (Fig. 2.7d). With the presumption of zero hopping exchange ($t$), identical ring sizes occur when $V = V_1$ on the d$I$/d$V$ map ($e$= 1 in Fig. 2.7f) with the tip at the vicinity. When $V = V_2$, two paraboloids start to cross, a double discharging event is possible at $(X, Y)$ positions equidistant from two QDs ($e$= 2 in Fig. 2.7f). In d$I$/d$V$ maps, double discharge is shown as crossing of the neighboring rings, inside which two charges can be removed by the tip field.

Lastly, assuming a non-zero $t$ between two QDs, each QD also has identical series of discharging rings (Fig. 2.7g). In contrary to the non-interacting case, when $V \geq V_2$, neighboring rings fuse in d$I$/d$V$ maps without intersection. The fused rings indicates the double discharge of both QDs for all $(X, Y)$ positions inside the fused area ($e$= 2 in Fig. 2.7h). Therefore, with interacting QDs, placing the tip near the target QD is not a strict necessity to trigger discharging events (Fig. 2.7i).

## 2.2 Spins on a Normal Metal Substrate

The coupling between a magnetic impurity and electrons near the Fermi sea involves many-body process which usually occurs at energies close to the Fermi level. As a powerful tool to investigate or manipulate such interactions in the atomic or molecular level, tunneling spectroscopy reveals two common interactions: Kondo resonances and spin-flip excitations.

### 2.2.1 Kondo effect

Typically, the resistance of a normal metal decreases with the lowering temperature due to the reduction in phonon scattering. However, it was found that with a small fraction of magnetic impurities, the resistance of a normal metal starts to increase below a certain temperature. In 1964, Jun Kondo explained this observation by introducing perturbation Hamiltonian to the dilute magnetic alloy system, which is later known as *Kondo effect* [95]. The characteristic temperature is denoted as *Kondo temperature*.

In the microscopic point of view, Kondo effect is the result of the local screening of the magnetic moment by antiferromagnetically coupled itinerant electrons from the substrate, and the incident electrons are scattered *via* elastic spin-flipping (Fig. 2.8a) [96, 97]. As illustrated in Figs. 2.8b-d, single-impurity Anderson model can nicely explain Kondo effect in the dilute alloy system. The Anderson model assumes only one energy state $\varepsilon_0$ below the Fermi level occupied by an electron (Fig. 2.8b). Due
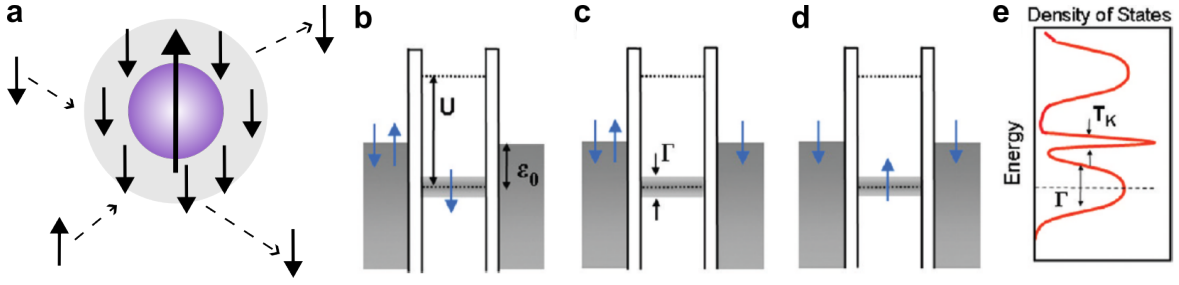
**Figure 2.8:** ***The scheme of Kondo screening and Anderson impurity model.*** ***a,*** *A scheme showing the local screening of the magnetic impurity by itinerant electrons of the substrate. Incident electrons are scattered with a spin-flip process.* ***b,*** *The Anderson model involves only one state with energy $\varepsilon_0$ below the Fermi level. Due to Coulomb repulsion, an empty state with the energy difference $U$ is created above $\varepsilon_0$.* ***c,*** *In the "virtual" state, the electron tunnels out from the spin state to the Fermi sea without adding energy to the system. The linewidth of the state is broadened due to the tunneling effect.* ***d,*** *An electron tunnels from the Fermi sea to compensate the temporarily empty spin state.* ***e,*** *An exemplary spectrum showing the energy distribution of DOS based on the Anderson model. Figures* ***b-e*** *are reprinted with the permission from [94].*

to Heisenberg uncertainty principle, the electron is able to tunnel out from its spin state to the DOS continuum without consuming energy (Fig. 2.8c) [98]. In this short timescale ($\approx h/\varepsilon_0$, where $h$ is the Planck constant), another electron tunnels to the spin state with an opposite spin from the original one, resulting in an equivalent spin-flip event (Fig. 2.8d) [98]. A collective tunneling leads to the screening effect, with the energy at $E_F$.

Figure 2.8e is an example of a Kondo resonance $\mathrm{d}I/\mathrm{d}V$ spectrum predicted by the Anderson model, which corresponds to a spin-1/2 system. The width of the spin state energy level $\Gamma$ is broadened due to the tunneling effect, which is related to the Kondo temperature ($T_K$) and further modifies the linewidth of the Kondo resonance [99]:

$$T_K = \frac{1}{2}\sqrt{\Gamma U}e^{\pi\varepsilon_0(\varepsilon_0 + U)/\Gamma U}. \tag{2.1}$$

With different spin states and substrates, there could be distinct spectra from Fig. 2.8e, exhibiting an asymmetric Kondo lineshape or a dip. Nevertheless, the lineshape can be fitted with Fano or Frota functions, the latter is modified by the numerical renormalization group calculation and found to describe tunneling spectra better [100, 101]:

$$Fano(V) \propto \frac{(q+\epsilon)^2}{1+\epsilon^2}, \qquad Frota(V) \propto Im\left[e^{i\phi}\sqrt{\frac{i\Gamma_{Frota}}{eV - E_K + i\Gamma_{Forta}}}\right], \tag{2.2}$$

where $V$ is the sample bias, $q$ and $\phi$ are the asymmetric factors that determines the Kondo lineshape for Fano and Frota functions respectively, $\epsilon$ is the normalized energy written as $\epsilon = (eV - E_K)/\Gamma_{Fano}$, $E_K$ is the energy of the Kondo resonance, and the half-width at half-maximum (HWHM, $\Gamma_K$) of the resonance is equal to $\Gamma_{Fano}$ or $2.54\Gamma_{Frota}$. The asymmetric factor $q$ and $\phi$ could be the result of coupling between the adsorbate and the metal wavefunctions [102].

From Equ. 2.2, $T_K$ can be extracted as [103]:

$$\Gamma_K = \frac{1}{2}\sqrt{(\alpha k_B T)^2 + (2k_B T_K)^2}, \tag{2.3}$$

where $\alpha$ is the slope of the linear growth of $\Gamma_K$, $k_B$ the Boltzmann constant, and $T$ the temperature. As indicated in Equ. 2.3, the Kondo linewidth is broadened as the temperature increases.

## 2.2.2 Magnetocrystalline anisotropy

Upon adsorption of magnetic impurities on a crystalline surface, the combined effect with SOC of the magnetic impurities gives rise to the varying magnetization intensity along different crystalline axes, also known as *magnetocrystalline anisotropy (MA)* [68,104]. The spin state $S$ of the impurity could split into multiplet without an external magnetic field, and solely due to the effect of MA, leading to *zero field splitting (ZFS)*. Factors that modify MA include the adsorption symmetry with respect to the substrate and ligands attached to the ion. The overall influence of the surrounding to the metallic ion can be expressed by the crystal field Hamiltonian [68]. In the case of a single ion, the Hamiltonian has the form:

$$\mathcal{H}_{\mathcal{CF}} = D_{xx}\hat{S}_x^2 + D_{yy}\hat{S}_y^2 + D_{zz}\hat{S}_y^2, \tag{2.4}$$

where $D_{xx}$, $D_{yy}$, and $D_{zz}$ are the anisotropy strength in $x$-, $y$-, $z$-axis, and $\hat{S}_x$, $\hat{S}_y$, $\hat{S}_z$ are spin operators along corresponding axes. By subtracting a constant $1/2(D_{xx} + D_{yy})S(S+1)$ from Equ. 2.4, the Hamiltonian can be written as

$$\mathcal{H}_{\mathcal{CF}} = D\hat{S}_z^2 + E(\hat{S}_x^2 - \hat{S}_y^2), \tag{2.5}$$

with $D = D_{zz} - 1/2D_{xx} - 1/2D_{yy}$ and $E = 1/2(D_{xx} - D_{yy})$. The new parameters $D$ and $E$ are the strength of axial and transverse anisotropy respectively. In the case of axial symmetry, meaning that the magnetization strength is isotropic on the $xy$ plane ($D_{xx} = D_{yy}$), Equ. 2.5 is then simplified into

$$\mathcal{H}_{\mathcal{CF}} = D\hat{S}_z^2. \tag{2.6}$$

By solving Equ. 2.6, eigenstates are the spin state in $z$-projection, which are $|m_z\rangle = |-S\rangle, |-S+1\rangle ... 0 ... |S-1\rangle, |S\rangle$ with the definition $\hat{S}_z|m_z\rangle = m_z|m_z\rangle$. It can be thus interpreted as the splitting of spin state $S$ into $(2S+1)$ multiplet with the effect of axial anisotropy $D$. Furthermore, due to the quadratic nature of Equ. 2.6, state energy is the same with identical $|m_z|$. Next, by introducing the $E$ term, $|m_z\rangle$ starts to hybridize with each other under the criteria $\Delta m_z = \pm 2$. Note that $D$ can be either positive or negative. According to the spin excitation scheme, a low-spin ground state favors positive $D$, while a high-spin ground state has negative $D$. In convention, $D$ and $E$ solved from Equ. 2.5 should fulfill the criteria of maximizing $|D|$ and letting $E > 0$ [105]. Nevertheless, in some cases of large half-integer spins, positive $D$ values split $S$ with degenerate $m_z = \pm 1/2$ as ground states, which promotes Kondo resonance with the coexistence of spin-flip excitations at larger energies [96].

### 2.2.3  Coupled spins

For the presence of multiple spins with small spacings, the wavefunction overlap between adjacent atoms/molecules enables the exchange of electrons, leading to the coupling of spins [64]. Heisenberg coupling indicates the so-called ferromagnetic or antiferromagnetic coupling, meaning that neighboring spins are either parallel or antiparallel aligned. With the lack of inversion symmetry at surfaces or interfaces, Dzyaloshinskii-Moriya interaction (DMI) arises when the spin-orbit coupling (SOC) breaks the inversion symmetry of hopping electrons in Heisenberg exchange [106–109]. The noncollinear nature of the spin order induced from DMI could results in exotic spin textures [108]. By taking Heisenberg coupling and DMI into account, the Hamiltonian in Equ. 2.5 is modified as [97]:

$$\mathcal{H} = \sum_i (D(\hat{S}_z^i)^2 + E((\hat{S}_x^i)^2 - (\hat{S}_y^i)^2)) + \sum_{i,j} \vec{\mathcal{J}}_{ij}\hat{\mathbf{S}}^i \cdot \hat{\mathbf{S}}^j + \sum_{i,j} \vec{\mathcal{D}}_{ij}\hat{\mathbf{S}}^i \times \hat{\mathbf{S}}^j, \qquad (2.7)$$

where $\vec{\mathcal{J}}_{ij}$ and $\vec{\mathcal{D}}_{ij}$ are vectors of Heisenberg coupling and DMI terms respectively, and $\hat{\mathbf{S}}^i$ the total spin operator which is composed of $\hat{S}_x^i$, $\hat{S}_y^i$, and $\hat{S}_z^i$. Heisenberg interaction can be separated into the isotropic and anisotropic terms. The isotropic component can be simply written as a scalar $J_{ij}$, and a positive value represents ferromagnetic coupling while a negative one stands for antiferromagnetic coupling [68].

In addition to direct coupling *via* the wavefunction overlap, through the mediation of substrate itinerant electrons, a long-range coupling up to few nanometers can be achieved (Fig. 2.9), which is known as *Ruderman-Kittel-Kasuya-Yosida (RKKY) interaction* [110–112]. Due to the close vicinity of a magnetic moment, itinerant electrons in the substrate possess a preferential spin orientation which oscillates with the distance from the magnetic source. Another magnetic moment then couples with the oscillating spin-density in either the ferromagnetic or antiferromagnetic manner [113].
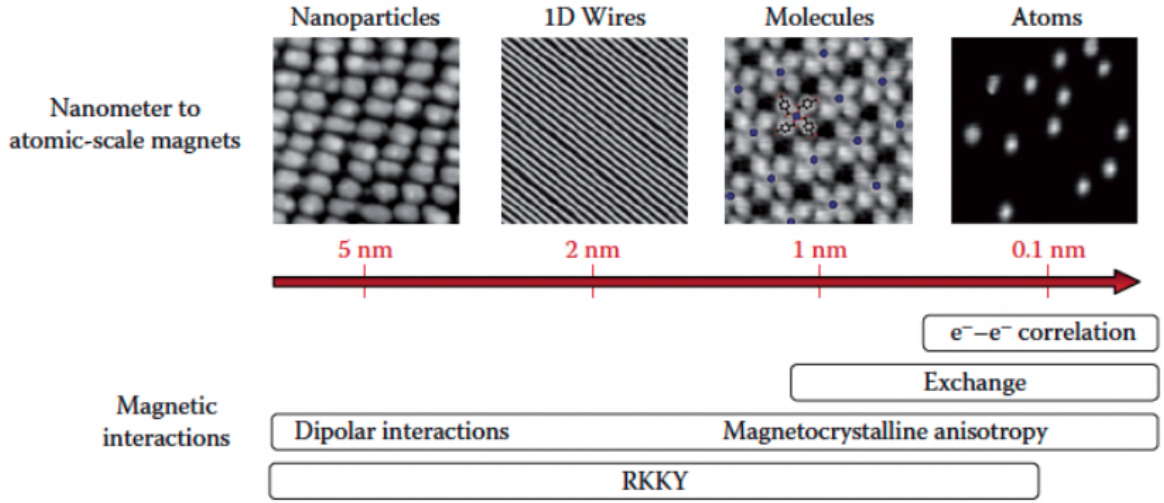
**Figure 2.9:** *Magnetic coupling in different length scales.* *At different distances, different spin coupling mechanisms come to effect. Reprinted with the permission from [64].*

In this dissertation, we examine magnetic properties in atomic and molecular systems on surfaces. From Fig. 2.9, electron-electron correlation, exchange coupling due to electron hopping, magnetocrystalline anisotropy, and RKKY interaction are the main coupling mechanisms in our study.

## 2.3 Spins on a Superconductor

In contrary to normal metals, spins of electrons on a superconductor are limited by Pauli exclusion principle due to the formation of Cooper pairs. Upon adsorption of a magnetic impurity, the impurity spin can break Cooper pairs and result in quasiparticle excitations. In this section, superconductivity will be first introduced, followed by the discussion of the interaction between magnetic moments and superconducting states.

### 2.3.1 Superconductivity

The resistance of metals tends to drop as the temperature decreases due to the reduction of lattice vibration. For some materials, it is found that the resistance drops to zero while lowering the temperature to a critical value ($T_c$). Such property is later known as *superconductivity*, and the materials are *superconductors*. The first observation of superconductivity was made by Heike Kamerlingh Onnes in 1911, who is also the pioneer of liquefying helium, by cooling solid mercury to 4.2 K [115]. In addition, superconductors are also able to repel an external magnetic field up to a critical value ($H_c$), known as *Meissner effect* [116]. Meissner effect can be used to distinguish type-I and type-II superconductors. Superconductivity of type-I superconductors vanishes

29
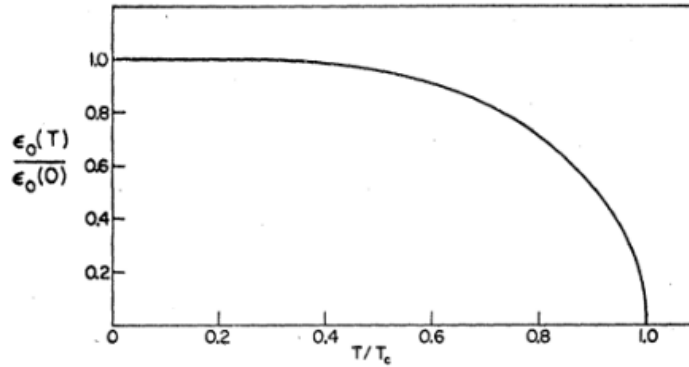
**Figure 2.10:** *The relation between the energy gap of a superconductor to temperature.* *The ratio of the energy gap to that at 0 K drops as the temperature increases, and finally the gap closes when reaching $T_c$. Reprinted with the permission from [114].*

when the magnetic field raises above $H_c$. On the other hand, type-II superconductors have a lower ($H_{c1}$) and a higher ($H_{c2}$) critical field. When the applied field falls between these two limits, magnetic flux quanta are able to penetrate through, locally destroy the superconductivity, and exhibit Abrikosov vortices [117].

From the microscopic point of view, below $T_c$, electrons in superconductors condensate into pairs *via* the indirect phonon exchange, which results in attractive interaction that dominates over Coulomb repulsion [118]. Due to the pairing energy of electrons ($\Delta$), there is an energy gap ($2\Delta$) about a few meV symmetric to $E_F$, being known as the *superconducting gap*. The symmetry to $E_F$ also implies the particle-hole symmetry of the superconducting state. The explanation of the phenomenon was further completed by Bardeen, Cooper, and Schrieffer [114]. Bardeen-Cooper-Schrieffer (BCS) theory was therefore developed to describe conventional superconductivity, which has symmetric pairing ($s$-wave pairing) of electrons in space. BCS theory also describes the temperature dependency of the superconducting gap (Fig. 2.10) as one of the characteristics of a conventional superconductor. The spatial dimension of a Cooper pair is denoted as the coherence length ($\xi$), in which the attractive force remains between two electrons in a Cooper pair.

From BCS theory, DOS of a conventional superconductor around $E_F$ was derived in [114] as:

$$\rho_{bcs}(E) = \frac{E}{\sqrt{E^2 - \Delta^2}}. \tag{2.8}$$

However, as temperature increases, the superconducting gap can be broadened and becomes more shallow as a "soft" gap. As fermions, the excitation probability of electrons follows Fermi-Dirac function at finite temperature as shown in the following:

$$f(E, T) = \frac{1}{1 + e^{E/kT}}, \tag{2.9}$$

$$f'(E, T) = \frac{1/kT}{2 + e^{E/kT} + e^{-E/kT}}. \tag{2.10}$$

The superconducting gap width demonstrated in Chapter 3 to Chapter 6 is estimated by fitting the $dI/dV$ spectra with thermal-broadened BCS function, which is obtained by convoluting BCS function with Fermi-Dirac function:

$$\rho_{bcs'}(E, T) \propto \int \rho_{bcs}(E - \varepsilon) f'(\varepsilon, T) d\varepsilon \tag{2.11}$$

Another aspect of superconductivity was developed by introducing the concept of "quasiparticles". At finite temperatures, unpaired electrons from the broken Cooper pairs are considered as quasiparticles with spin-1/2 [119]. Dynes *et al.* modified the superconductivity DOS derived from BCS theory (Equ. 2.8) by considering the recombination of two quasiparticles close to the energy gap edge [120]. Thus, the quasiparticle lifetime ($\Gamma$) is included to estimate DOS:

$$\rho_{dynes}(E) = \rho_0 Re \left[ \frac{E - i\Gamma}{\sqrt{(E - i\Gamma)^2) - \Delta^2}} \right], \tag{2.12}$$

Bogoliubov quasiparticles were further proposed to describe excitations in superconductors [121]. Excitations can be written as a superposition of a particle-like component and a hole-like component, which can be solved from the Bogoliubov-de Gennes Hamiltonian [122]. Quasiparticle excitations play an important role when introducing magnetic adsorbates which could break Cooper pairs and generate localized bound states. The magnetism-superconductivity interaction will be elaborated in Section 2.3.3.

## 2.3.2 Proximity-induced superconductivity

Proximity effect can be found at the interface of a normal metal and a superconductor (NS interface). In conventional superconductors, electrons condensate into Cooper pairs. Since the pairing pattern of electrons cannot change abruptly across the interface, Cooper pairing leaks to the immediate vicinity of the normal metal. The microscopic scattering event at the NS interface can be described by Andreev reflection (Fig. 2.11). As illustrated in the scheme, an electron injected from the normal metal to the interface can be transmitted to a Cooper pair when there is another injected electron, which can be viewed as the retro-reflection of a hole in the opposite direction with the identical momentum [123]. The leakage of Cooper pairs to the normal metal has the opposite mechanism, as plotted in the lower part of Fig. 2.11.
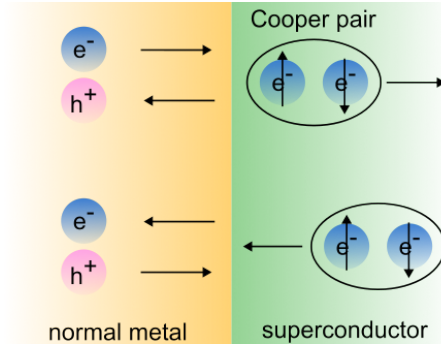
**Figure 2.11: *Andreev reflection at the NS interface.*** *At the interface, an incident electron from the normal metal reflects back as a hole in the opposite direction. The charge difference is absorbed as a Cooper pair in the superconductor.*

As proposed by McMillan [124], proximity effect at the NS interface can be treated as a tunneling process of Andreev reflection with a potential barrier at the interface. Thus, the quality of the interface, such as impurities or lattice mismatch, could largely influence the proximity effect.

### 2.3.3 Yu-Shiba-Rusinov states

**Tunneling measurement of Yu-Shiba-Rusinov states.** A magnetic impurity adsorbed on a superconductor can impose an exchange interaction into the scattering of Cooper pairs, resulting in a local pair-breaking potential. The exchange coupling induces Bogoliubov quasiparticle excitations, generating low-energy bound states inside the superconducting gap, which are known as *Yu-Shiba-Rusinov states (YSR states)* [43, 125–128].

In d$I$/d$V$ spectra, YSR states are shown as pairs of asymmetric peaks inside the superconducting gap. Depending on the magnetic moment and the crystal field around the magnetic impurity, the orbital degeneracy is lifted, and multiple pairs of YSR states can arise due to different scattering channels of the angular momentum [43, 129]. From the method of Yu, Shiba, and Rusinov, the bound state energy can be expressed as [43, 130, 131]:

$$\varepsilon = \Delta \frac{1 - \alpha^2}{1 + \alpha^2}, \quad \text{while} \quad \alpha = J_K S \pi \rho_s / 2. \quad (2.13)$$

Here, $J_K$ is the exchange coupling strength between the magnetic impurity and the Cooper pair (also the Kondo exchange coupling), $\rho_s$ is the substrate DOS at $E_F$ in the normal state, and $S$ is the spin state of the impurity. As indicated in Equ. 2.13, the bound state energy is determined by $J_K$. When the coupling is weak, the small $J_K$ merges YSR states to the superconducting coherence peaks.
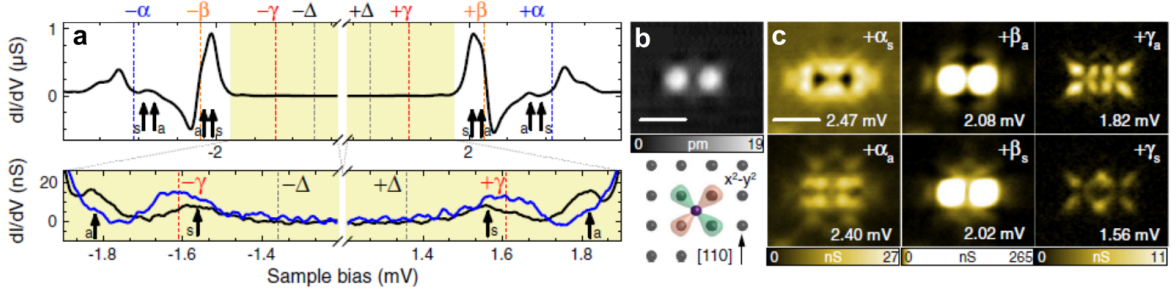
**Figure 2.12:** *dI/dV spectra and conductance maps of a Mn dimer on the superconducting Pb(001). **a,** Three pairs of YSR states ($\pm\alpha$,$\pm\beta$, $\pm\gamma$) are observed on a Mn dimer, and each of them splits into symmetric and antisymmetric hybridization of YSR wavefunctions. **b,** The STM image of the target Mn dimer. **c,** Series of dI/dV maps of the Mn dimer at positive YSR energies. A nodal line perpendicular to the dimer axis is observed on the antisymmetric hybridized YSR wavefunctions ($\alpha_a$, $\beta_a$, $\gamma_a$). Reprinted with the permission from [132].*

**Hybridization of Yu-Shiba-Rusinov states.** Although YSR states are bound to magnetic impurity sites, YSR wavefunctions have a slow spatial decay, enabling wavefunction hybridization. The particle-like ($u(r)$) and hole-like ($v(r)$) wavefunctions can be found by solving the Bogoliubov-de Gennes equation [122, 127]:

$$u(r), v(r) \propto \frac{sin(k_F r + \delta^\pm)}{k_F r} exp\left[-|sin(\delta^+ - \delta^-)|\frac{r}{\xi}\right], \qquad (2.14)$$

where $k_F$ is the Fermi wavevector, $\delta^\pm$ are the scattering phase shift, and $\xi$ is the coherence length of the superconductor. From Equ. 2.14, the wavefunction decays with the factor $1/(k_F r)$ in short distances, and it has an exponential decay in large distance which further depends on $\xi$ [43]. An example of YSR hybridization has been studied in the Mn dimer system on the superconducting Pb(001) [132]. The symmetric and antisymmetric superposition of YSR wavefunctions splits each resonance peak into two on the dI/dV spectrum (Fig. 2.12a). On conductance maps at corresponding YSR energies, the d-orbital shapes of a single Mn still remain (Fig. 2.12c) [132].

By fabricating magnetic atoms into a spin chain (Shiba chain) or a spin island (Shiba lattice), the formation of YSR bands is expected, and this is considered as a promising route towards the realization of topological superconductivity (see Section 2.4) [18, 133–135].

**Quantum phase transition.** As discussed in Section 2.2.1, the antiferromagnetic coupling of the impurity spin with itinerant electrons can lead to a Kondo singlet state. This also happens on a superconductor under the condition $k_B T_K \gg \Delta$, when the screening energy is much larger than the pairing energy [137]. In the weakly screening regime $k_B T_K \ll \Delta$, YSR states are observed and Kondo resonances are suppressed due to the DOS depletion around $E_F$ [43, 65]. Under the criteria $k_B T_K \sim \Delta$, Kondo
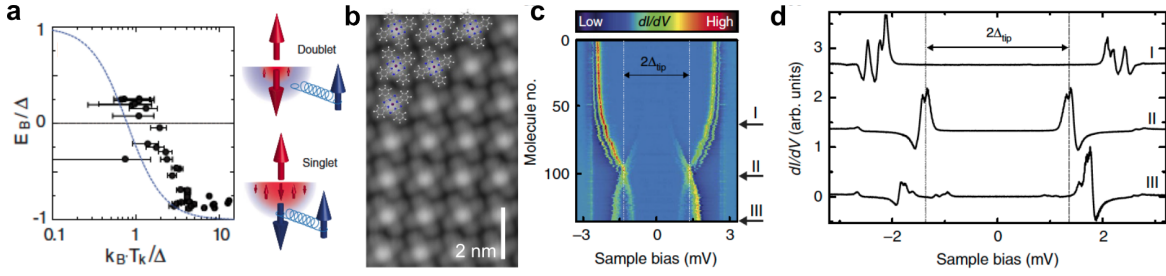
**Figure 2.13:** ***STS study of quantum phase transition arise from the modulation of adsorption sites.*** *a, A plot showing the relation between the bound state energy ($E_B$) and the Kondo energy ($k_B T_K$). The strong coupling with the substrate (large $k_B T_K$) gives rise to the Kondo singlet ground state. A small $k_B T_K$ leads to an weak Kondo screening, and a broken Cooper pair is bound to the magnetic site, which is the free-spin ground state. Reprinted with the permission from [65]. **b,** The STM image of a MnPc self-assembly on Pb(111). **c,** The dI/dV contour along the Moiré of a MnPc assembly, showing the excitation peaks shift from hole-dominant to particle-dominant excitations (I→III)). **d,** dI/dV spectra extracted from **c** at the corresponding markers **b**-**d** reprinted with the permission from [136].*

screening and superconducting pairing coexist, with the ratio of their strengths leads to *quantum phase transition* [43, 65, 138].

Quantum phase transition describes the crossing of YSR states through the Fermi level, and the transition between the Kondo-screened singlet to the free-spin doublet ground state occurs (Fig. 2.13a) [65]. The STS observation of quantum phase transition has been studied on a MnPc assembly on the sueprconducting Pb(111) [65, 136]. As shown in Fig. 2.13c, d, along the Moiré of the MnPc assembly, YSR peaks shift their spectral weight from the negative bias (hole-like) regime to the positive bias (particle-like) regime (I→III), with the merge at $E_F$ (spectrum II, at $\pm\Delta_{tip}$). This also marks the switch from Kondo-screened to the free-spin ground state [65, 136].

In addition to adsorption sites, the exchange coupling strength between the magnetic molecule and the superconducting substrate also changes by imposing the force from the tip to the target molecule [130, 139]. Following the Lennard-Jones potential diagram, when the tip approaches the surface, an attractive force is induced between the tip-sample junction, which lifts the molecule from the surface (Fig. 2.14a). The decreasing exchange coupling between the impurity spin and Cooper pairs drives the molecule through a quantum phase transition from the Kondo-screened ($S = 0$) to the free-spin ($S = 1/2$) many-body ground state [139]. In a dI/dV spectrum, the shift of the YSR energy (Fig. 2.14b, c) has a similar trend as the lattice-modulated quantum phase transition (Fig. 2.13c).
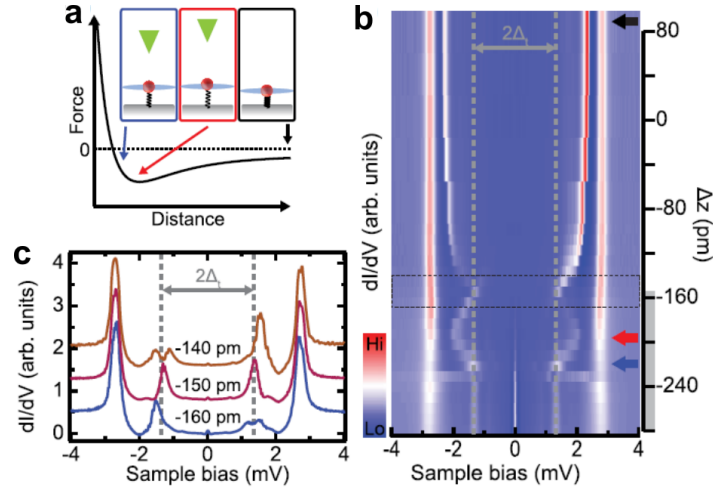
**Figure 2.14:** *STS study of quantum phase transition driven by the tip-induced force. **a,** The Lennard-Jones potential diagram indicates an attractive force when the tip approaches the surface (red box), which pulls the molecule upwards and reduces the coupling with the substrate. If the tip goes further closer, an induced repulsive force pushes the molecule towards the surface (blue box). **b,** The dI/dV contour of a Fe-porphin (FeP) molecule adsorbed on the Pb(111) superconductor. The weight of YSR states changes along with the tip-sample distance. **c,** Before the quantum phase transition, the molecule is in the Kondo-screened ground state, having a higher spectral weight in the positive bias YSR state (brown spectrum). The claret spectrum marks the quantum phase transition, at which YSR states merge to $E_F$ ($\pm\Delta_t$ in the spectrum). The molecule shifts to the free-spin ground state after the quantum phase transition, which has a higher intensity at the negative YSR energy (blue spectrum). Reprinted with the permission from [139].*

## 2.4  Topological Superconductivity

Topological superconductors are currently of particular interest in condensed matter physics due to their tolerance to the external disturbance and noise, considered as ideal building blocks for topological quantum computation [7, 13]. Topological superconductivity (TSC) is elusive in nature, but it can also be engineered in hybrid heterostructures by coupling an electron gas with spin-momentum locking to a conventional superconductor [140–144].

The emergence of TSC is closely related to Majorana fermions, which is defined by a particle being its own antiparticle [8]. At zero energy, Bogoliubov quasiparticles, which are the superpositions of particle and hole excitations, are chargeless as the particle and hole components are equivalent, yet net spins remain [10]. When both of the criteria are reached–being chargeless and spinless–Majorana fermions arise at zero energy, with the spatial distribution at the topological margin. To achieve zero net spin, a *p*-wave superconducting pairing is required that the hole and the electron spin can cancel out with each other [10,142,145,146]. Possessing the non-Abelian characteristic, Majorana fermion manipulation is a promising route for realizing topological quantum

computation [13].

## 2.4.1 Majorana bound states in the 1D system

The common goal of these models is to fabricate a spinless, time-reversal breaking $p$-wave pairing superconducting state [9,147]. Such system can be achieved by combining $s$-wave superconductivity, Rashba SOC, and an out-of-plane magnetic field [148]. A more concise system was later proposed by Klinovaja *et al.* by placing ferromagnetic atomic chains on a $s$-wave superconductor [18]. In this prototype, a helical spin texture arises on the chain through RKKY interaction, resulting in an equivalent $p$-wave pairing.
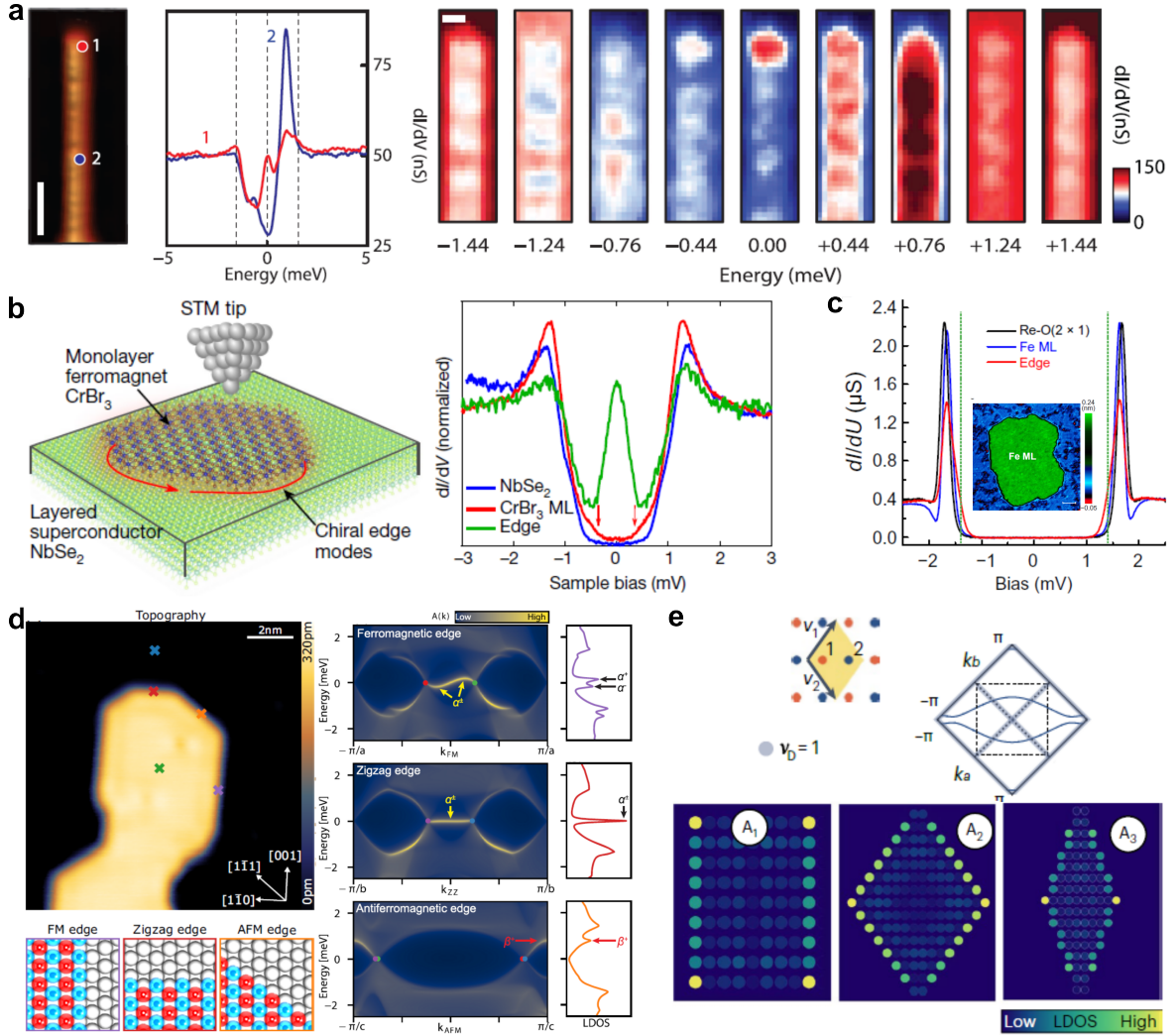
The experimental realization of the aforementioned model has accomplished by the STM/STS investigation through constructing magnetic atomic chains on a superconducting substrate (Fig. 2.15a) [19–21, 149]. With STS measurements, TSC is demonstrated as Majorana zero modes (MZMs), which can be identified by a conductance peak at zero energy in a $dI/dV$ spectrum at the system boundary which also mark the system topology [22]. For the 1D atomic chain, MZMs arise at two ends of the chain, also known as *Majorana bound states (MBSs)*.

## 2.4.2 Chiral Majorana modes in the 2D system

In 2D systems, MZMs can be realized by growing ferromagnetic islands *via* epitaxy on a $s$-wave superconductor (Fig. 2.15b, c) [150,151]. Different from the 1D case, in which MBSs appear as a pair and bound to both ends of the chain, in the 2D system, MZMs propagate along the topological edge, also known as *chiral Majorana modes.* Although having the antiferromagnetic nature, Mn islands grown on the Nb(110) superconductor also exhibit chiral Majorana modes. Depending on spin coupling patterns at different Mn island edges, MZM signatures on $dI/dV$ spectra vary from a single peak pinned at zero-energy to pairs of peaks symmetric to $E_F$ (Fig. 2.15d) [152].

In addition to epitaxial growth of magnetic islands, chiral Majorana modes can also be realized by constructing magnetic islands atom-by-atom through tip-manipulation [153], or by molecular self-assembly [154]. Such constructed spin lattices have larger lattice parameters than that of magnetic films. The YSR impurities then hybridize *via* the RKKY interaction. The resulting Shiba bands propagate throughout the island [135, 155]. This type of spin lattice is also called a *Shiba lattice.*

In such Shiba lattices, MZMs emerge at boundaries of the islands [153,156] (Fig. 2.15e). The topology class of the Shiba lattice can be indexed by the Chern number. With different Chern numbers, multiple MZMs could arise, where each pair propagates along the topological edges in opposite directions, also known as "chiral" MZMs. In a $dI/dV$ spectrum, chiral MZMs show multiple low-energy peaks with equal spacing symmetric to $E_F$ [156].

**Figure 2.15:** *Experimental realization of MBSs and MZMs under the STM and STS investigation.* ***a,*** *A Fe chain is constructed by tip-manipulation on the Pb(110) superconductor. A zero-bias conductance peak is found at two ends of the chain. Reprinted with the permission from [19].* ***b,*** *A CrBr₃ island grown on the superconducting NbSe₂ shows a broad zero-bias conductance peak at the island edge. Reprinted with the permission from [151].* ***c,*** *A Fe island fabricated on the superconducting Re(0001)-O(2×1) substrate shows Majorana edge modes. Reprinted with the permission from [150].* ***d,*** *The antiferromagnetic Mn island grown on the Nb(110) superconductor shows different low-energy modes depending on the spin order at the edge. Reprinted with the permission from [152].* ***e,*** *The spatial distribution of the zero-energy peak is highly dependent on the geometry of the Shiba lattice. In the bottom panel, color dots map the LDOS intensity at zero energy. Reprinted with the permission from [153].*

## 2.5 Summary

This chapter serves as a toolbox of concepts that will be used in the following chapters. We first discuss approaches to fabricate spin lattices *via* on-surface reactions as well as three spin origins that will be investigated later. The interplay between magnetic adsorbates with itinerant electron and with Cooper pairs are also elaborated, with the focus on the SPM research as it is our main investigation technique. Lastly, we introduce topological superconductivity and its 1D and 2D realization under the SPM study, showing signatures of MBSs and MZMs respectively. The topologically protected MBSs and MZMs are robust against the external disturbance, which is considered as a promising route towards topological qubits.

$3$

# Experimental Setup

I N this dissertation, sample investigation is completed by scanning probe microscopy (SPM). Three different microscopes with distinct working temperatures and spectral resolutions are used throughout this project research, which enables a thorough exploration in fundamental physics *via* multiple aspects. In addition to investigation tools, the proper sample fabrication plays a crucial role that validates the sample examination. In this chapter, specifications of three types of SPM and details of sample preparation will be introduced.

## 3.1 4 K STM/AFM

To resolve the bond structures of organic nanostructures, it is essential to reduce lattice vibrations and surface diffusion by decreasing the sample temperature. We thus use a 4 K STM/AFM purchased from Scienta Omicron GmbH (Fig. 3.1a). The cryostat is composed of an outer and an inner tank, filled with liquid nitrogen ($LN_2$) and liquid helium (LHe) respectively. The 4 L LHe bath cryostat is able to cool down the sample to about 4.7 K and stay at this temperature for 16 hours after each LHe and $LN_2$ refill [157]. In addition to the LHe temperature, the measurement can also be done at $LN_2$ temperature ($\approx 77$ K) or room temperature [157]. The measurement is carried out with the controlling software and electronics provided by Nanonis RC5-SPECS.

The 4 K STM/AFM is composed of a preparation chamber and an analysis chamber, separated by a gate valve. The preparation chamber is mounted with a $Ar^+$ sputtering gun and evaporators for depositing molecules and atoms (Fig. 3.1b). The pressure of the preparation chamber is kept around $10^{-9}$ mbar throughout the preparation process to prevent heavy contaminations. After preparation, the sample is transferred to the analysis chamber for investigation using a manipulator. Methods of sample preparation will be discussed in Section 3.4-3.6.

In the analysis chamber, the pressure is kept at about $10^{-11}$ mbar. To maintain
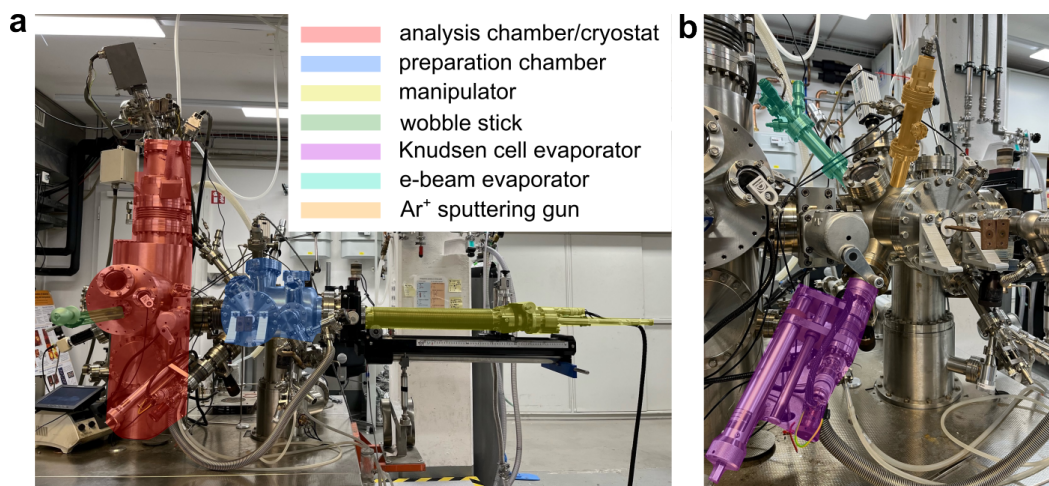
**Figure 3.1:** *Photos of the 4 K STM/AFM. **a,** An overview photo of the 4 K STM/AFM. **b,** A zoom-in photo of the preparation chamber, showing the $Ar^+$ sputtering gun and different types of evaporators.*
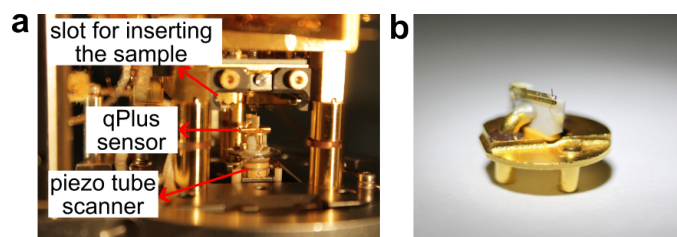


**Figure 3.2:** *Photos showing the scanning stage and the qPlus sensor. **a,** The scanning stage is hanging inside two layers of cylindrical shutters. In the 4 K STM/AFM, a qPlus sensor is placed above the piezo tube scanner for sample investigation. **b,** A zoom-in of a qPlus sensor. A W-tip is attached on the quartz tuning fork.*

the sample at low temperature during scanning, the scanning stage (Fig. 3.2a) is surrounded and thermally isolated by two layers of shutters. Samples are inserted into and taken out from the scanning stage using the wobble stick. Above the piezo tube scanner, we install a qPlus sensor, which is composed of a tuning fork and a tungsten (W) tip attached to its top (Fig. 3.2b, see Section 1.3.2 for the working principle of a qPlus sensor). The tuning fork has the natural resonance frequency of about 23 kHz and spring constant 1800 N/m. The vibrational amplitude is usually set to 50-60 pm to acquire bond-resolved AFM images. The W-tip is prepared by focused ion beam and is further sharpened by indenting the tip into a metallic substrate to enhance the conductivity and spatial resolution. As mentioned in Section 1.3.3, a CO-functionalized tip is usually used to improve the resolution of the frequency-modulation AFM. A CO-tip is prepared by deposition CO molecules on a cold substrate ($< 10$ K) with the chamber pressure about $1 \times 10^{-7}$ mbar, and then gently dipping the tip above a CO molecule. A successful CO-tip preparation shows a current jump during either the dipping or the retracting process, since CO attachment can largely reduce the conductivity of the tip.

## 3.2 Joule-Thomson STM/AFM
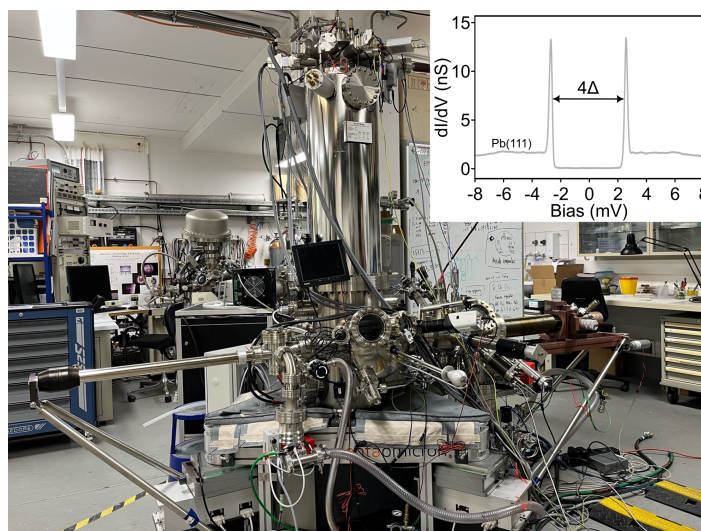


**Figure 3.3:** ***The JT STM/AFM microscope.*** *The figure shows the JT STM/AFM microscope, as well as an exemplary superconducting gap spectrum acquired with a superconducting tip after the improvement of the electronic noise ($I_t =$ 300 pA, V = 8 mV, $A_{mod} =$ 50 $\mu V$).*

Although the 4 K STM/AFM is able to reveal molecular structures with spatial resolution down to the atomic level, investigating bound states generated by a local spin on a crystalline substrate requires a higher spectral resolution. We thus implement another microscope – TESLA Joule-Thomson (JT) STM/AFM purchased from Scienta Omicron GmbH. JT STM/AFM is able to lower the temperature to 1 K through the JT cooling, and stay at 1 K for more than 120 hours with 11 L of L$^4$He and 22 L of LN$_2$ after each refill [158]. The microscope also possesses a vertical magnetic field up to 2.2 T. The main components of JT STM/AFM are similar to that of 4 K STM/AFM (Fig. 3.3), yet efforts were put to reduce the noise and improve the spectral resolution. First, the mechanical vibration is reduced by damping legs purchased from TableStable. To eliminate the electronic noise that hampers the d$I$/d$V$ spectral resolution, we install an I/V converter from Basel Instruments for the current line, and a home-built voltage divider and a $\pi$-filter to the voltage line. The radio frequency noise is further removed by re-wiring the ground loop between the microscope and the Nanonis electronics into "star ground".

To probe low-energy states, such as Yu-Shiba-Rusinov states (see Section 2.3.3), a much higher energy resolution is required for d$I$/d$V$ spectra. Under the constraint of the working temperature, in this dissertation, we utilize a superconducting Pb-tip to better resolve these in-gap states. A Pb-tip is prepared by cutting a short segment of Pb wire, dipping into pure acetic acid for primary cleaning, and followed by several cycles of Ar$^+$ sputtering for oxide removal. The sharpness and superconductivity of the Pb-tip are then adjusted by indenting into the Pb(111) substrate, ensuring the superconducting gap width on Pb(111) to be 4$\Delta$ as shown in the inset of Fig. 3.3.

# 3.3 Dilution Refrigeration STM
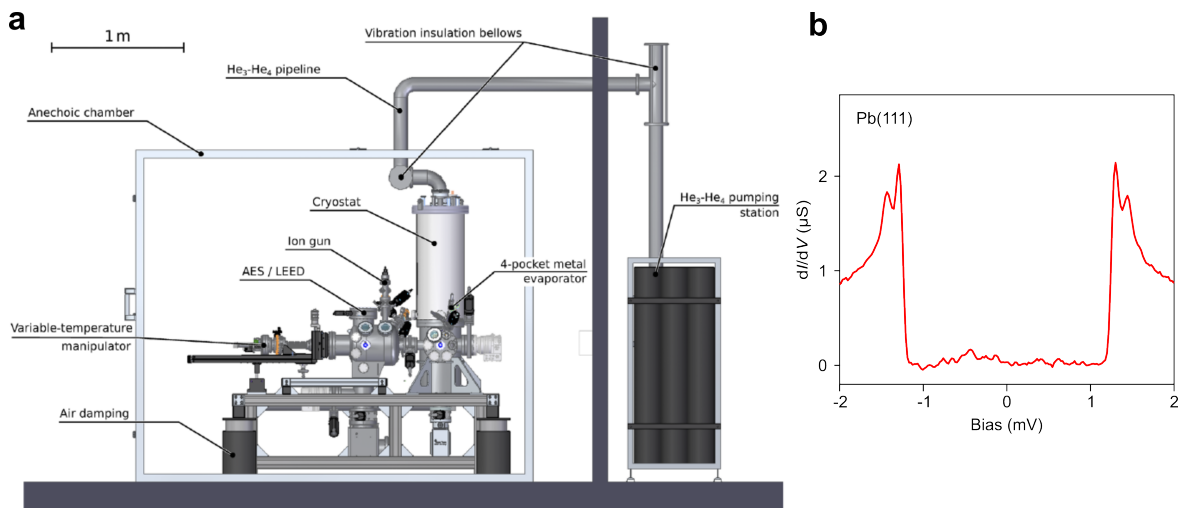


**Figure 3.4:** ***The dilution refrigeration STM built in Karlsruhe Institute of Technology. a,*** *An illustration that demonstrates the overall setup of the dilution refrigeration STM. The figure is reprinted from [159].* ***b,*** *An exemplary spectrum acquired at 35 mK with a W-tip shows double-gapped superconductivity on Pb(111) [44] ($I_t$= 50 pA, V = 2.5 mV, $A_{mod}$= 40 μV).*

The implementation of a superconducting tip at 1 K is able to reveal YSR states, however, due to the convolution with tip DOS and thermal broadening, it could be difficult to discern multiple pairs of YSR states and near-zero energy states. To better resolve these low-energy states, we use the STM equipped with a dilution refrigerator built in Karlsruhe Institute of Technology (Fig. 3.4a) [159]. Dilution refrigeration relies on the circulation of the $^3$He-$^4$He gas mixture, which undergoes repeating condensation and evaporation processes. *Via* multiple cooling processes, below 10 mK can be reached at the mixing chamber [159], which can cool down the sample to the base temperature ($\approx$ 35 mK). When being stabilized at the base temperature, the LHe consumption is lowered and can stay for 59 hours [159]. To reduce the extra mixture loss for cooling down the hot sample, as-prepared samples are first pre-cooled to about 90 K on the LN$_2$ shield before inserting into the scanning stage.

At millikelvin temperatures, thermal broadening is largely reduced, enabling the energy resolution about 25 μeV on a d$I$/d$V$ spectrum [159]. Figure 3.4b shows an exemplary superconducting gap spectrum of Pb(111) probed with a metallic tungsten (W) tip. The two-band superconductivity of Pb is able to be revealed under this working condition [44].
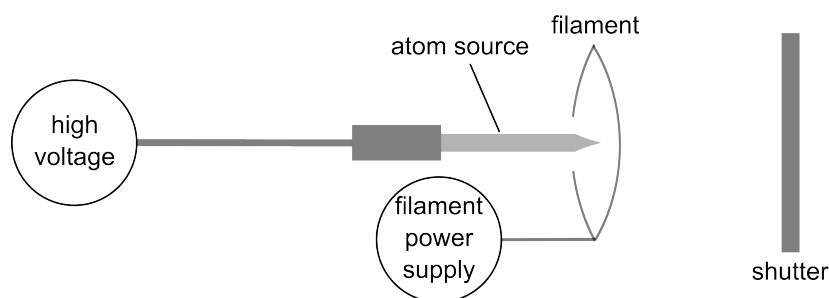
**Figure 3.5:** *A schematic plot of an e-beam evaporator. The rod atom source is placed at the center of a filament, and a high voltage is supplied directly to the source to provide desired flux.*

## 3.4 Atom/Molecule Deposition

### 3.4.1 Atom deposition

Atoms are evaporated on the target substrate through an e-beam evaporator EFM3 purchased from Focus GmbH. As plotted in the scheme (Fig. 3.5), the atom source is placed at the center of a W filament, which is supplied by a current to ionize atoms due to the potential difference. A high voltage is then applied to the atom source to produce a sufficient flux. The relative position between the filament and the atom source is calibrated by applying 200 V of high voltage with measured 5 mA of emission current. During the atom evaporation, the water cooling with the flow rate larger than 0.5 l/min is required to keep the evaporator temperature around 30°C.

There are two atom sources used in this dissertation. First, the silver (Ag) source is provided by a 2 mm diameter Ag rod with 99.99% of purity. The Ag source is used for fabricating Ag films with designated thickness. Secondly, the iron (Fe) source is also provided by a rod with 2 mm in diameter, which is used for depositing single atoms.

### 3.4.2 Molecule deposition

Molecules are evaporated on substrates through a three-pocket Knudsen cell. Dry molecule powder is placed in a quartz crucible wrapped by a W filament. By heating the crucible above the molecule sublimation temperature, molecules are then sublimed from the crucible in the conical pattern. The flux of the molecule evaporation is monitored by a quartz micro-balance (QMB).

Three different organic molecules are carefully examined in this dissertation. First, 10,10'-dibromo-9,9'-bianthracene (DBBA) (Fig. 3.6a) are sublimed at 170°C with the flux of 1.38 Å/min. DBBA is a well-studied monomer for performing Ullmann-type reaction. In Chapter 4, we use DBBA precursors as the first attempt to synthesize atomically precise NGs on a superconducting substrate. Secondly, pyrene-4,5,9,10-tetraone (PTO) (Fig. 3.6b) is sublimed at 150°C with the flux 2.7 Å/min on the
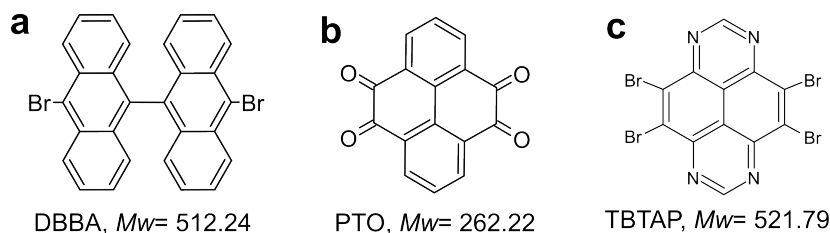
**Figure 3.6:** *The chemical structures of molecules used in this thesis.* **a,** *The chemical structure of 10,10'-dibromo-9,9'-bianthracene (DBBA), which is used to perform on-surface synthesis of NGs.* **b,** *The chemical structure of pyrene-4,5,9,10-tetraone (PTO), which is able to coordinate with magnetic atoms through electron affinity.* **c,** *The chemical structure of 4,5,9,10-tetrabromo-1,3,6,8-tetraazapyrene (TB-TAP), which is a designed electron acceptor.*

preheated Ag(111) and Pb(111) substrates. Due to the strong electron negativity of ketone groups, PTO is able to coordinate with magnetic transition metal elements and form chain structures. Characterization of such organometallic system will be presented in Chapter 5. Lastly, as will be demonstrated in Chapter 6, we evaporate 4,5,9,10-tetrabromo-1,3,6,8-tetraazapyrene (TBTAP) (Fig. 3.6c) at 170°C with the flux 1.3 Å/min on the cold Pb(111) surface ($\approx$ 200 K). TBTAP is a carefully designed electron acceptor, which is able to capture one electron from the substrate while being decoupled intrinsically due to Br substitutes. The alternating charged and non-charged TBTAP rows exhibit exciting physical properties which are promising for fabricating topological qubits.

## 3.5 Preparation of Metal Substrates

In this dissertation, we use the Ag(111) and lead (Pb) (111) single crystalline substrates purchased from MaTeck GmbH with readily polished surfaces. Both Ag and Pb are face-centered cubic (FCC) crystals, with the melting point 961.78 and 327.46°C respectively [160].

Since SPM is the main technique we use to characterize our samples, there is a high demand in a conducting sample with a smooth surface to prevent damaging the probe. It is thus necessary to adequately remove oxides on the surface before scanning. In our work, the cleaning process of substrates is performed in the preparation chamber under UHV ($\approx 10^{-9}$ mbar) in order to achieve contaminant-free surfaces. The substrate first undergoes argon ion (Ar$^+$) bombardment for 10 minutes to efficiently remove surface oxides. Ar gas is ionized with the filament and accelerated by a high voltage of 1 kV. Following Ar$^+$ sputtering, the surface of the substrate is flattened by annealing to 360°C for Ag(111) and 137°C for Pb(111). The annealing of both substrates are done with the built-in heater on the manipulator. In 4 K STM/AFM and the dilution refrigeration STM, the manipulator is equipped with an e-beam bombardment heater, which heats up the sample by accelerating electrons emitted from the filament placed

at the back side of the sample. The heater in JT STM/AFM can provide a much lower heating rate to the sample through radiative heating using pyrolytic boron nitride.

## 3.6 Preparation of the Nb(110) Substrate

Niobium (Nb) is a body-centered cubic (BCC) crystal, which has {110} as the close-packed plane. In this dissertation, we focus on the superconducting nature of Nb below its critical temperature ($T_c \approx 9.2$ K). Under the working temperature, Nb becomes a type-II and one-band conventional superconductor. The $T_c$ of Nb is relatively high compared to other single-element conventional superconductors such as Pb ($T_c \approx$ 7.2 K), vanadium ($T_c \approx 5.4$ K), or aluminium ($T_c \approx 1.2$ K) [160]. Moreover, the superconducting gap width of Nb(110) is estimated to be $2\Delta \approx 3.0$ meV [161], which is larger than its counterparts. Combining all of these intrinsic properties, Nb is an ideal superconductor to investigate possible in-gap states with our microscopes.

### 3.6.1 Radio-frequency heater
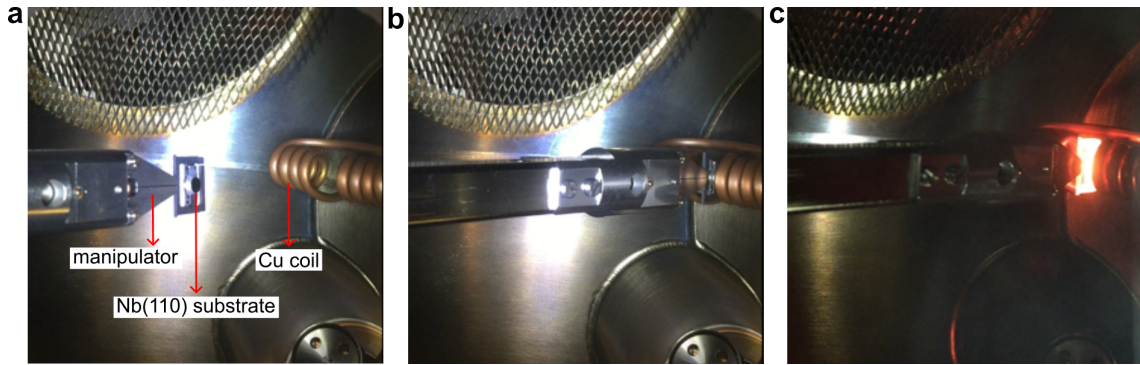


**Figure 3.7:** *Pictures illustrating the operation of RF heating on the Nb(110) substrate.* *a,* *The picture shows the setup of the RF heating. The Nb(110) sample plate is grabbed by a water cooled wobble stick.* *b,* *The sample is inserted into the slit of the Cu coil, being ready for annealing.* *c,* *RF heating is able to heat the Nb substrate to temperatures higher than 1600° C with a power of 2 kW.*

Although Nb is an ideal superconductor for the study in this thesis, the high melting point of Nb ($\approx 2477°$C) makes it difficult to obtain atomically clean surfaces with the annealing approach described in Section 3.5. It is found that the annealing temperature higher than 2200°C is needed to remove surface oxides after Ar$^+$ sputtering [162]. The heater with electron bombardment as described in Section 3.5 cannot reach such a high temperature in short time without losing UHV. Therefore, we develop a radio-frequency (RF) induction heating using copper (Cu) coils (Fig. 3.7), which provide temperature $\geq$ 1600°C with a full power of 2 kW and the output frequency of one hundred-and-tens Hz, depending on the matching with the Cu coil. An upgrade of the RF generator to 10 kW is also possible.

Figure 3.7 shows the setup and the operation of the home built RF heater. The Nb(110) substrate is spot welded onto a tantalum (Ta) plate, which is a material that has a higher melting point (3017°C) than Nb to sustain the high annealing temperature. To avoid heavy degassing, the sample plate is deliberately cut, the manipulator and the Cu coil are water cooled, allowing the pressure kept bellow $5 \times 10^{-8}$ mbar while annealing.

## 3.6.2 Nb-O reconstruction
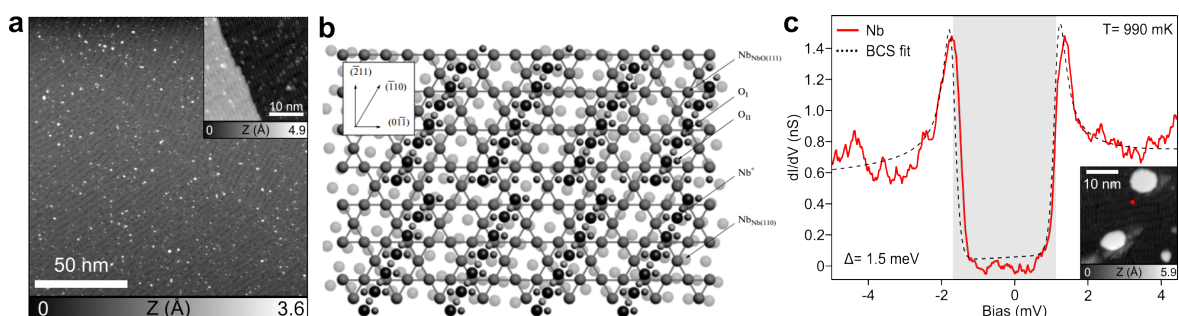


**Figure 3.8:** *The superconducting state of the oxide-reconstructed Nb(110) substrate.* ***a,*** *The pristine Nb(110) surface after cleaning. The inset is a zoom-in of the surface. The texture of short rods indicates the Nb-O reconstruction ($I_t$= 1 pA, V = -1 V. Inset: $I_t$= 1 pA, V = -150 mV).* ***b,*** *The model showing the NbO(111) terminated Nb(110) surface. The figure is reprinted from [163].* ***c,*** *The superconducting gap of Nb is measured by a metallic tip at the position of the red dot in the inset ($I_t$= 100 pA, V = 10 mV, $A_{mod}$= 80 μV). The shaded area marks the superconducting gap with the width of 2Δ. The inset is a STM image of Nb(110) with 0.11 ML of Ag ($I_t$= 100 pA, V = 1 V).*

The Nb(110) substrate was prepared by $Ar^+$ sputtering and followed by cycles of heat flash and cooling. RF heating is able to remove bulk oxides from Nb(110), however, as shown in Fig. 3.8a, textures of short rods observed on the surface indicate a certain surface reconstruction. Due to the insufficient annealing temperature, oxygen (O) embedded in the bulk is able to diffuse to the surface, and forms rod-like Nb-O reconstruction [164]. From previous studies, the reconstruction has the FCC NbO(111) structure [163, 164]. Furthermore, additional Nb rows arranged along the NbO⟨110⟩ direction exhibit the rod pattern (Fig. 3.8b), which has about 5° of misalignment from the Nb⟨111⟩ of the Nb(110) plane.

Nevertheless, the oxide reconstruction does not influence the superconductivity. The superconductivity of Nb(110) was examined with a metallic tip on the sample with less than 1 monolayer (ML) of Ag (red dot in the inset of Fig. 3.8c), which shows a BCS lineshape (Fig. 3.8c). The spectrum is fitted with the thermal-broadened BSC function as described in Section 2.3.1. The fitted Δ= 1.5±7.3×$10^{-7}$ meV, which agrees to the ideal superconducting gap of Nb.

### 3.6.3 Ag film growth on Nb(110)
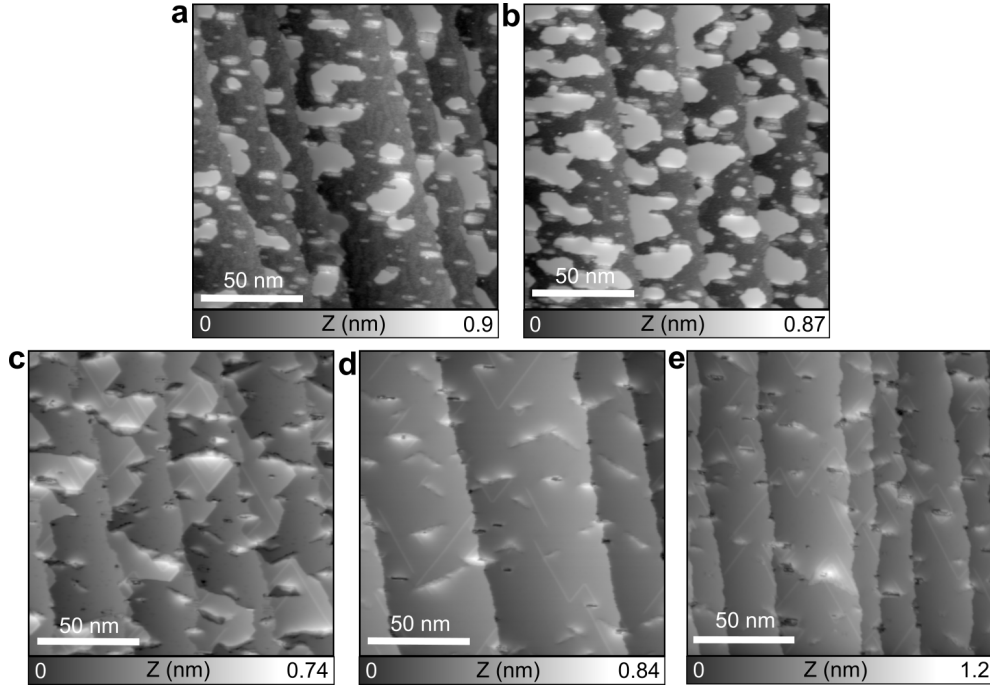


**Figure 3.9:** *STM images of different Ag coverages obtained by adjusting the Ag deposition time.* ***a,*** *2 minutes 30 seconds ($I_t$= 1 pA, V = -100 mV),* ***b,*** *5 minutes ($I_t$= 1 pA, V = -100 mV),* ***c,*** *20 minutes ($I_t$= 1 pA, V = -100 mV),* ***d,*** *30 minutes ($I_t$= 1 pA, V = -80 mV),* ***e,*** *1 hour ($I_t$= 1 pA, V = -80 mV). Terraces are tilted upward in all images to have a better contrast.*

As will be discussed in Chapter 4, we demonstrate the first attempt to synthesize NGs directly on a superconducting substrate. In order to realize this, a substrate possessing low reactivity and superconductivity is needed. Inspired by Tomanic *et al.* [161], we grow homogeneous Ag buffer layers on Nb(110) to obtain an inert surface while maintaining superconductivity *via* proximity effect. Ag films are grown on the Nb(110) surface kept at room temperature through e-beam evaporation (see Section 3.4.1). Typical evaporation is about 30 min for a measured flux of about 30-40 nA. After Ag deposition, the sample is annealed with the RF heater to 550°C for 15 minutes in order to obtain flat and extended Ag monolayers.

To characterize the two-dimensional (2D) growth of Ag films on Nb(110), we keep the Ag evaporation flux and the subsequent annealing process unchanged, and adjust the Ag deposition duration. The Ag coverage is calculated by the software Gwyddion, which shows 21% and 42% of coverage for Fig. 3.9a and Fig. 3.9b respectively. The linear relation between the coverage and the deposition time enables intuitive estimation of the Ag film thickness. Thus, the Ag thickness in Figs. 3.9c, d and e can be deduced as 1.6, 2.5 and 5 ML respectively. On the surface with full coverage of Ag (Figs. 3.9c-e), we find long triangular lines on terraces, which are considered as the trait of Ag film growth. In addition, defects such as notches at the terrace edge and
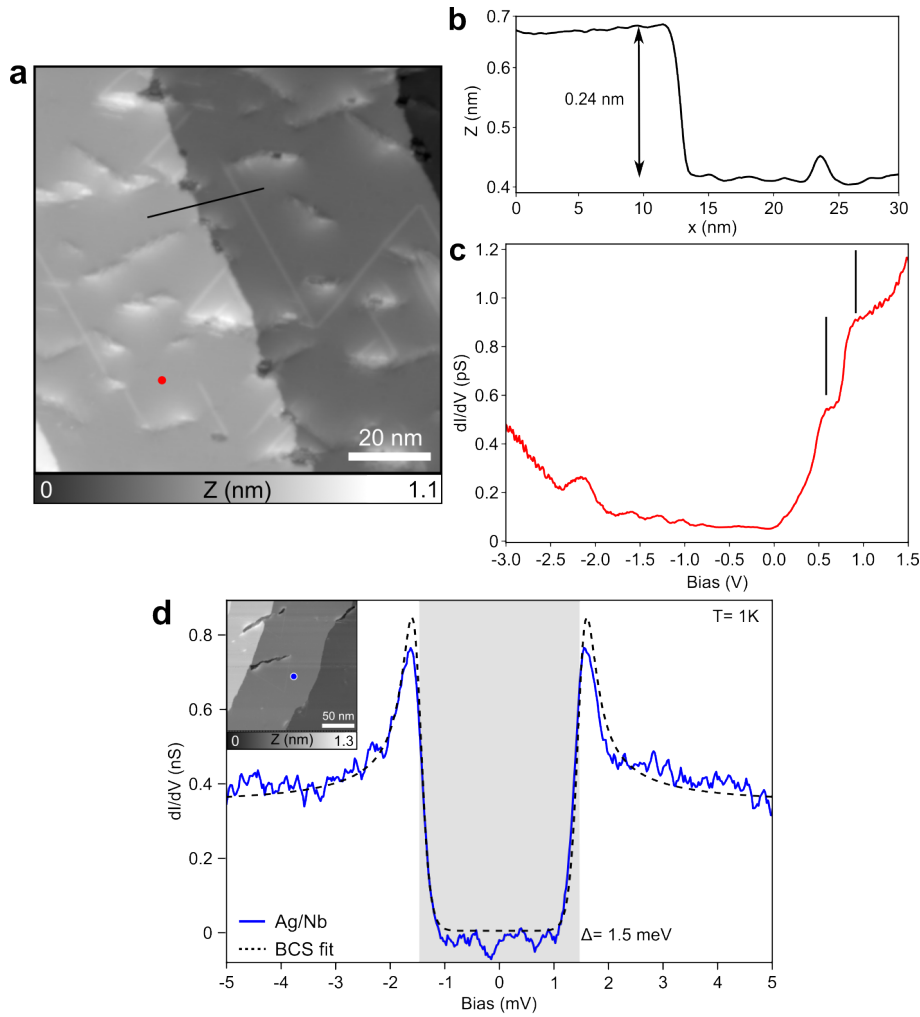
**Figure 3.10:** *Characterization of the clean Ag/Nb substrate with 2.5 ML of Ag.* ***a,*** *The STM image of the clean Ag/Nb surface ($I_t$= 1 pA, V = -100 mV).* ***b,*** *The height profile extracted from the line indicated in* ***a****. The height of a terrace is roughly 0.24 nm, and the triangular line is about 35 pm above the terrace.* ***c,*** *The large scale dI/dV spectrum measured at the position marked in* ***a*** *($I_t$= 1 pA, V = -1 V, $A_{mod}$= 20 mV).* ***d,*** *The superconducting gap measured on the 2.5 ML Ag at the position indicated in the inset ($I_t$= 100 pA, V = 10 mV, $A_{mod}$= 50 $\mu$V. Inset: $I_t$= 100 pA, V = -1 V).*

tiny holes on the terrace are also found on thick Ag.

Since 2.5 ML of Ag provides large and uniform terraces (Fig. 3.10a), most of the on-surface reactions are performed on the Ag layer with such thickness. The height profile extracted from a clean substrate is plotted in Fig. 3.10b. The height of a terrace is approximately 0.24 nm, which is consistent with the theoretical height of a Ag(111) atomic layer (0.24 nm). The triangular line is about 35 pm above the surface. The large range dI/dV spectra in Fig. 3.10c exhibits periodically oscillating peaks in the negative bias, and two steps in the positive bias. These signatures could
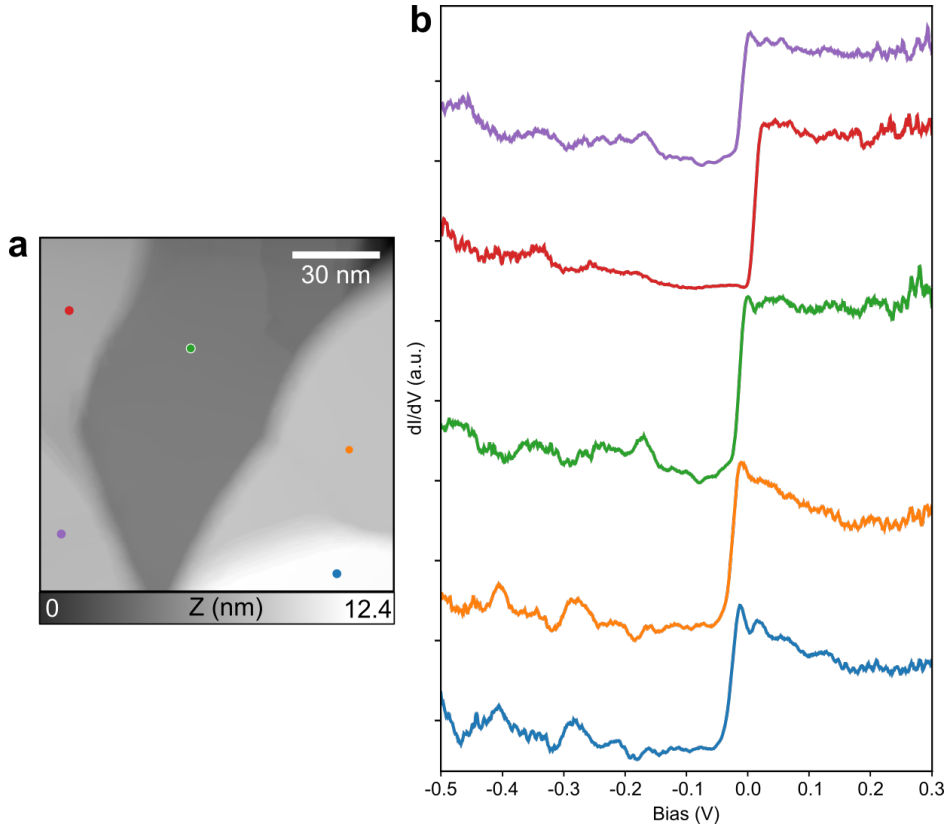
**Figure 3.11: *Characterization of the thick Ag layer grown on Nb(110).* a,** *STM topographic image of the Ag layer showing island growth ($I_t$= 100 pA, V= 800 mV).* **b,** *SS is observed at different positions with the energy at about -10 meV ($I_t$= 100 pA, V = -500 mV, $A_{mod}$= 10 mV).*

be the result of vertical confinement induced by atomically thin Ag, or the lateral confinement due to limited width of the terrace. Figure 3.10d confirms proximity-induced superconductivity on the Ag layer. The superconducting gap obtained with a metallic tip is fitted with the same method as Nb, which has $\Delta$= 1.5±6.3×10⁻⁷ meV.

As the Ag layer grows much thicker than 5 ML, we observe Stranski–Krastanov growth mode on Nb(110) (Fig. 3.11a). On the thick Ag island, surface state (SS) is probed by d$I$/d$V$ at different positions, showing the energy level $E_{SS} \approx$ -10 meV (Fig. 3.11b). Since SS is a characteristic of the noble metal (111) surface [165], we assume this substrate has similar chemical reactivity as Ag(111). However, $E_{SS}$ of the thick Ag island deviates from that of the bulk Ag(111) (about -63 meV [165]), which is very likely the result of the epitaxial strain induced on Ag due to the insufficient thickness [161]. The comparison of the on-surface synthesis on the homogeneous thin wetting layer and the rough Ag island will be discussed in Section 4.1.

49

# 3.7  Summary

In this chapter, three different types of STM/AFM used in this thesis are introduced. By cross-checking samples with different microscopes, we ensure the reproducibility of the results and complete the investigation in diverse aspects. Following the specification of microscopes, details about sample preparation are described. Noteworthy is the novel setup of RF heater which is delicately designed for generating high temperature to clean the Nb(110) substrate. Lastly, a careful calibration of Ag film growth on Nb(110) is presented.

# 4

# On-surface Synthesis of Nanographenes on the Superconducting Ag/Nb(110)

With the bottom-up synthesis through on-surface reactions, atomically-precise nanographenes (NGs) and graphene nanoribbons (GNRs) [71, 72] can host Dirac fermions, topological electronic properties [90, 91, 166], magnetic edge states [72, 167], and coupled spins [92, 168]. Despite considerable efforts to engineer their structures and electronic properties on surfaces, observing the interaction of a superconducting state with graphene local magnetism is scarce in literature [169]. Interestingly, this interaction can lead to further application from strong spin-orbit coupled materials to novel graphene-based topological superconductors [170], which opens a new era for implementing Majorana-based *qubits* in topological quantum computation.

Inspired by the seminal work of Tomanic *et al.* [161], this chapter targets Nb(110) substrates covered with thin Ag buffer layers grown in UHV as a reliable superconducting platform [161]. Using STM and AFM at 4 K, we investigate Ullmann polymerization of 10,10'-dibromo-9,9'-bianthracene (DBBA) precursors. We characterize the synthesized nanostructures by AFM with CO-terminated tips and confirm proximity-induced superconductivity. We believe our results open a new route towards the study of topological superconductivity in atomically-precise NGs.

## 4.1 Nanographene Synthesis

Our aim is to reproduce Ullmann polymerization of DBBA precursors (compound **1** in Fig. 4.1a), which leads to 7-carbon-wide armchair GNRs (7-AGNRs) on Ag(111) [80, 81], on the superconducting Ag/Nb(110) substrate. To achieve this, we first investigate by STM the growth of Ag thin films on the oxide-reconstructed Nb(110) [162] with thicknesses ranging from 0.2 to 5 monolayers (ML) (see Section 3.6.3). Precursor **1** is then sublimated at 170°C to the Ag/Nb(110) substrate kept at room temperature,

# Chapter 4. On-surface Synthesis of Nanographenes on the Superconducting Ag/Nb(110)
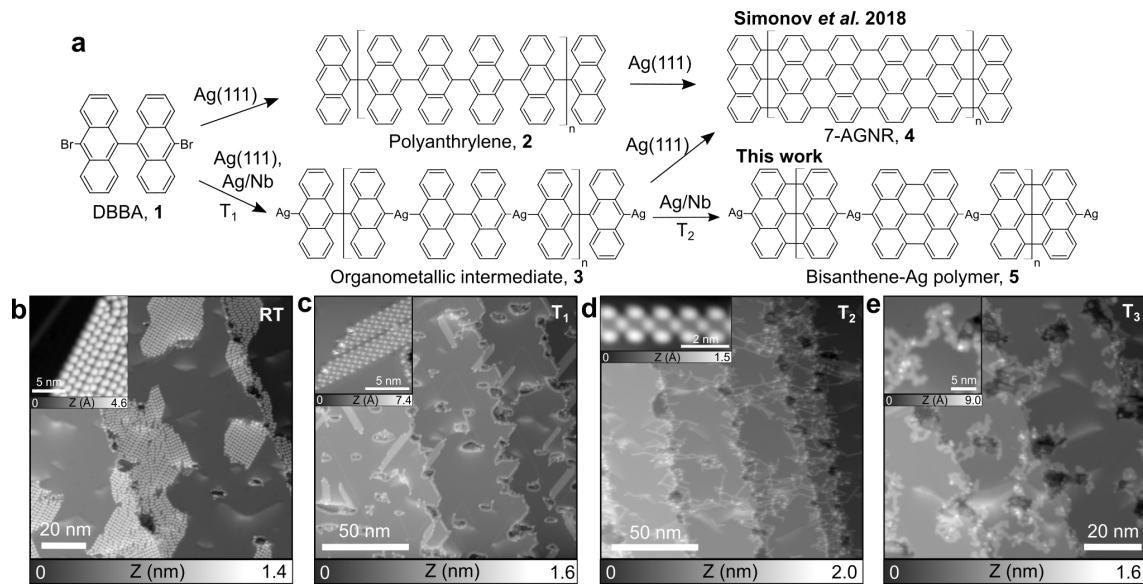


**Figure 4.1:** ***Bottom-up synthesis of NGs on the superconducting Ag/Nb(110) substrate.*** *a, Hierarchical Ullmann polymerization leading to bisanthene-Ag chains as compared to literature.* ***b-e,*** *Series of STM images showing the evolution of surface morphology as a function of substrate temperature.* ***b,*** *Sublimating DBBA molecules (**1**) on Ag/Nb(110) leads to extended two-dimensional self-assemblies ($I_t = 1$ pA, $V = 1.8$ V. Inset: $I_t = 1$ pA, $V = -1.5$ V).* ***c,*** *Upon annealing to $T_1 = 75°C$, molecular domains evolve to one-dimensional stacks of compounds **3** ($I_t = 1$ pA, $V = -1.5$ V. Inset: $I_t = 1$ pA, $V = 900$ mV).* ***d,*** *Annealing to $T_2 = 300°C$ leads to bisanthene-Ag chains **5** ($I_t = 1$ pA, $V = 1.8$ V. Inset: $I_t = 1$ pA, $V = 900$ mV).* ***e,*** *The final thermal treatment to $T_3 = 390°C$ results in small NG domains ($I_t = 1$ pA, $V = 1.9$ V. Inset: $I_t = 1$ pA, $V = 2$ V).*

resulting in 2D self-assembled domains located mostly at step edges and defects (Fig. 4.1b). Upon annealing to $T_1 = 75°C$, dehalogenation of **1** is initiated, forming bundles of chains (Fig. 4.1c). Increasing the sample temperature to $T_2 = 300°C$ then results in single polymeric chains (Fig. 4.1d) while for $T_3 = 390°C$, molecular structures appear more curved and fused. The close-up STM image of each sub-product is shown in the insets of Figs. 4.1b-e. We found the formation of these sub-products are independent of the Ag thickness explored so far.

Interestingly, on the Ag/Nb(110) substrate prepared at a lower temperature about 450°C (comparing to the typical preparation temperature of 550°C), we find coexisting zigzag and armchair chains after DBBA deposition (Fig. 4.2). As will be elucidated with high resolution AFM, we assign both of the configurations to organometallic (OM) intermediate compounds towards graphene nanoribbons (GNRs). Different from the OM intermediate synthesis shown in Fig. 4.1c, the spontaneous conjugation indicates that the energy barrier for forming such intermediates is very low, and it can be overcome by the surface-assisted process on this Ag/Nb(110) substrate. Despite of the different reaction pathway on this substrate, OM intermediates are still able to
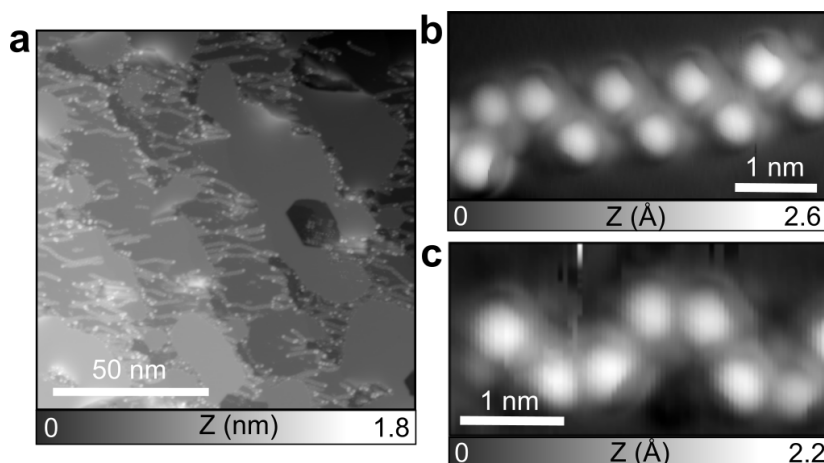
**Figure 4.2:** *Structural characterization of zigzag and armchair intermediates.* ***a,*** *Large scale STM image of the sample where zigzag and armchair intermediates coexist ($I_t$ = 1 pA, V = 1.8 V).* ***b,*** *The close-up STM image of a zigzag chain ($I_t$ = 1 pA, V = 150 mV).* ***c,*** *he close-up STM image of an armchair chain ($I_t$ = 1 pA, V = 150 mV).*

transform to bisanthene-Ag chains by annealing at a much lower temperature estimated to be 150°C.

To better understand the reaction steps, we elucidate the chemical structure of each sub-product using AFM imaging with a CO-functionalized tip [53]. First of all, Figs. 4.3a and b display AFM images of zigzag and armchair chains respectively. Both chain configurations are found as intermediates towards 7-AGNRs on noble metal surfaces [71, 80]. We assign both buckled structures to the formation of OM intermediates **3**, which are composed of bianthracene radicals and Ag surface adatoms. Due to the steric hindrance between anthracene moieties, only the topmost phenyl rings can be resolved by AFM (bold lines in the superimposed Kékulé structures of Figs. 4.3a and b). Our assignment is different from the previous study on Ag(111) using the same precursor [80], in which the zigzag pattern was confirmed as polyanthrylene **2** after successful dehalogenation of **1** and formation of C-C bonds. We attribute the two different buckling patterns of **3** on Ag/Nb(110) to the accommodation to the distorted lattice of thin (2.5 ML) Ag films.

To enforce cyclodehydrogenation towards GNRs, we further annealed the sample to $T_2$ = 300°C. Exemplary STM/AFM images of the resulting product are shown in the inset of Fig. 4.1d and Fig. 4.3c. Surprisingly, cyclodehydrogenation only occurs within each bianthracene moiety, but not between adjacent bisanthene monomers (Fig. 4.3c). By extracting the distance between adjacent bisanthenes, we find the interlinking bond length about 2.51±0.07 Å, which is too long to be a single C-C bond. Moreover, bright protrusions located at the interlinking position in the STM image (inset of Fig. 4.1d) indicate conducting species conjugated in between. Based on these observations, we assign the synthesized structure of Fig. 4.3c to the bisanthene-Ag polymer **5** even though Ag atoms are not clearly resolved by AFM [171]. According to the relaxed
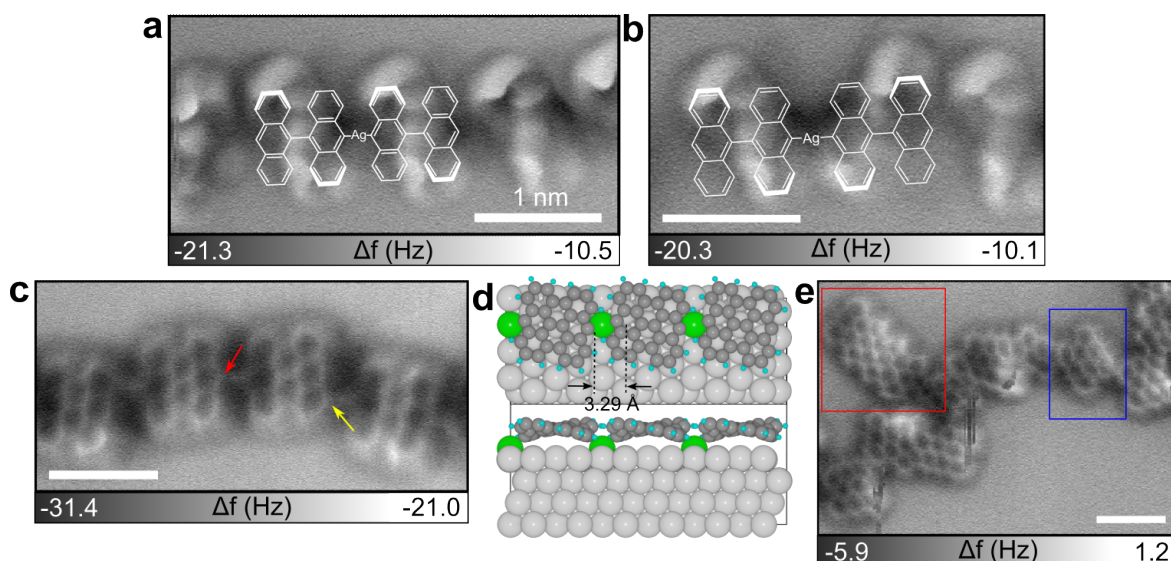
**Figure 4.3:** *Bond-resolved characterization of reaction sub-products. **a,** AFM image of OM intermediates **3** showing a zigzag pattern. **b,** AFM image of the OM intermediates **3** which have an armchair pattern fingerprint in AFM. Bold bonds in the corresponding Kékulé structures of **a** and **b** represent the most protruding part of the chain. Two buckling patterns of **3** might result from the Ag lattice-modulated effect. **c,** AFM image of a bisanthene-Ag chain **5** where each monomer is linked by C-Ag-C bond. **d,** Relaxed structure of the OM intermediate on Ag(111) optimized by DFT. The DFT simulation result shows the distance of 3.29 Å between bisanthene moieties. **e,** AFM image of the irregularly fused bisanthenes (blue) leading to small 7-GNR segments (red) as well as irregular structures. All scale bars are 1 nm.*

structure of **5** on Ag(111) optimized by density function theory (DFT) (Fig. 4.3d), surface Ag atoms are pulled out, yielding a distance of 3.29 Å between middle peripheral carbons of adjacent bisanthene monomers. This distance is still much larger than our measured bond length (2.51 Å), which might be explained by different lattice configurations of thin Ag films and Ag(111). Besides, the shorter bond length may be caused by intrinsic limits of the AFM technique, such as the tilted CO molecule at the tip apex [56] and slight drift during the slow scan.

With the confirmation of **5**, we stress that intermediate **2** is unlikely to be synthesized at this step of the reaction, since breaking a strong C–C bond between anthracene moieties and forming a much weaker OM (C–Ag) bond is not energetically favorable. Furthermore, bisanthenes are interlinked not only from the middle of the bisanthene edge (red arrow in Fig. 4.3c) but also from the peripheral carbons (yellow arrow). This observation allows us to conclude that surface Ag atoms of Ag/Nb(110) are involved in the reaction, causing the Ullmann-type reaction competes with surface-assisted dehydrogenative coupling (non-Ullmann). Noteworthy is the synthesis of **5** from DBBA precursors on Ag/Nb(110), which is novel compared to previous studies on Ag(111), suggesting that these two substrates do not share the identical catalytic reactivity [80, 81].
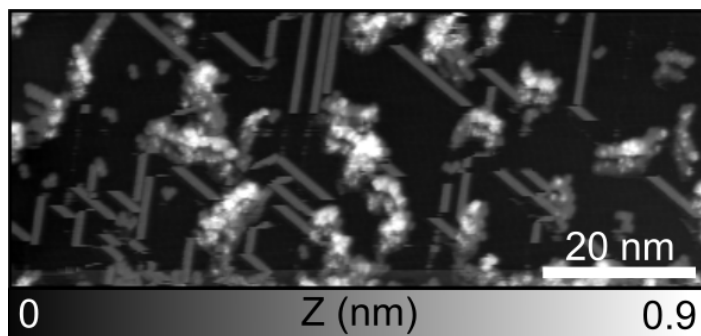
**Figure 4.4:** *The STM image of products synthesized on the thick Ag layer. Stripe-like structures are synthesized on the thick Ag after the slow annealing process that could be attributed to GNRs ($I_t$= 100 pA, V = 1 V).*

Annealing the sample to $T_3$= 390°C promotes a cyclodehydrogenation reaction between neighboring bisanthene monomers, leading to dendritic structures (Fig. 4.1e) instead of straight GNRs. These structures consist of irregularly-fused bisanthenes or short GNR segments according to AFM imaging (Fig. 4.3e), which are similar to those obtained using chlorinated precursors on Au(111) [77]. We suggest that the Ag coordination between bisanthene monomers prevents the conventional Ullmann reaction (Fig. 4.1a) and promotes alternative cyclodehydrogenation processes. Note that we are aware that kinetic factors such as annealing temperature of the substrate [80] or heating rate [81] are key parameters that can influence the reaction towards extended GNRs. We explored various preparation procedures but no significant improvements of Ullmann reaction sub-products nor the formation of extended GNRs have been observed on top of thin Ag film. However, on thicker Ag buffer layers ($\geq$ 5 ML), we observed a Stranski–Krastanov growth mode with the formation of large Ag islands [161] (see Section 3.6.3 Fig. 3.11) on top of which premises of GNR reaction has been obtained with slow annealing rate (Fig. 4.4). We thus think that the epitaxial deformation in thin Ag buffer layer containing many surface dislocations (see Section 3.6.3 Fig. 3.9d) leads to a substantial amount of Ag adatoms during annealing for the GNR synthesis. Nevertheless and despite the large involvement of the substrate in the Ullmann reaction, short segments of 7-AGNRs on the thin Ag layer can be occasionally found as marked by the red rectangle in Fig. 4.3e.

## 4.2 Spectral Analysis

### 4.2.1 Spectra on bisanthene-Ag chains

Next, we performed scanning tunneling spectroscopy (STS) on **5** and fused NGs to gain an in-depth understanding of their electronic properties in combination with DFT calculations. The superconducting states on **5** was confirmed at 1.3 K with a metallic tungsten tip (Fig. 4.5a). The overall shape and gap width of the fits using BCS on **5** are almost identical to that measured on the Ag/Nb(110) substrate, which implies
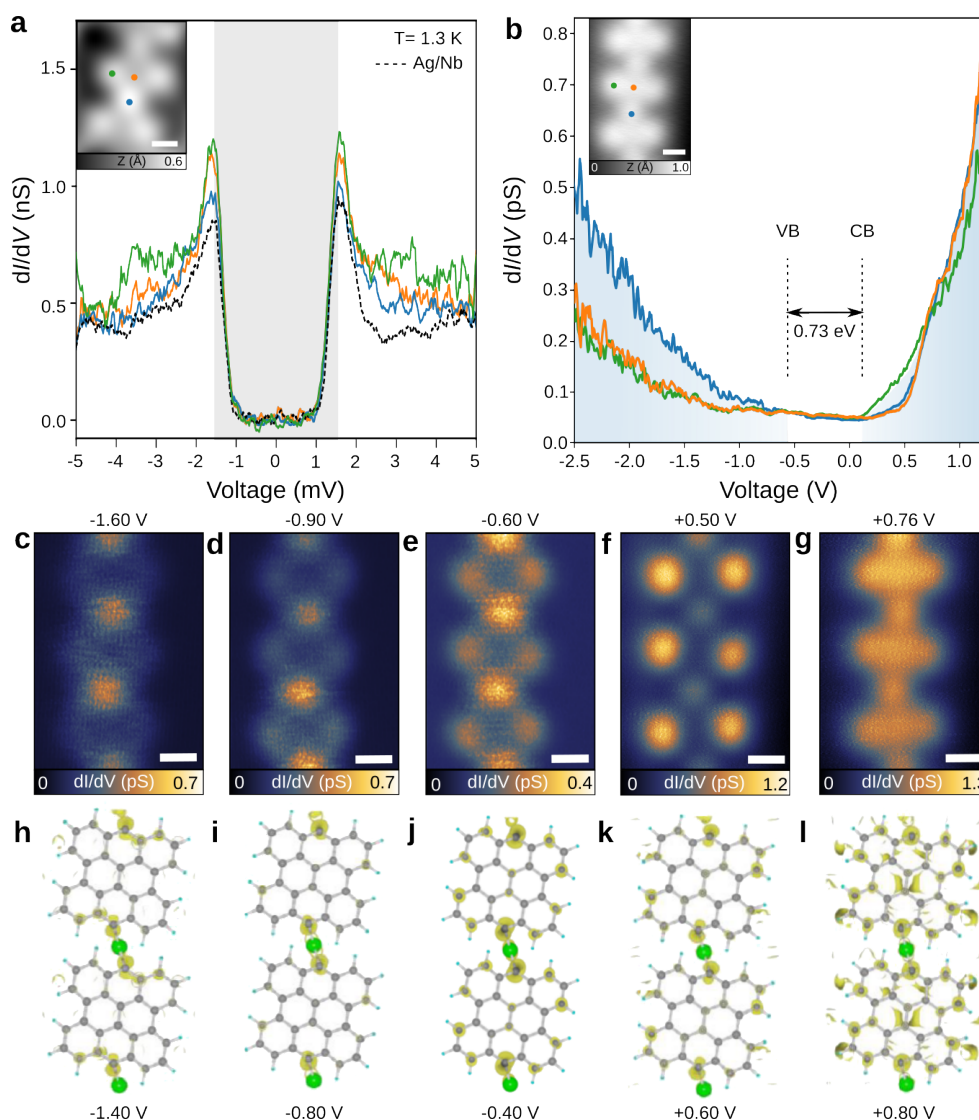
**Figure 4.5:** *Experimental and simulated electronic properties of bisanthene-Ag chains 5. a, Proximity-induced superconductivity on 5 at different positions marked in the inset ($I_t$= 100 pA, V = 10 mV, $A_{mod}$= 50 mu V. Inset: $I_t$= 20 pA, V = 760 mV). Dashed line corresponds to a representative spectra on pristine Ag/Nb. Shaded area marks the fitted width of the superconducting gap. b, dI/dV spectra measured at three representative positions of the bisanthene chain. Shaded areas refers to the onsets of CB and VB ($I_t$= 1 pA, V = 900 mV, $A_{mod}$= 20 mV. Inset: $I_t$= 1 pA, V = 900 mV). c-g, Series of dI/dV maps at indicated bias. Scale bars of all the images are 5 Å. h-l, Simulated DOS of 5 at different energy levels shows consistency with the experimental results in c-g.*

that the superconductivity state is given by proximity from the underlying substrate is not influenced much by the molecular adsorbates. In addition, a series of differential conductance (dI/dV) spectra and dI/dV mapping were acquired along the central of **5** and across a bisanthene monomer. Figure 4.5b shows three representative dI/dV

spectra acquired at positions marked in the inset. Along the chain axis, a shoulder at +0.76 eV is found on bisanthene monomers (orange) and Ag atomic sites (blue) which is absent at the bisanthene armchair edge (green). The latter has a resonance at +0.13 eV attributed to the conduction band (CB) onset. The frontier resonance of the valence band (VB) onset is assigned to -0.60 eV, allowing to extract an energy gap of about 0.73 eV. In comparison, DFT calculations of the OM structure in gas phase reveal a gap of 1.05 eV in relative agreement with experimental data. Note that the band gap value extracted from STS measurements is typically reduced by an additional electron screening from the underlying metallic surface with respect to the band gap of the gas-phase polymer obtained by DFT [172]. Moreover, due to the heavy orbital hybridization with the substrate, a non-zero DOS around Fermi energy as in Fig. 4.5b leads to reasonable observation of superconductivity on **5**.

The d$I$/d$V$ map acquired at +0.50 eV (Fig. 4.5f) shows an increased DOS over bisanthene edges and at Ag atomic sites while centers of bisanthene units are extinguished. The d$I$/d$V$ map above the VB edge (Fig. 4.5c) shows maxima at Ag atoms and lateral termini of the bisanthene moiety, while the d$I$/d$V$ map acquired at +0.76 eV (Fig. 4.5g) shows a continuous DOS over the entire chain. Despite the fact that DFT calculations cannot predict correctly the magnitude of the intrinsic bandgap of the polymeric chain, we find that the measured DOS of **5** on Ag/Nb(110) has a similar trend to the calculated frontier orbitals of **5** on Ag(111) for the VB and CB band edges (see Figs. 4.5h-l), validating the character of the frontier orbitals predicted by DFT.

## 4.2.2 Spectra of nanographenes

We last discuss the electronic properties of irregularly fused NGs. d$I$/d$V$ spectra acquired at different positions share almost identical line-shape (Fig. 4.6a), allowing a gap estimation of 1.58-1.68 eV. We also carry out STS measurements at 560 mK with a metallic tip to investigate the superconductivity within the NG structure. Superconducting gaps at various positions are estimated by using the BCS function considering thermal broadening as described in Section 2.3.1. They all have identical widths of $\Delta=$ 1.5 meV, being comparable to that on the Ag/Nb(110) substrate (dashed line in Fig. 4.6b). Note that we also observe an increase of the SC coherence peak at the edge of the nanographene (red and blue spectra in Fig. 4.6b) as opposed to the center of the NG (green). Such increase, similar to the one observed for Fe adatom on Nb(110) [173,174], might suggest the presence of a single pair of YSR states, which energetically overlaps with the coherence peaks due to the limited spectral resolution at the measurement temperature. We thus conclude that the NG structure induces a slight modification of the proximity-induced superconductivity from the Ag/Nb(110) substrate, as the result of YSR states likely arising from unpaired electrons at edges of fused bisanthene moieties. This allows us to conclude that the fused NGs on Ag/Nb(110) might contain evidences of carbon magnetism [92], which will be explored in future works.

As for the speculated GNRs shown in Fig. 4.4, according to the work by Tomanic *et*
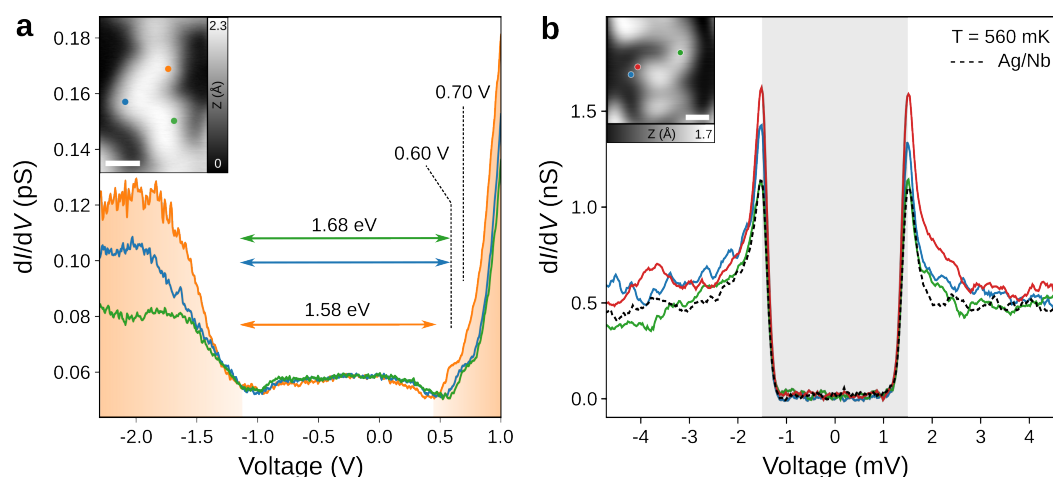
**Figure 4.6:** *Proximity-induced superconductivity in fused NG. a,* $dI/dV$ *spectra showing VB and CB onsets of a NG segment ($I_t$= 1 pA, V = 1.8 V, $A_{mod}$= 20 mV). The STM image of the target NG is shown in the inset ($I_t$= 1 pA, V = 1.8 V). Green, orange and blue dots in the inset refer to positions of dI/dV spectra. b, Superconducting gap measurement at different positions of NG shown in the inset as compared to the pristine Ag/Nb (dashed line) ($I_t$= 100 pA, V = 10 mV, $A_{mod}$= 50 $\mu$V. Inset: $I_t$= 50 pA, V = 1.5 V). The estimated widths of superconducting gaps are highlighted by the shaded area, indicating a robust proximity-induced superconductivity on the NG. Scale bars of the insets are 1 nm.*

*al.* [161], superconductivity is fully proximitized on the surface state for such coverage. We thus reasonably assume that GNRs synthesized on such Ag films might show similar superconducting gap as found on bisanthene-Ag chains and NGs.

## 4.3 Summary

In conclusion, we fabricated a metal-superconductor heterostructure consisting of a Nb(110) substrate covered by thin Ag films, and find robust proximity-induced superconductivity on the Ag layer [161]. In contrast to the reactive Nb surface, we demonstrated by low temperature STM/AFM that the Ag buffer layer is compatible with thermal-triggered on-surface reactions, including surface diffusion of molecules, dehalogenation, formation of C-C intra-monomer bonds as well as cyclodehydrogenation. The presence of surface Ag adatoms from thin Ag buffer layer however change the reaction pathway compared to pristine Ag(111) leading to unexpected NG structures such as bisanthene-Ag polymeric chains or fused nanographene. We propose to use in future experiments iodine substituent instead of bromine atoms in the precursors to promote polymerization on the surface at lower annealing temperature in order to circumvent the formation of organometallic intermediates [175]. As compared to the pristine substrate, bisanthene-Ag polymer and edges of fused nanographene show an increase of the SC coherence peaks which can be attributed to the presence of YSR

states from unpaired electrons in these structures [92]. Our results demonstrate an exciting starting point towards the general exploration of exotic electronic states or carbon magnetism in atomically precise NGs or extended metal-organic frameworks proximitized to a $s$-wave superconductor. This may open new routes towards the emergence of topological superconductivity in carbon-based nanostructures.

*5*

# Substrate Dependent Long-range Spin-spin Coupling in Organometallic Chains

U PON the adsorption of transition metal elements on metallic surfaces, $d$-orbital degeneracy is lifted due to the crystal field imposed by the substrate and ligands. As discussed in Section 2.4.2, fabricating a spin lattice into specific geometries might give rise to topological superconductivity through the coupling with superconducting states. To construct a regular spin lattice, we utilize the directional bonding of functional groups on organic molecules, and coordinate them with transition metal ions.

In this chapter, we fabricate a magnetic organometallic (OM) framework using pyrene-4,5,9,10-tetraone (PTO) and Fe atoms on Ag(111) and on the superconducting Pb(111) [61]. The subsequent structural characterization is carried out by scanning tunneling microscopy (STM) and atomic force microscopy (AFM) at 4 K. Local magnetic features are examined by inelastic tunneling spectra measured at 1 K, which reveals different spin-state excitation mechanisms and distinct long-range spin-spin coupling behaviors on the two substrates.

## 5.1 Fabrication of PTO-Fe Chains

The reaction pathway of the magnetic OM chain on Ag(111) and Pb(111) is depicted as Fig. 5.1a. PTO molecules are first sublimed on the substrate kept at room temperature, resulting in extended 2D domains that are stabilized by hydrogen bonds (Fig. 5.1b). Fe atoms are subsequently deposited on pre-heated Ag(111) to 150°C. Due to the electron affinity between ketone groups and Fe atoms, PTO-Fe coordinated chains are formed as shown in Fig. 5.1c. On Pb(111), since Fe has high tendency of forming clusters with Pb, a reduced amount of Fe is evaporated followed by the PTO deposition, and an annealing process at a much lower temperature ($\approx 115$°C) is then treated to the

**a**



**b**



**c**



**d**
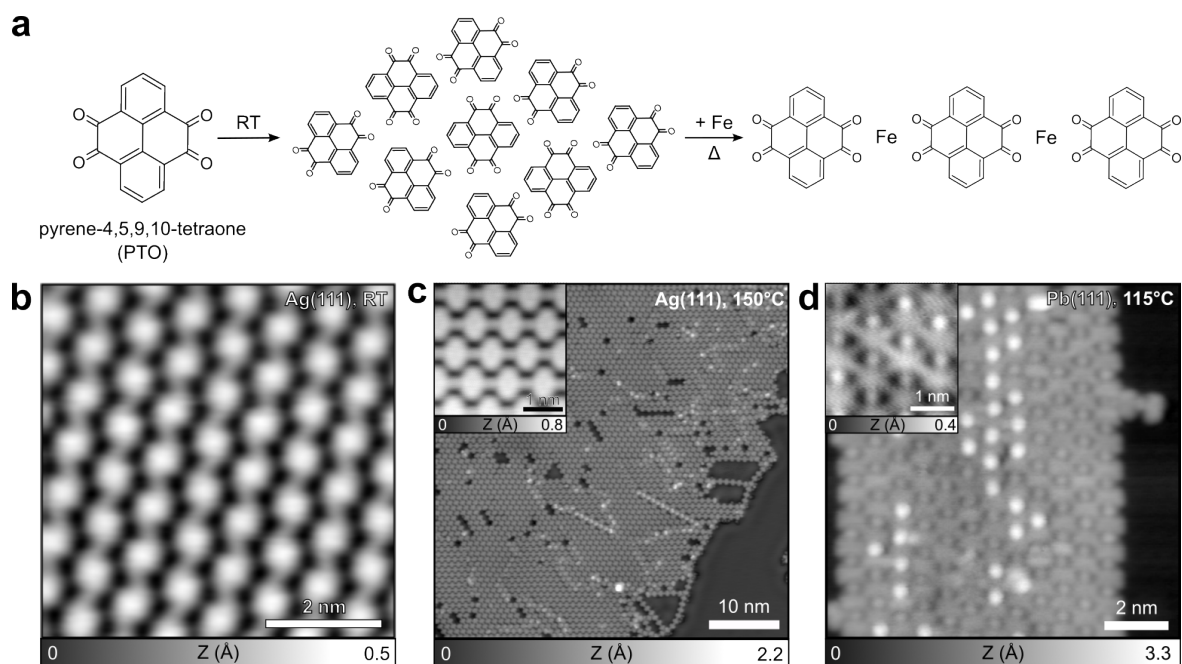


**Figure 5.1:** *On-surface synthesis of PTO-Fe chains on Ag(111) and Pb(111) substrates. **a,** Overview of the reaction pathway. **b-d,** STM images of a PTO assembly and PTO-Fe chains on Ag(111) and Pb(111) respectively. **b,** Sublimating PTO molecules on Ag(111) leads to extended two-dimensional self-assemblies ($I_t$ = 1 pA, V = 500 mV). **c,** After depositing Fe atoms, PTO and Fe are able to form coordinated chains, which further assemble into islands in the close-packed pattern on Ag(111) ($I_t$ = 1 pA, V = 200 mV). **d,** PTO-Fe chains assemble into bundles rather than islands on Pb(111), showing a stark difference from that on Ag(111) ($I_t$ = 80 pA, V = 600 mV. Inset: $I_t$ = 100 pA, V = 50 mV).*

sample. Though the chain structure is expected to be identical on both substrates, PTO on Pb(111) shows obvious diagonal links between two chains while this link on Ag(111) is relatively weak (Fig. 5.1d).

Atomic structures of the PTO assembly and the PTO-Fe chain on Ag(111) are revealed by AFM with a CO-functionalized tip and density function theory (DFT) calculation. As shown in Fig. 5.2a, PTO molecules self-assemble into a rotated arrangement through hydrogen bonds, resulting in an angle approximately 60° between adjacent rows inside the assembly. Interestingly, hydrogen bonds can also lead to parallel arrangement of PTO assemblies, yet it is less energetically favorable on Ag(111) according to DFT calculations (Fig. 5.2c). The subsequent Fe deposition on the heated substrate at 150°C allows metal-coordination with PTO molecules. Bonds between ketone groups and Fe are clearly resolved by AFM, which shows the coordination number of four on Fe (Fig. 5.2b). To clarify the species of the conjugated atom, DFT calculation was performed to compare the energy of Ag- and Fe-coordination (Fig. 5.2d). The simulation shows 5.40 eV more energetically favorable in the Fe-coordinated case over its counterpart.
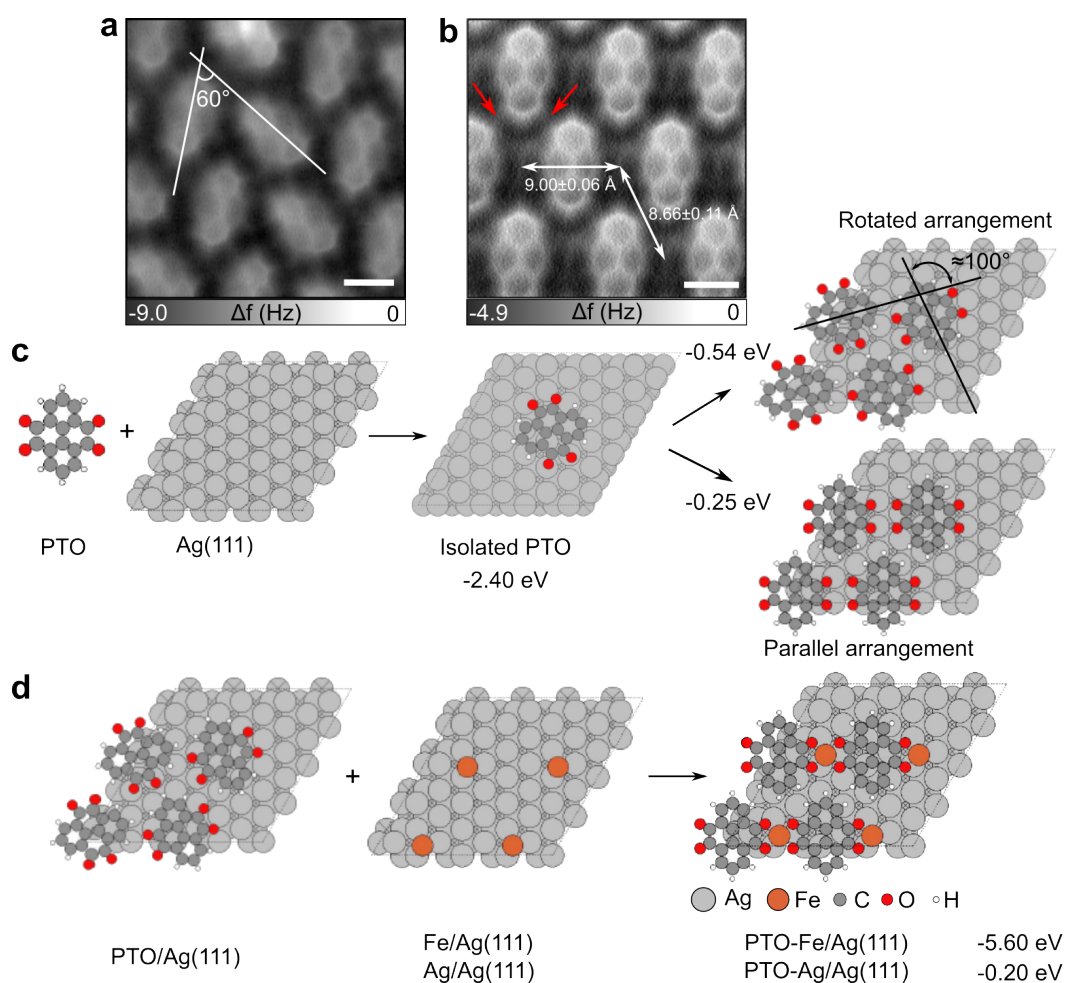
**Figure 5.2:** ***Structural characterization of reaction products. a,*** *The AFM image shows a PTO self-assembly with about 60° of rotational angles between two molecular rows.* ***b,*** *The AFM image reveals Fe-coordinated PTO chains. Fe atoms are separated by 9 Å along the chain, and about 8.6 Å across the chain. Scale bars in* ***a*** *and* ***b*** *are 5 Å.* ***c,*** *DFT calculations confirm the energetically favorable rotated arrangement of PTO self-assembly, which is in relative agreement with the experimental observation.* ***d,*** *DFT calculations show that Fe-coordination is preferred over Ag-coordination.*

## 5.2 Magnetic Signatures of Fe Atoms in Organometallic Chains

Figure 5.3b shows serial tunneling spectra performed along the central axis of a segment of a chain (Fig. 5.3a). From both the spectra and its contour (Fig. 5.3b, c), a dip around $E_F$ and symmetric steps at about $\pm18$ meV are consistently observed. These two features are considered as spin state excitations with different mechanisms induced by inelastic tunneling. The consistent observation of magnetic signatures along the PTO-Fe chain indicates the formation of a dispersed spin chain.

As discussed in Section 2.2.2, magnetocrystalline anisotropy (MA) is induced by
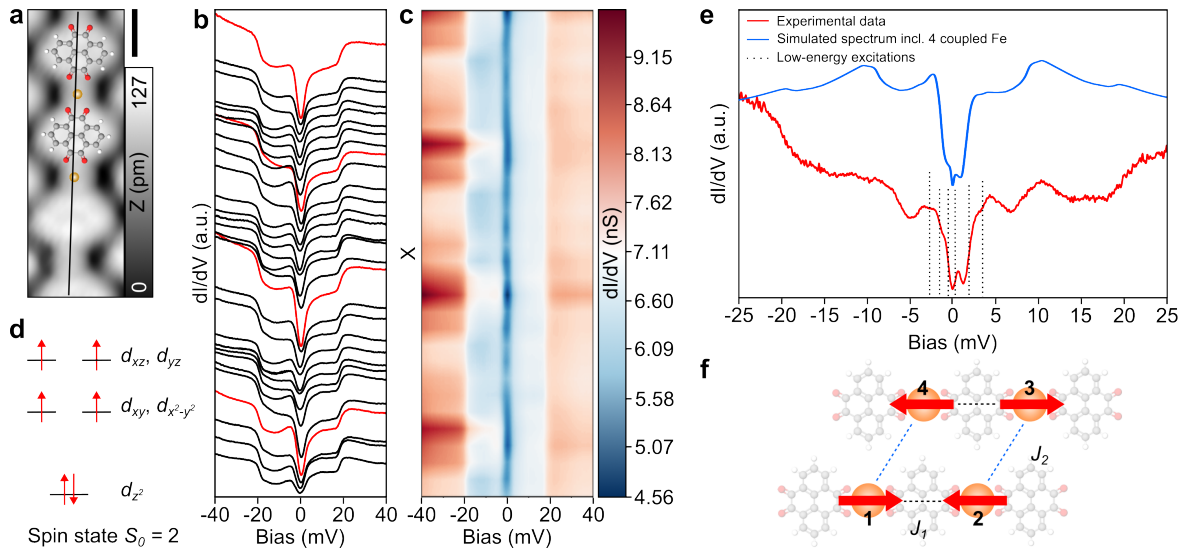
**Figure 5.3:** *Spectral analysis of a fully conjugated PTO-Fe chain on Ag(111).* ***a,*** *The STM image of a segment of PTO-Fe chain ($I_t$= 100 pA, $V$= 50 mV). The molecular model is superimposed on the image. Scale bar: 500 pm.* ***b,*** *A series of dI/dV spectra recorded along the PTO-Fe chain as marked in **a**. Spectra measured around Fe sites are plotted in red ($I_t$= 300 pA, $V$= 35 mV, $A_{mod}$= 1 mV).* ***c,*** *The dI/dV contour plotted based on **b** shows the modulated asymmetric lineshape with respect to the position.* ***d,*** *The DFT calculation of spin ground state on Fe, showing $S_0$= 2 and $D_{4h}$ symmetry of 3d energy levels after coordinating with PTO.* ***e,*** *The experimental dI/dV spectrum on Fe with a higher spectral resolution (red curve), and the conceptual simulated curve including four antiferromagnetically coupling Fe (blue) ($I_t$= 1.5 nA, $V$= 35 mV, Z-offset= +20 pm).* ***f,*** *The scheme of an unit spin lattice for simulating the spectrum in **e**.*

the combine effect of the crystal field and spin-orbit coupling, which can split the spin state into multiplets even without an external field. Excitations among these multiplets give rise to several steps at low energies on a dI/dV spectrum. Considering the adsorption on the Ag(111) hollow site and the coordination with two neighboring PTO (Fig. 5.2d), each Fe is in a square antiprismatic crystal field that lifts the $d$-level degeneracy (Fig. 5.3d). The DFT calculation also suggests the spin ground state $S_0$= 2 is expected on Fe. Thus, we assign the dip around $E_F$ as the spin-flip excitation of a single Fe resulted from MA, while the steps at ±18 meV mark the collective spin-flipping events caused by superexchange. In addition, the consistent lineshape observed along the PTO-Fe chain indicates that spin-flip excitations are delocalized across the entire chain. Rather than direct $d$-orbital overlapping, itinerant electron mediated Ruderman-Kittel-Kasuya-Yosida (RKKY) interaction [110–112] is the mechanism that leads to Fe-Fe coupling although being separated by a PTO molecule.

The tunneling spectrum with a higher energy resolution reveals more features inside the dip around $E_F$ and additional steps at about ±10 meV (red spectrum in Fig. 5.3e). Considering $S_0$= 2, a conceptual simulation of the spectrum was done

using the perturbative model developed by Ternes (blue curve in Fig. 5.3e) [176]. We construct the spin lattice with the unit cell including four antiferromagnetically coupled Fe along and across the chains (Fig. 5.3f). The simulated spectrum has the best agreement with the experiment when the uniaxial and transverse anisotropy strengths are $D=$ -1 meV and $E=$ 0.8 meV respectively on a single Fe. Parameters related to the substrate electron bath, such as potential scattering $U=$ 0.63 meV and Kondo scattering $J_K \rho_s =$ -0.02 meV are also taken into account.

Interestingly, these small energy excitations are usually observable with a decoupling layer [96, 105, 177], an atom or molecule decorated spin-polarized tip [178–181], or a superconducting substrate [182, 183]. In our system, a possible explanation could be that Fe atoms are lifted from the substrate due to the coordination with PTO molecules, and the exchange with substrate electron bath is slightly reduced. This could lead to the preservation of Fe spin ground state ($S_0=$ 2) as expected for a free-atom spin [105].

On the other hand, excitations at larger energies ($\pm 10$ meV and $\pm 18$ meV on the red spectrum in Fig. 5.3e) are associated with collective spin-flipping events. With Fe-Fe separation about 8 to 9 Å (Fig. 5.2b), RKKY interaction can be approximated by an antiferromagnetic Heisenberg Hamiltonian [184]. As plotted in Fig. 5.3f, we assume the same MA on each Fe, a constant and stronger intra-chain coupling strength ($J_1$), and a weaker inter-chain coupling ($J_2$). The Hamiltonian describing MA on a single magnetic impurity (Equ. 2.5) is modified accordingly as

$$\mathcal{H} = \sum_i^4 \mathcal{H}_i + J_1(\vec{S_1} \cdot \vec{S_2} + \vec{S_3} \cdot \vec{S_4}) + J_2(\vec{S_2} \cdot \vec{S_3} + \vec{S_1} \cdot \vec{S_4}), \qquad (5.1)$$

where $\mathcal{H}_i$ is the Hamiltonian of a single Fe. With $J_1=$ -4.0 meV and $J_2=$ -1.5 meV, steps at $\pm 10$ meV and $\pm 18$ meV in the experimental spectrum can be best reproduced.

Lastly, we adjust the tip-sample distance ($\Delta Z$) on top of a Fe site. The force imposed by the tip follows Lennard-Jones type potential that can pull or push Fe outward or toward the surface [139]. Such interaction is able to modify the exchange strength with the substrate and could possibly induce slight shift in the spin-flip energy [130, 139, 182, 183]. In Fig. 5.4, $\Delta Z = 0$ is defined by the tunneling condition $I_t=$ 1.5 nA, $V=$ 35 mV, and the tip position is changed manually without the feedback loop. At different $\Delta Z$, the lineshape of the spectra maintains, and only the excitation at about 5 meV shows clear shift (orange lines in Figs. 5.4a and 5.4b). Since the PTO-Fe coordination is rigid against the tip-induced structure modification, only the local Fe spin orbital responds to the force imposed by the tip and shows slight shift in the excitation energy. On the contrary, excitations at higher energies are related to the long-range Fe-Fe coupling which is delocalized along the chain (blue lines in Figs. 5.4a and 5.4b). The local change in the Fe bonding with the substrate has relatively minor influence, and thus and these energies remain unchanged under the tip effect.
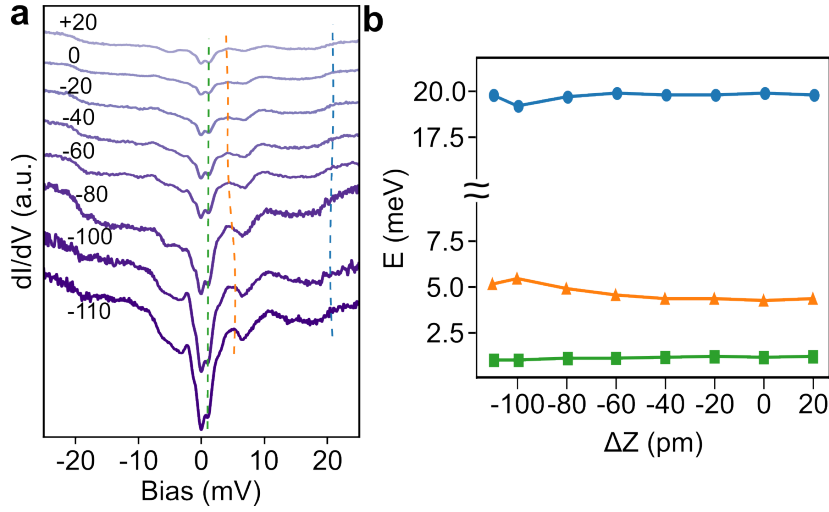
**Figure 5.4: *Height-dependent inelastic tunneling spectra measured on Fe.*** *a, Series of dI/dV spectra measured at different tip heights. Numbers marked next to the spectra indicate $\Delta Z$ with the unit of pm. $\Delta Z = 0$ is defined by $I_t = 1.5$ nA and $V = 35$ mV. Dash lines are plotted for the guide for the eye, showing the exemplary evolution of spin-flip energies at different tip-sample distances. b, Among the three exemplary spin-flip excitations, only the step at around 5 meV shifts slightly towards a smaller energy as the tip moves away from the surface, while the steps at about 1 meV and 18 meV stay almost unchanged ($A_{mod} = 400$ $\mu V$, $f_{mod} = 613$ Hz).*

## 5.3 Magnetic Properties of PTO-Fe Chains on the Superconducting Pb(111)

By transferring PTO-Fe coordinated chains from a normal metal to a superconductor, extended spin-flip excitation lifetime on Fe is expected due to the depletion of substrate DOS around $E_F$ [182, 183]. Figure 5.5b shows a series of d$I$/d$V$ spectra measured along the central axis of a PTO-Fe chain (Fig. 5.5a) using a superconducting Pb-tip at 1 K. Two pairs of excitations are systematically observed outside the superconducting gap around Fe sites (red spectra in Fig. 5.5b) that we assign as MA-induced spin-flip excitations. These excitation energies slightly vary on different Fe with the range up to 0.72 meV on eight exemplary spectra, which could the result of the modulating coupling strength with the substrate [65].

As more clearly resolved in the contour (Fig. 5.5c), asymmetric coherence peaks at Fe sites indicate the weak coupling with the superconducting states. The emergence of Yu-Shiba-Rusinov (YSR) bound states depend on the wavefunction overlap between unpaired electrons in $d$-orbitals of Fe and the substrate, in which the out-of-plane $d$-orbitals ($d_{xz}$, $d_{yz}$, and $d_{z^2}$) have larger effect than the in-plane orbitals ($d_{xy}$ and $d_{x^2-y^2}$) [130, 185]. By adopting the DFT calculation about $d$-orbital splitting and filling on Ag(111) as a similar coordination geometry of Fe is expected on both substrates, only the degenerate $d_{xz}$-/$d_{yz}$-orbitals and $d_{xy}$-/$d_{x^2-y^2}$-orbitals have unpaired electrons (Fig. 5.3e). As we interpreted in the previous section, Fe atoms are very

66

**Figure 5.5:** *Spectral analysis of a fully conjugated PTO-Fe chain on the superconducting Pb(111). **a,** The STM image of an assembly of PTO-Fe chains ($I_t$ = 80 pA, V = 9 mV). The molecular model is superimposed on the image. **b,** A series of dI/dV spectra recorded along the central axis of the PTO-Fe chain as marked in **a**. Spectra measured at Fe sites are plotted in red ($I_t$ = 300 pA, V = 8 mV, $A_{mod}$ = 50 μV). **c,** The dI/dV contour plotted based on **b** shows the modulated asymmetric coherence peaks and mildly dispersed spin-flip excitation with respect to the position. **d,** A defect site of the PTO-Fe chain with an additional Fe atom (green dot) attached to the chain ($I_t$ = 90 pA, V = 9 mV). **e,** dI/dV spectra measured at three Fe around the "defect" site of the chain. The green spectrum measured on an additional Fe shows typical YSR states without spin-flip excitation. The orange spectrum taken at the close vicinity to the additional Fe shows the coexistence of YSR states and the spin-flip excitation. The blue spectrum shows two pairs of spin-flip excitation, similar to those measured in the defect-free PTO-Fe chain. Black arrows mark spin-flip excitations and red arrows point out YSR in-gap states ($I_t$ = 300 pA, V = 8 mV, $A_{mod}$ = 50 μV).*

likely lifted by ketone groups of PTO, making the planar $d_{xy}$- and $d_{x^2-y^2}$-orbitals trivial and perpendicular $d_{xz}$- and $d_{yz}$-orbitals only weakly coupled to the substrate. This is possibly the reason pronounced in-gap quasiparticle excitations are not shown on the fully coordinated PTO-Fe chain.

Nevertheless, clear YSR in-gap states are observed at defect sites of the chain (Fig. 5.5e). For instance, due to the attachment of an additional Fe (green dot in Fig.5.5d), the coupling with the Fe inside the chain leads to the change in the spin ground state, and thus only one spin-flip excitation is found with the coexistence of

YSR states (see arrows in Fig. 5.5e). Although the end of the chain is deviated from the assembly (blue dot in Fig. 5.5d), the coordination with two PTO molecules enables a typical two-pair-spin-flip excitation as shown in the blue spectrum in Fig. 5.5e.

In addition, in Fig. 5.5b, spin-flip excitations are localized on Fe but absent on PTO, making a stark contrast with the measurement on Ag(111). This deviation is due to the different surface band characteristics of the two substrates, which gives rise to distinct RKKY interactions. The bulk Ag(111) exhibits Shockley surface state at about -65 meV with a parabolic dispersion close to $\Gamma$-point [186, 187], while bulk Pb(111) has a flat valance surface band dispersion around $M$ - and $K$-point at - 2.2 eV [188]. Furthermore, since the tunneling measurement is limited to the small energy window determined by the workfunction, the interaction between magnetic impurities and surface electrons away from $\Gamma$-point is difficult to be detected [187]. Thus, the low-lying surface states of Ag(111) are prone to interact with magnetic impurities of PTO-Fe chains, making it an ideal platform for the long-range RKKY interaction as observed by scanning tunneling spectroscopy (STS). On the contrary, the absence of such states on Pb(111) decreases long-range magnetic interaction and suppresses the signature of collective spin excitations in the tunneling spectra on Pb.

As a preliminary comparison, we first extract spin-flip excitation energies on Ag(111) from Fig. 5.3e, and shift these values by $2\Delta = 2.7$ meV due to the superconducting electrodes. The rough estimation of spin-flip energies on Pb(111) is obtained accordingly (dotted lines in Fig. 5.6b and Table 5.1). Note that the energy +3.00 and -3.20 meV fall close to the superconducting gap edge, which is an indication of another pair of spin-flip excitations as the superconducting gap on Fe is slightly wider than that on the bare Pb(111). However, this rough estimation does not match exactly with the experimental results on Pb(111). A possible reason for the deviation could be the strong coupling of Fe to Pb(111) that modifies the crystal field.

Based on the spectrum in Fig. 5.6b, differential conductance maps (Figs. 5.6c and 5.6d) measured at coherence peak energies ($\pm 2\Delta$ meV) show different relative intensity between PTO and Fe at the particle- and hole-regimes. This difference stems from the magnetic nature of Fe, where highly asymmetric coherence peaks arise. On the other

**Table 5.1:** *Estimated and experimental spin-flip excitation energies of Fe on Pb(111).*

| Excitation on Ag(111) (meV) | Estimation on Pb(111) (meV) | Excitation on Pb(111) (meV) |
|:---:|:---:|:---:|
| +0.30 | +3.00 | - |
| +1.90 | +4.60 | +4.34 ($+\varepsilon_1$) |
| +3.30 | +6.00 | +4.96 ($+\varepsilon_2$) |
| -0.50 | -3.20 | - |
| -1.65 | -4.35 | -4.22 ($-\varepsilon_1$) |
| -2.85 | -5.55 | -4.84 ($-\varepsilon_2$) |

hand, magnetic characteristics cease on PTO and equal intensity of coherence peaks are observed. Conductance maps at each pair of spin-flip energies ($\pm\varepsilon_1$ and $\pm\varepsilon_2$) have roughly the identical DOS distribution on Fe (Figs. 5.6e-h).

As demonstrated in the previous works [182, 183], the lifetime of the spin state excitation can be extracted from d$I$/d$V$ spectra measured at different tip-sample distances. The spin state excitation peaks are expected to shift towards larger energies as
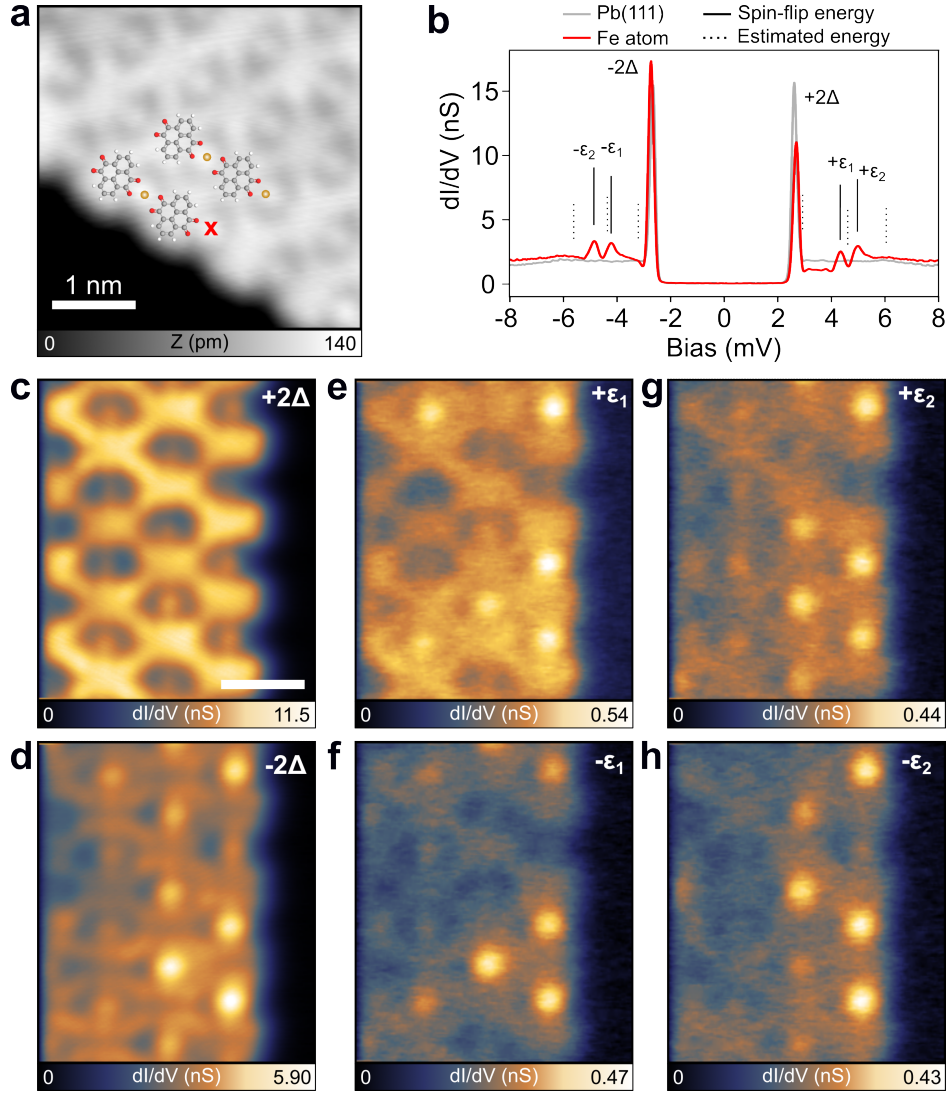


**Figure 5.6: *Conductance maps measured at the characteristic energies.*** *a, The STM image of an assembly of PTO-Fe chains ($I_t$ = 90 pA, V = 9 mV). The molecular model is superimposed on the image. b, Representative dI/dV spectra measured on Pb and on a Fe marked by the red cross in a ($I_t$ = 300 pA, V = 8 mV, $A_{mod}$ = 50 µV). c-h, dI/dV maps recorded at pairing and spin-flip energies. Maps e-h show roughly identical DOS distribution on Fe at each pair of spin-flip excitation ($\pm\varepsilon_1$ and $\pm\varepsilon_2$ respectively). Scale bar: 1 nm.*

the tip approaches. This measurement is planned to perform on the PTO-Fe/Pb(111) system in the near future.

## 5.4  Summary

In this chapter, we compare spin-flip excitations of an ordered magnetic lattice on a normal metal and on a superconductor. We fabricate an OM framework using PTO and Fe on Ag(111) and Pb(111). On Ag(111), the slight lifting of Fe after the coordination with PTO decouples the magnetic moment from the substrate, leading to the visibility of spin-flip excitations at small energies induced by MA. PTO-Fe chains on superconducting Pb(111) show only two clear spin state excitations and asymmetric coherence peaks that indicate weak spin-superconductivity coupling. Interestingly, the Fe-Fe coupling due to RKKY interaction is only observable on Ag(111) and absent on Pb(111). This different coupling behavior can be attributed to different electronic properties of the two substrates.

# 6

# Topological Superconductivity in a Molecule-Based Electron Spin Lattice

W ITH the protection from topology, Majorana zero modes (MZMs) are known to be tolerant to defects or external disturbance, and are expected to be fabricated into a novel type of qubits for quantum computing. So far, the realization of MZMs in 2D has only been found by coupling transition metal magnetic islands with $s$-wave superconductivity (see Section 2.4.2) [150–152, 189, 190]. As demonstrated in Chapter 5, the PTO-Fe spin lattice fabricated on the superconducting Pb(111) shows spin-flip excitations without sub-gap quasiparticle excitations, indicating insufficient interaction between magnetic moments and superconducting states. In search of a novel approach, as described in Section 2.1.2, molecule electron acceptors are able to extract one electron from the substrate and ensure the simple spin-1/2 system. With designed ligands, the backbone of a molecule can be lifted, leading to the natural decoupling effect. Inspired by the recent works about tip-induced charge-state control using scanning tunneling microscopy (STM), [28, 30, 93], we propose to fabricate a Shiba lattice with such gate-tunable radical molecules on a superconductor.

In this chapter, the Shiba lattice is realized by 4,5,9,10-tetrabromo-1,3,6,8-tetraazapy-rene (TBTAP) molecules which self-assemble into large-range islands on the superconducting Pb(111). TBTAP molecules are able to trap one electron from Pb(111), and form alternating charged and neutral rows in the assembly. Through the investigation of STS at millikelvin and 1 K, we demonstrate the sub-gap quasiparticle excitations on charged TBTAP molecules, as well as the modulation of Yu-Shiba-Rusinov (YSR) band across the molecular island. Supported by theoretical calculations, we assign the emergence of low-energy modes (LEMs) to chiral MZMs near the edge of the supramolecular assembly.

## 6.1 Supramolecular Assembly of TBTAP on the Superconducting Pb(111)
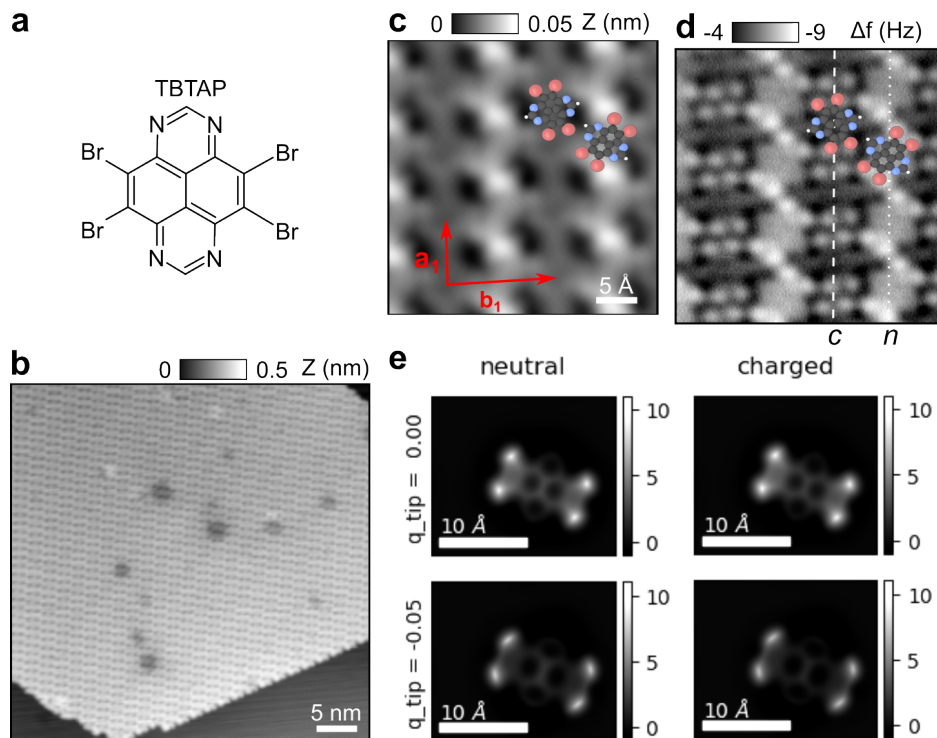


**Figure 6.1:** *Supramolecular assembly of radical TBTAP molecules on Pb(111).* ***a,*** *The chemical structure of 4,5,9,10-tetrabromo-1,3,6,8-tetraazapyrene (TBTAP).* ***b,*** *The STM overview of the supramolecular assembly on Pb(111) ($V = -0.5$ V, $I_t = 1$ pA).* ***c,*** *The close-up STM image of the molecular lattice ($V = 0.8$ V, $I_t = 0.8$ pA). The unit cell is marked with arrows.* ***d,*** *The corresponding constant-height AFM image acquired with a Br-fuctionalized tip. The lattice consists of charged (c) and neutral (n) TBTAP molecule rows. Red, blue, white and black colors of the CPK models refers to Br, N, H and C atoms.* ***e,*** *Simulated AFM images using the probe-particle model [191]. DFT coordinates are applied for an isolated neutral and charged molecule on the surface with a neutral (top row) and a charged (bottom row) tip.*

As precursors, we synthesize 4,5,9,10-tetrabromo-1,3,6,8-tetraazapyrene (TBTAP) molecules (Fig. 6.1a) that is composed of an acceptor perimidine backbone and four peripheral Br atoms. In a recent work [30], we have shown that the TBTAP molecule is singly-occupied by an electron donated from the substrate, leading to the spin-1/2 ground state on Ag(111). We thus sublime TBTAP molecules in ultra high vacuum on the Pb(111) substrate kept at about 200 K (see Section 3.4.2), forming large supramolecular domains larger than 100 nm (Fig. 6.1b). Molecules exhibit a densely packed rectangular structure (lattice parameter $a_1 = 12.3$ Å and $b_1 = 17.2$ Å, arrows in Fig. 6.1c), observed by STM as alternating dark and bright rows. The corresponding
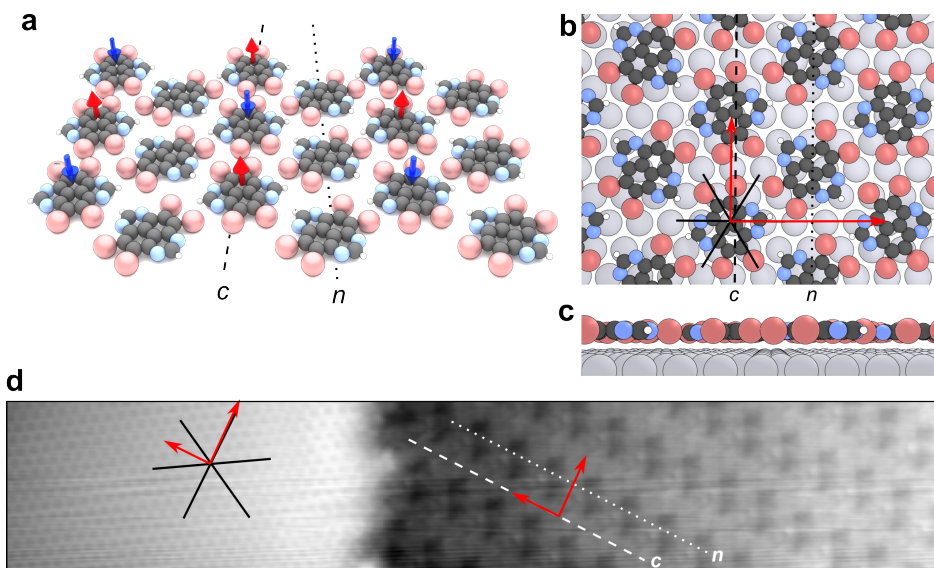
## 6.1. Supramolecular Assembly of TBTAP on the Superconducting Pb(111)



**Figure 6.2:** *TBTAP supramolecular assembly on Pb(111) optimized by DFT. **a,** The perspective view of the TBTAP assembly on Pb(111) optimized by DFT calculations. Red and blue arrows depict the electron spin lattice formed by the anionic TBTAP$^{•-}$ molecules. **b,** Simulated top and side (**c,**) views of the TBTAP supramolecular assembly on Pb(111). The unit cell is 17.5 Å×12.1 Å, 90°. **d,** STM image of both the supramolecular assembly and the Pb(111) substrate with atomic resolution. Red arrows refer to the molecular lattice, black lines are the principal directions of Pb(111), and white dashed/dotted lines mark molecular rows.*

constant-height atomic force microscopy (AFM) image (Fig. 6.1d), probed by a Br-terminated tip, shows each Br atom bound to the TAP backbone as bright protrusion that allows assigning the exact position of the molecule in the array (space-filling CPK models in Fig. 6.1d). Similar to STM imaging, two AFM contrasts are observed as a function of the rows under consideration denoted as $c$ (dashed line) and $n$ (dotted line). To rationalize this contrast difference, we simulated the AFM image of the neutral and anionic TBTAP (denoted as TBTAP$^0$ and TBTAP$^{•-}$ respectively) from the density function theory (DFT) coordinates using the probe-particle model (Fig. 6.1e) [191]. Using an uncharged tip (top row, no electrostatic molecule-tip) interaction, TBTAP$^0$ and TBTAP$^{•-}$ have the same contrast. For a negatively charged tip (bottom row), the neutral molecule appears bright, especially in the central region. This implies that the contrast difference emerges due to different electrostatics between the sample and the tip, instead of the topographic cause.

Using DFT, we relaxed the supramolecular TBTAP network on Pb(111) (Figs. 6.2a-c). The lattice parameter ($a_1$= 12.1 Å and $b_1$= 17.5 Å, rotated by 90°) is in registry with the Pb(111) surface and agrees with the experimental data. Molecules are stabilized by a combination of halogen bonds between Br atoms (C–Br...Br–C) and TAP units (C–N...Br–C). The $n$ rows have their molecules inclined by 50° with respect to the row axis, while molecules in $c$ rows are almost vertically overlapped (-

6°). Furthermore, according to DFT calculations, molecules are flat-lying in the same plane 3.4 Å above the surface (Fig. 6.2c). Therefore, we conclude that the contrast in STM/AFM images between molecules of neighboring rows is due to the coexistence of two charge-states in the TBTAP assembly [93], rather than the difference of relative height. Note that the selective charging of the TBTAP assembly is the result of electronic long-range self-interaction, which is unable to be modelled directly by DFT [192]. In addition, to compare the simulated morphology with the experimental data, we acquired a STM image resolving both the supramolecular assembly and the Pb surface with atomic resolution (Fig. 6.2d). The black lines show the main crystallographic directions of Pb(111) with red arrows the TBTAP lattice unit vector. By comparing Fig. 6.2b with Fig. 6.2d, we found the self-assemble registry is well-aligned between DFT simulation and STM investigation.

## 6.2 Imaging Correlated Electrons of the Supramolecular Assembly

To confirm the assumption of alternating $c$-$n$ rows according to the AFM simulation (Fig. 6.1e), we assigned their molecule charge states by comparing $dI/dV$ spectra (Fig. 6.3b) of TBTAP molecules located in $c$ and $n$ rows respectively. For $c$ molecules (also TBTAP$^{\bullet-}$, blue spectra), a strong resonance $D$ appears at $V \approx 1$ V which is absent for $n$ molecules (also TBTAP$^0$, red spectra). The $D$ resonance peak is attributed to a charge state transition induced by the local electric field of the tip, which transfer the molecule charge state from TBTAP$^{\bullet-}$ to its neutral counterpart TBTAP$^0$ [28, 30, 93]. Radical TBTAP$^{\bullet-}$ are obtained by transferring one electron from the surface to the lowest unoccupied molecular orbitals (LUMO). Due to Coulomb repulsion, the former LUMO splits into a singly-unoccupied molecular orbital (SUMO) above $E_F$ and a singly-occupied molecular orbital (SOMO) below $E_F$ with different spin directions. As shown in Fig. 6.3c, SOMO and SUMO energy levels are located at $\pm150$ meV respectively. Similar mechanism of forming radical molecules by electron donation from the substrate have also been reported in the literature [193]. Note that charging events expected at negative voltages are not observed for either type of molecules, meaning that trapping an excessive charge on the molecule is spontaneous instead of tip-induced.

The discharging efficiency from TBTAP$^{\bullet-}$ to TBTAP$^0$ is characterized by the *lever arm* ($\alpha$), which is linearly dependent on the applied voltage $V$ and the tip position ($X$, $Y$, $Z$) with respect to the charged molecules. The discharge of TBTAP$^{\bullet-}$ on Pb(111) can be explained by the double-junction tunneling barrier (DJTB) model [28, 93, 194]. By gradually increasing the positive sample voltage $V$, the energy level of SOMO is only shifted by $\alpha V$ with respect to the chemical potential of the substrate due to the potential barrier between the molecule and the substrate. As depicted in Figs. 6.3e and d, when $V = V_{thresh}$ ($V_{thresh}$ is the threshold voltage of the molecule discharge), SOMO aligns with the surface chemical potential, the electron at SOMO
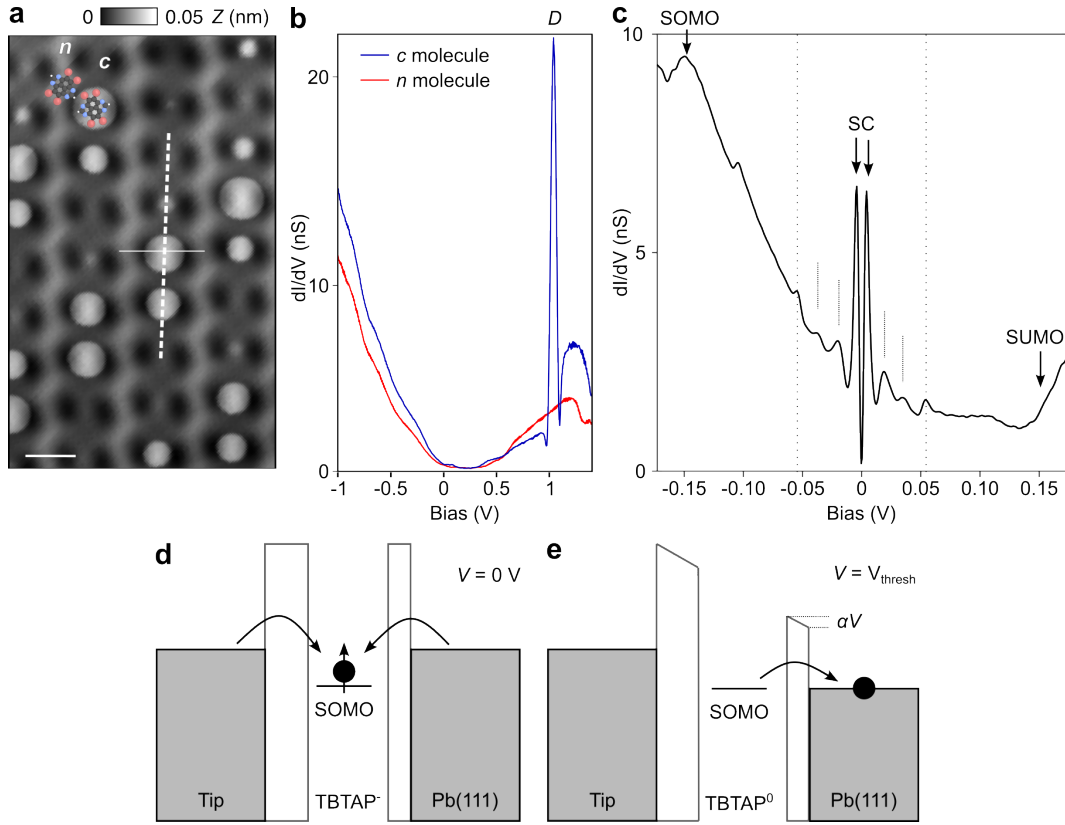
**Figure 6.3:** **$TBTAP^{\bullet-}$ discharging mechanism.** **a,** *The STM image of the molecular assembly (V = 0.8 V, $I_t$ = 50 pA). The scale bar is 1 nm.* **b,** *Single-point dI/dV spectra of c (blue) and n (red) molecules. The D resonance peak correspond to the tip-induced discharging event (V = -0.8 V, $I_t$ = 100 pA, $A_{mod}$ = 20 mV).* **c,** *dI/dV spectra on a charged molecule. Dotted lines refers to vibrational excitations of the TBTAP molecule at ± 18 meV, ± 36 meV and ± 52 meV respectively, which are similar to our previous work of TBTAP/Ag(111) [30]. Black arrows point to the SOMO/SUMO onsets at ± 150 meV. SC refers to the superconducting gap edge which resolution is hampered by the large voltage modulation used for the lock-in detection (lock-in parameters: $f_{mod}$ = 611 Hz, $A_{mod}$ = 700 µeV).* **d,** *Energy levels of the tip-TBTAP-surface for V = 0 V. SOMO of the molecule below $E_F$ is occupied by an electron.* **e,** *By applying a positive voltage V ≥ $V_{thresh}$, SOMO is shifted by the amount αV with respect to the chemical potential of the substrate. When SOMO crosses $E_F$, the level is emptied, leading to the discharge and the neutral state of TBTAP.*

is able to tunnel through, and the molecule is now in the $TBTAP^0$ state. Such charge-state transition opens an additional tunneling channel between tip and sample, being observed as a sharp conductance peak $D$ in d$I$/d$V$ spectra (Fig. 6.3b). To determine $\alpha$, we estimate the ratio between the SOMO level ($E_{SOMO}$) and the energy of discharging ($E^{-\to 0}$ = e$V_{thresh}$), which gives $\alpha = |E_{SOMO}|/(E^{-\to 0} - |E_{SOMO}|)$ [155]. From Fig. 6.3c, $E_{SOMO}$ is about -150 meV, and $E^{-\to 0}$ = 0.9 eV according to Fig. 6.3b. Therefore, $\alpha$ = 0.2, which is in the similar range compared to previous works regarding discharge of

molecules on metals [28] or on a thin insulating layer [195].

A constant-height $dI/dV$ map acquired at the discharge threshold $D$ shows that rings and dots of high conductance always center on molecules in $c$ rows, marking the signature of discharging events (Fig. 6.4a). It also indicates the spatial position of electrons trapped at TBTAP$^{\bullet-}$ prior to its discharge (i.e. without tip gating). When the tip is located inside a ring in $dI/dV$ maps, the molecule is discharged but remains charged when the tip is outside the ring. Discharging rings were not observed for molecules of $n$ rows since no charge can be extracted from the TBTAP$^0$. Figure 6.4b shows a $dI/dV$ cross-section acquired across $n$-$c$-$n$ rows (solid line in Fig. 6.4a). The high-conductance parabola is positioned above the TBTAP$^{\bullet-}$ molecule with its bottom ($\approx 0.9$ V) corresponding to the minimum voltage for the discharge. Owing to the linear dependency of $\alpha$, the parabolic branches linearly expands with increasing $V$, which also reflects the formation of "Coulomb" rings at higher voltages in the corresponding $dI/dV$ maps.

Circular halos in Fig. 6.4a form a well-ordered superlattice of parameter $a_2 = 20$ Å and $b_2 = 39.7$ Å and rotated by $30°$ with respect to the molecular lattice. The variation of ring diameters is due to a slight modulation of the threshold voltage $\Delta D$ along the charged rows. We found $\Delta D \approx 150$ mV by comparing the bottom of parabolas among neighboring TBTAP$^{\bullet-}$ of a $c$ row (Fig. 6.4c). When $V \geq 1.1$ V and the tip is located
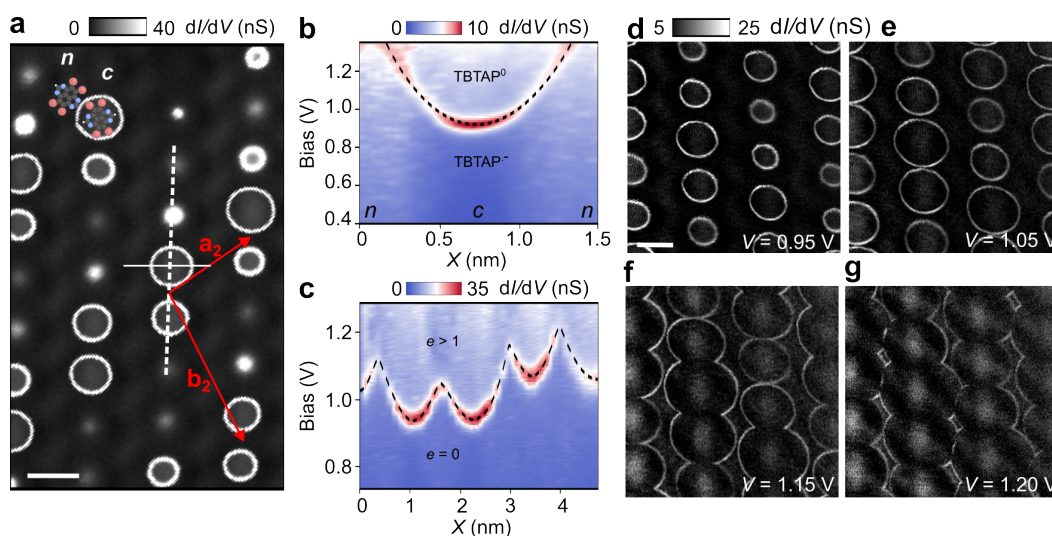


**Figure 6.4:** *Electron superlattice of the supramolecular assembly. a, The dI/dV map shows discharging rings centered at every molecules of c rows. Red arrows mark the electron superlattice unit vector (V = 1 V, $A_{mod}$ = 6 mV). b, The dI/dV contour across n-c-n rows (solid line in a) that shows electron localization c, The dI/dV contour across five TBTAP$^{\bullet-}$ molecules (dashed line in a). The parabolic pattern marked by the dashed line corresponds to multiple discharging events by tip gating. e is the number of charge removed by gating. d-g, Series of dI/dV mapping at increasing V shows the expansion of the ring diameter and cascade discharge for V $\geq$ 1.15 V ($A_{mod}$ = 6 mV). Scale bars are 1 nm.*

between two adjacent molecules, the parabola start to merge (dashed line in Fig. 6.4c) promoting the removal of multiple electrons from neighboring molecules (region $e > 1$). Increasing $V$ in a series of d$I$/d$V$ maps (Figs. 6.4d-g) first leads to the ring expansion in real space (Fig. 6.4e), and their coalescence along $c$ rows (Fig. 6.4f). In contrast to a simple superposition of rings as expected for non-interacting quantum dots, their fusion as observed in Figs.6.4f-g indicates a cascade discharge along $c$ rows and thus a manifestation of electron correlation in the supramolecular assembly [196].

# 6.3 Spectral Characterization of the Supramolecular Assembly

## 6.3.1 Yu-Shiba-Rusinov states from radical molecules

Radical TBTAP$^{\bullet -}$ on Pb(111) feature a $S = 1/2$ ground state with strong spin-polarization according to DFT calculations (Fig. 6.5a). To assign the interaction of the electron spin lattice with the superconducting Pb, we probed the YSR bound states of TBTAP$^{\bullet -}$ in the middle of the island using tunneling spectroscopy with a metallic tip at 35 mK (see Section 3.3). In Fig. 6.5c, we compared d$I$/d$V$ spectra of three neighboring TBTAP$^{\bullet -}$ (black) with the pristine Pb(111) surface (blue) and a TBTAP$^0$ (red). In all the spectra, a hard gap is systematically observed centered to $E_F$ and framed by the coherence peaks of Pb(111) [44]. Similar to Pb, TBTAP$^0$ shows no in-gap states due to the absence of unpaired electrons. Each TBTAP$^{\bullet -}$ spectrum additionally shows one pair of YSR states at energies $\varepsilon_\alpha = \pm 460$ $\mu$eV, $\varepsilon_\beta = \pm 720$ $\mu$eV and $\varepsilon_\gamma = \pm 940$ $\mu$eV (dotted lines), resulting from the spin-1/2 nature of the radical molecule.

In series of d$I$/d$V$ maps at $\varepsilon_\alpha^\pm$, $\varepsilon_\beta^\pm$, and $\varepsilon_\gamma^\pm$ YSR energies (Figs. 6.5e, f), both particle-like and hole-like wavefunctions of TBTAP$^{\bullet -}$ show the typical donut-shape, which is similar to the computed spin density map of the anionic molecule (Fig. 6.5a). These differential conductance maps also show that YSR energies are molecule-dependent and well-extended in real space into a long-range superlattice. We thus attribute the convergence to only three YSR energies and their spatial distribution to the long-range coherent coupling between quasiparticle excitations in the spin network [138].

Figure 6.5g shows a d$I$/d$V$ cross-section across the island (red arrow of Fig. 6.5d), where white dotted lines refer to the $\varepsilon_{\alpha,\beta,\gamma}^\pm$ YSR energies. Broad resonances near $E_F$ coexist with the YSR peaks as marked by black arrows in Figs. 6.5c and g. These LEMs are systematically observed with the highest intensity on molecules along the white dashed lines marked in the zero-energy d$I$/d$V$ map as in Fig. 6.5d.

## 6.3.2 Spectral signatures of low-energy modes

The intrinsic particle-hole symmetry of zero-energy modes, imposed by the Bogoliubov quasiparticle character, can be probed by tunneling spectroscopy using superconduct-
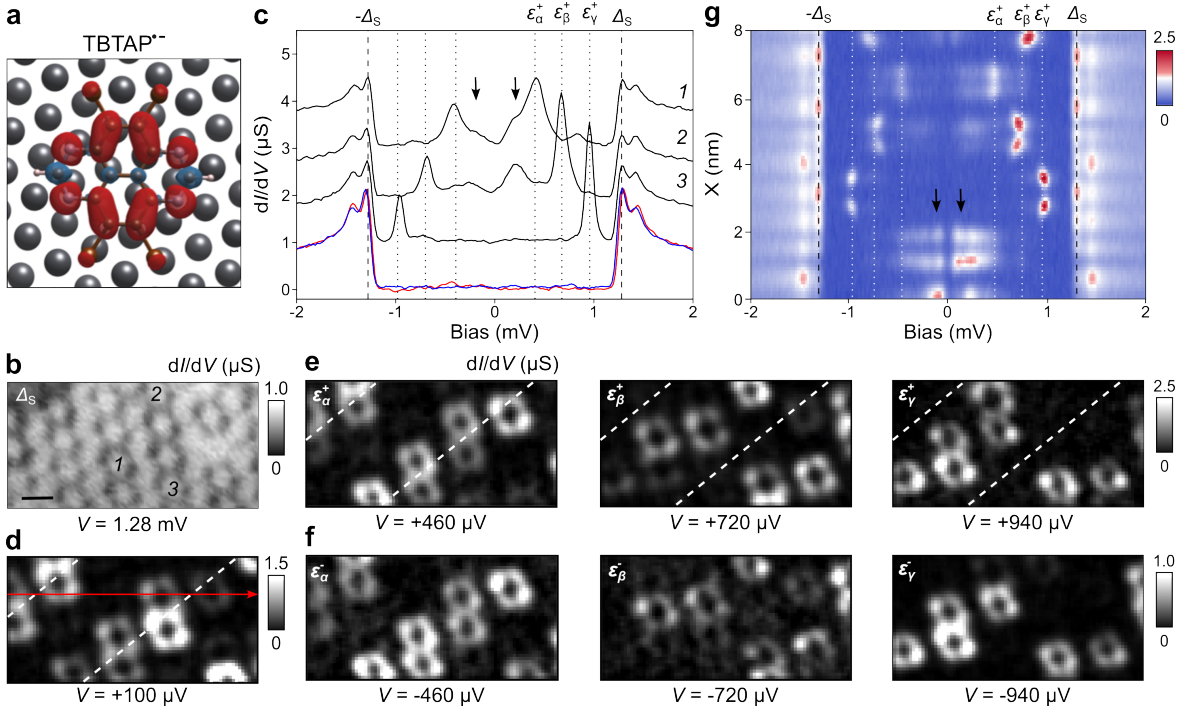
**Figure 6.5: _YSR states of the TBATP$^{\bullet-}$ assembly._ a,** _Spin density map of a single TBTAP$^{\bullet-}$ molecule on Pb(111) calculated by DFT._ **b,** _dI/dV (X, Y) map of the TBTAP$^{\bullet-}$ assembly acquired at energy $\Delta_S$= -1.28 meV at T= 35 mK with a metallic tip. The scale bar is 1 nm (lock-in parameters: $f_{mod}$= 3.28 kHz, $A_{mod}$= 40 µV, tunneling parameters: $I_t$= 200 pA, V = 5 mV)._ **c,** _Exemplary dI/dV point-spectra of Pb(111) (red), TBTAP$^0$ (blue), and three representative TBTAP$^{\bullet-}$ (black). Black spectra are shifted by 1 µS for clarity. Pairs of YSR resonances at $\varepsilon_\alpha = \pm$ 460 µeV, $\varepsilon_\beta = \pm720$ µeV and $\varepsilon_\gamma = \pm940$ µeV are molecule-dependent along the c row. The black arrows mark the low-energy modes near $E_F$._ **d,** _The near zero-energy ($\varepsilon$= +100 µeV) dI/dV map shows the spatial distribution of the LEM line as pointed out by the white dotted line._ **e-f,** _Series of dI/dV maps extracted at energies of $\pm\varepsilon_\alpha$, $\pm\varepsilon_\beta$ and $\pm\varepsilon_\gamma$ respectively._ **g,** _dI/dV (V, X) cross-section acquired along the red arrow in **d**. White dotted lines refer to YSR energies. Dashed lines show the superconducting edge $\pm\Delta_S$, while black arrows mark LEMs._

ing STM tips ($\Delta_T$= 1.35 meV is the superconducting pairing strength of the tip). Due to the convolution of tip and sample electron DOS, a zero-energy peak appears in d$I$/d$V$ spectra as a pair of peaks of equal amplitude shifted from zero to the finite voltages $eV = \pm\Delta_T$, while the superconducting edge is observed at $\pm (\Delta_T + \Delta_S) = \pm$ 2.7 meV ($\Delta_S$= 1.35 meV is the superconducting pairing strength of the substrate). Using bulk Pb tips at T= 1 K, YSR energies at $\varepsilon_{\alpha,\beta,\gamma}$ acquired from millikelvin measurements (Fig. 6.5c) are now expected to be found at a single energy $eV= \pm(\Delta_T + \varepsilon_{\alpha,\beta,\gamma}) \approx \pm2.1$ meV due to the large thermal broadening ($\approx$ 90-100 µeV). This is in agreement with our results measured along seven TBTAP$^{\bullet-}$ (white dotted lines in Fig. 6.6a and $\varepsilon^\pm_{\alpha,\beta,\gamma}$ marked in Fig. 6.6b). In addition, the emergence of YSR states
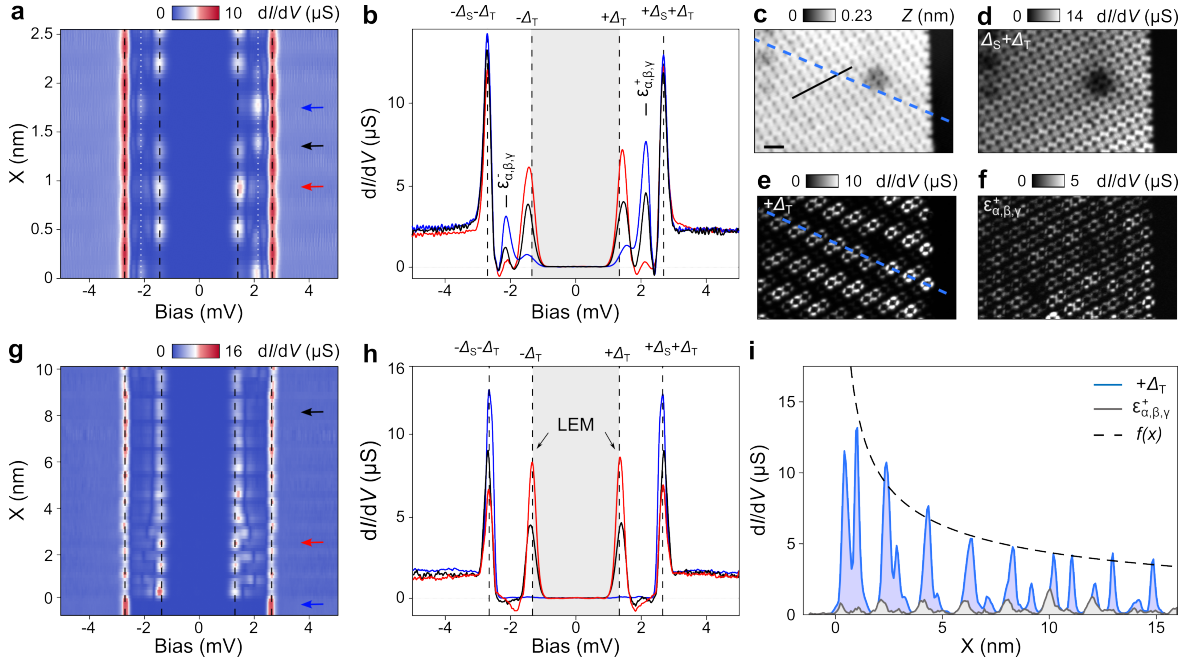
**Figure 6.6:** *Tunneling spectroscopy of LEMs near an island edge.* **a,** $dI/dV$ *cross-section measured along seven TBTAP$^{\bullet-}$ (black line in **c**). White dotted lines mark the YSR energies $\varepsilon_{\alpha,\beta,\gamma}^{\pm}$, and black dashed lines correspond to $\pm(\Delta_T + \Delta_S)$ and $\pm\Delta_T$ energies respectively (lock-in parameters: $f_{mod}= 611$ Hz, $A_{mod}= 25$ μV, tunneling parameters: $I_t= 300$ pA, $V= 5$ mV).* **b,** $dI/dV$ *spectra extracted at the red, blue, and black arrows in **a**.* **c,** *The topography and **d-f,** $dI/dV$ maps near an island edge showing DOS at the superconducting gap energy, wavefunction of LEMs, and at the $\varepsilon_{\alpha,\beta,\gamma}^{+}$ energy. Scale bar is 1 nm.* **g,** $dI/dV$ *cross-section acquired along the blue dashed line in **c**, which is also the local maxima of the modulated LEM wavefunction.* **h,** $dI/dV$ *spectra extracted at the blue, red, and black arrows in **g**. LEMs appear as pairs of peaks with equal amplitude positioned at $\pm\Delta_T$.* **i,** *Decay length of the LEM wavefunction (blue) comparing to the $\varepsilon_{\alpha,\beta,\gamma}^{+}$ energy (grey) along the blue dashed line in **e**. The border of the island is set at $X= 0$ nm. The dashed line is the theoretical fit of the edge mode using two exponential functions that estimate the short ($\xi_1= 3$ nm) and the long ($\xi_2= 110$ nm) localization length.*

is accompanied by resonances at $\pm\Delta_T$, which are signatures of LEMs probed by a superconducting tip.

From the constant-height $dI/dV$ maps acquired near the island edge, we compare the spatial distribution of LEM wavefunction at $+\Delta_T$ (Fig. 6.6e), hole-like (YSR) wave-function at $\varepsilon_{\alpha,\beta,\gamma}^{+}$ (Fig. 6.6f), and at the superconducting edge $\Delta_T+\Delta_S$ (Fig. 6.6d). At the YSR energy, DOS is homogeneous along $c$ rows, while LEM lines emerge along the rotational angle of 60° with respect to the edge. The propagation of the LEM lines corresponds to the ferromagnetic direction of the spin lattice. To better characterize LEMs, we next extracted a $dI/dV$ cross-section across the island edge along one LEM line (Fig. 6.6g acquired along the blue dashed line in Fig. 6.6e).

As shown in Fig. 6.6h, all in-gap excitations along the LEM line strictly appear at zero energy ($\pm\Delta_T$) with equal amplitudes of particle-like and hole-like regimes. This observation is in stark contrast with the particle-hole asymmetry of YSR resonance peaks (Fig. 6.6b), indicating the "near" zero-energy character of these edge modes.

### 6.3.3 Localization length of low-energy modes near the island edge

We next characterize the LEM localization length (Fig. 6.6i) by comparing $dI/dV(\text{X})$ profiles along the LEM line (blue) with the one obtained at $\varepsilon^+_{\alpha,\beta,\gamma}$ energy (grey). In contrast to the continuous spatial distribution of the $\varepsilon^+_{\alpha,\beta,\gamma}$ DOS, the LEM DOS has its maximum amplitude at the border of the island ($X = 0$) with a long decay towards the interior of the island without completely vanishing. To explain this observation, we consider the TBTAP$^{\bullet-}$ network as a spin-1/2 lattice with long-range YSR overlap coupled to a superconductor as in References [135,155]. We further estimate the LEM decay by fitting its envelop (dashed line in Fig. 6.6i) with $f(x)$, which is composed of two exponential functions with the short $\xi_1 = 3$ nm and the long $\xi_2 = 110$ nm localization length [21].

## 6.4  The Theoretical Modeling of Edge Modes

To further rationalize our findings, we use a tight binding model on a rectangular spin lattice introduced by Soldini *et al.* [153] in order to describe the symmetry-protected topological order of an antiferromagnet-superconductor hybrid system. As suggested by our tunneling spectroscopy measurements, we assume the antiferromagnetic order of the electron spin lattice imposed on the TBTAP assembly (Fig. 6.7a, electron spin orientation illustrated by red and blue arrows). Based on our STM observations (Fig. 6.1b and Fig. 6.6c), we construct a prototypical Shiba lattice mimicking the supramolecular network boundaries by only considering edges along the [110] direction (red dashed line in Fig. 6.7a). Figure 6.7b shows the simulated zero-energy LDOS map, where LEMs are found located at edges in agreement with [153]. Theoretical LDOS spectra are plotted in Figs. 6.7c and d for two selected edge positions marked in green and orange squares in Fig. 6.7b respectively. These edge modes exhibit two typical spectral signatures consisting of either two peaks with equal amplitude split from $E_F$ (green in Fig. 6.7c), or three resonances centered to $E_F$ (orange in Fig. 6.7d). Both of these cases are framed by a topological gap ($\pm\Delta_{top}$) extracted at the center of the island (faint yellow spectra in Figs. 6.7c, d), as well as the superconducting gap at $\pm\Delta_S$ (grey spectra). Since the 45°-edges selected in our model lattice are protected by spatial symmetries [153], these edge modes possess a topological character due to the formation of a gapped topological crystalline superconductor. The experimental spectral signatures of LEMs (Figs. 6.7e, f) acquired near an edge at 50 mK with a metallic tip are in good agreement with the theoretical prediction of these topological edge modes.
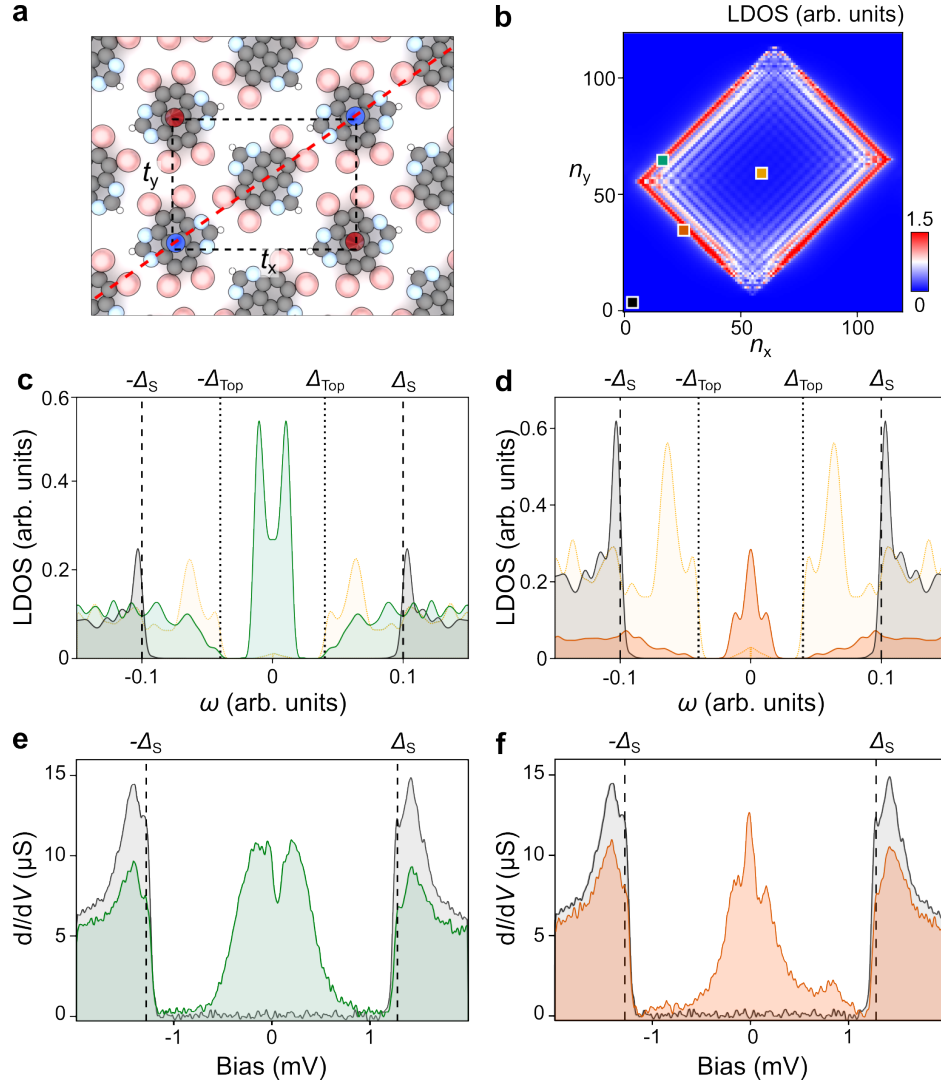
**Figure 6.7: *Theoretical modeling of LEMs. a,*** *Antiferromagnetic spin lattice (black dashed rectangle) formed by the supramolecular assembly (red arrow: spin up, blue arrow: spin down). The molecular lattice has different hopping strengths $t_x$ and $t_y$ in x and y directions. The red dashed line is the assumed 45°-edge with respect to the molecular lattice. **b,** LDOS map of the constructed lattice at zero energy shows the emergence of edge modes. **c-d,** Theoretical LDOS($\omega$) spectra of LEMs extracted at lattice edges (green and orange squares in **a**) as the comparison to the pristine Pb (grey) and the center of the island (faint yellow). **e-f,** Experimental dI/dV spectra of edge modes acquired at 50 mK with a metallic tip (lock-in: $f_{mod}$= 3.2 kHz, $A_{mod}$= 20 μV).*

# 6.5  Summary

In conclusion, we demonstrated the formation of highly-ordered arrays of electron spins on the superconducting Pb(111) through the supramolecular assembly of organic radicals. Occupied by a single electron transferred from the substrate, radical molecules are in the spin-1/2 ground state, confirmed by probing one pair of YSR in-gap states in differential conductance spectra. Additionally, signatures of LEMs are observed by tunneling spectroscopy near molecular island edges with a long decay length towards the interior of the domain. Using both metallic and superconducting tips, we investigate the zero-energy character of the LEM resonance: its intrinsic particle-hole symmetry, the localization length, as well as position-dependent spectral signatures. Altogether, these key features reproduced by theory are consistent with the emergence topological non-trivial modes in an antiferromagnet-superconductor hybrid system that can be assigned to Majorana zero modes [153].

Nevertheless, such symmetry-protected topological superconductor can have complex topological phase diagrams that depends on edge terminations of the system boundaries, as well as the lattice parameter $a$ (i.e. hopping parameters $t$) [153]. Moderate assembly disorders or alternative boundaries that break the mirror symmetry of the system could result in trivial edge modes.

Since the molecular spacing determines the spin lattice constant, we plan to explore in future works the design of side groups of the molecule, which enables the access to alternative sizes and lattice symmetries. For instance, one can envision to use coupled spins in nanographene structures [92] as 1D or 2D Shiba lattices obtained by on-surface reactions on a superconducting substrate [197]. More importantly, our findings demonstrate the reversible control of the charge (spin) in radical molecule by the local electric field of the tip, opening an interesting platform for the fine tuning of the system with external gate voltages. We envision to controllably build defect patterns in the molecular assembly by tip-induced chemistry [198] in order to investigate the effect of disorder on the topological phase as well as the topological edge modes.

Overall, our work constitutes key advances in designing organic topological superconductors by the self-assembly of organic metal-free molecules in proximity to the superconducting Pb(111). This could further serve to demonstrate non-Abelian Majorana exchange statistics in supramolecular arrays and possibly form the robust quantum bits required for a topological quantum computer.

# **Conclusion**

THIS dissertation focuses on the investigation of spin-spin and spin-substrate interactions as the fundamental scientific background for the realization of topological qubits. To fulfill this goal, we synthesize spin-carrying nanostructures through various on-surface reactions with different magnetic sources. The subsequent structural and spectral characterization are performed with low-temperature scanning probe microscopy.

First, in Chapter 4, we demonstrate the first synthesis of nanographenes (NGs) directly on the superconducting Ag/Nb(110) substrate. Different products are found at each stage of the reaction. Due to the distinct lattice constant of the thin Ag film and kinetic factors, the reaction pathway deviates from the conventional Ullmann coupling. By fine-tuning of the reaction parameters, we envision the feasibility to fabricate ordered NG structures and couple $\pi$-magnetism with a superconductor.

To ensure the magnetism in nanostructures from $d$-/$f$-shell electrons, we fabricate organometallic (OM) chains using transition metal elements as explored in Chapter 5. By coordinating Fe atoms with pyrene-4,5,9,10-tetraone (PTO) on Ag(111), we observe three spin-flip excitations on Fe due to magnetocrystalline anisotropy (MA). These excitations at small energies are able to be measured even without a decoupling layer, which could be the result of the slight lifting of Fe in the coordinated structure. Furthermore, the consistent dip lineshape around the Fermi level in $dI/dV$ spectra indicates the lateral dispersion of Fe magnetic moments across the PTO-Fe chain, leading to the Fe-Fe coupled spin-flip excitation. By modifying the tip-sample distance, however, does not show clear energy shift for all MA-induced spin-flip excitations, and only one excitation responds to the force imposed by the tip.

In the same chapter, we also show the feasibility to synthesize PTO-Fe chains on the superconducting Pb(111). Through the characterization by a superconducting Pb-tip at 1 K, we observe weak Yu-Shiba-Rusinov (YSR) states as they contribute to

the asymmetric coherence peaks, and two spin-flip excitations. With the preliminary estimation using simulated results of Ag(111), three spin-flip excitations of Fe are very likely on Pb(111), although the one with the smallest energy merges to the coherence peaks. We plan to explore in detail the effect of MA on Pb(111) in the near future.

Chapter 6 covers the investigation of a Shiba lattice fabricated by self-assembled molecular electron acceptors. 4,5,9,10-tetrabromo-1,3,6,8-tetraazapyrene (TBTAP) molecules are deposited on the cold superconducting Pb(111) substrate, which self-assemble into alternating charged and neutral molecular rows. The charge trapped on the molecule can be gated by tip-induced electric field, showing a sharp discharging peak in a d$I$/d$V$ spectrum. On charged TBTAP, Coulomb rings expand and fuse with the neighboring ones as the bias increases, indicating the electron correlation along the charged rows. Most importantly, the resulting YSR bands across the molecular island exhibit low-energy modes in d$I$/d$V$ spectra measured at millikelvin temperatures, which are consistent with signatures of Majorana zero modes.

In conclusion, we explored the structural flexibility of spin lattices through on-surface synthesis. With the measurement by low-temperature STM/AFM, we explore spin-substrate interactions from spin-flip excitations, YSR states, to Majorana zero modes. We further propose several experiments to extend and deepen our research. First, to ensure the $\pi$-magnetism on the superconducting Ag/Nb(110) substrate, triangulene chains are the proper carbon nanostructures for investigation [92]. For the magnetic OM structure, we expect different spin-flip excitations using other transition metal elements, such as Ni or Mn, due to different spin ground states. In addition, we are also interested in how photon-assisted tunneling affect low-energy modes on charged TBTAP molecules. With this approach, it is expected to firmly confirm the existence of Majorana zero modes, and distinguish them from YSR states and the Andreev bound state [199, 200].

# Bibliography

[1] Moore, G. E. Cramming more componentson to integrated circuits. *Proc. IEEE* **86**, 82–85 (2098).

[2] Taiwan Semiconductor Manufacturing Company Limited. 3nm technology. `https://www.tsmc.com/english/dedicatedFoundry/technology/logic/l_3nm` (2023). Accessed: 2023-10-07.

[3] Loss, D. & DiVincenzo, D. P. Quantum computation with quantum dots. *Phys. Rev. A* **57**, 120–126 (1998). URL `https://link.aps.org/doi/10.1103/PhysRevA.57.120`.

[4] Girvin, S. M., Devoret, M. H. & Schoelkopf, R. J. Circuit QED and engineering charge-based superconducting qubits. *Phys. Scr.* **T137**, 014012 (2009). URL `https://doi.org/10.1088/0031-8949/2009/t137/014012`.

[5] Steane, A. The ion trap quantum information processor. *Appl. Phys. B* **64**, 623–643 (1997). URL `https://doi.org/10.1007/s003400050225`.

[6] DiVincenzo, D. P. The physical implementation of quantum computation. *Fortschr. Phys.* **48**, 771–783 (2000). URL `https://doi.org/10.1002/1521-3978(200009)48:9/11<771::aid-prop771>3.0.co;2-e`.

[7] Stern, A. & Lindner, N. H. Topological quantum computation–from basic concepts to first experiments. *Science* **339**, 1179–1184 (2013).

[8] Majorana, E. Teoria simmetrica dell'elettrone e del positrone. *Il Nuovo Cimento* **14**, 171–184 (1937). URL `https://doi.org/10.1007/bf02961314`.

[9] Kitaev, A. Y. Unpaired majorana fermions in quantum wires. *Phys.-Usp.* **44**, 131–136 (2001).

[10] Pawlak, R., Hoffman, S., Klinovaja, J., Loss, D. & Meyer, E. Majorana fermions in magnetic chains. *Progress in Particle and Nuclear Physics* **107**, 1–19 (2019). URL `https://www.sciencedirect.com/science/article/pii/S0146641019300316`.

[11] Moore, G. & Read, N. Nonabelions in the fractional quantum hall effect. *Nucl. Phys. B.* **360**, 362–396 (1991). URL `https://www.sciencedirect.com/science/article/pii/055032139190407O`.

[12] Nayak, C., Simon, S. H., Stern, A., Freedman, M. & Das Sarma, S. Non-abelian anyons and topological quantum computation. *Rev. Mod. Phys.* **80**, 1083–1159 (2008). URL `https://link.aps.org/doi/10.1103/RevModPhys.80.1083`.

[13] Sarma, S. D., Freedman, M. & Nayak, C. Majorana zero modes and topological quantum computation. *npj Quantum Inf.* **1**, 15001 (2015).

[14] Schrade, C. & Fu, L. Majorana superconducting qubit. *Phys. Rev. Lett.* **121** (2018). URL https://doi.org/10.1103/physrevlett.121.267002.

[15] Lutchyn, R. M., Sau, J. D. & Das Sarma, S. Majorana fermions and a topological phase transition in semiconductor-superconductor heterostructures. *Phys. Rev. Lett.* **105**, 077001 (2010). URL https://link.aps.org/doi/10.1103/PhysRevLett.105.077001.

[16] Oreg, Y., Refael, G. & von Oppen, F. Helical liquids and majorana bound states in quantum wires. *Phys. Rev. Lett.* **105**, 177002 (2010). URL https://link.aps.org/doi/10.1103/PhysRevLett.105.177002.

[17] Mourik, V. *et al.* Signatures of majorana fermions in hybrid superconductor-semiconductor nanowire devices. *Science* **336**, 1003–1007 (2012). URL https://doi.org/10.1126/science.1222360.

[18] Klinovaja, J., Stano, P., Yazdani, A. & Loss, D. Topological superconductivity and majorana fermions in RKKY systems. *Phys. Rev. Lett.* **111**, 186805 (2013).

[19] Nadj-Perge, S. *et al.* Observation of Majorana fermions in ferromagnetic atomic chains on a superconductor. *Science* **346**, 602–607 (2014).

[20] Ruby, M. *et al.* End States and Subgap Structure in Proximity-Coupled Chains of Magnetic Adatoms. *Physical Review Letters* **115**, 197204 (2015). URL https://link.aps.org/doi/10.1103/PhysRevLett.115.197204.

[21] Pawlak, R. *et al.* Probing atomic structure and majorana wavefunctions in mono-atomic fe chains on superconducting pb surface. *npj Quantum Inf.* **2**, 16035 (2016).

[22] Jäck, B., Xie, Y. & Yazdani, A. Detecting and distinguishing Majorana zero modes with the scanning tunnelling microscope. *Nature Reviews Physics* **3**, 541–554 (2021). URL https://www.nature.com/articles/s42254-021-00328-z.

[23] Binnig, G., Quate, C. F. & Gerber, C. Atomic force microscope. *Phys. Rev. Lett.* **56**, 930–933 (1986). URL https://link.aps.org/doi/10.1103/PhysRevLett.56.930.

[24] Gross, L. *et al.* High-Resolution Molecular Orbital Imaging Using a $p$-Wave STM Tip. *Phys. Rev. Lett.* **107**, 086101 (2011).

[25] Giessibl, F. J. The qPlus sensor, a powerful core for the atomic force microscope. *Rev. Sci. Instrum.* **90**, 011101 (2019).

[26] Binnig, G., Rohrer, H., Gerber, C. & Weibel, E. Tunneling through a controllable vacuum gap. *Appl. Phys. Lett.* **40**, 178–180 (1982).

[27] Repp, J., Meyer, G., Stojković, S. M., Gourdon, A. & Joachim, C. Molecules on insulating films: Scanning-tunneling microscopy imaging of individual molecular orbitals. *Phys. Rev. Lett.* **94**, 026803 (2005). URL https://doi.org/10.1103/physrevlett.94.026803.

[28] Fernández-Torrente, I., Kreikemeyer-Lorenzo, D., Stróżecka, A., Franke, K. J. & Pas-

cual, J. I. Gating the Charge State of Single Molecules by Local Electric Fields. *Phys. Rev. Lett.* **108**, 036801 (2012). URL https://link.aps.org/doi/10.1103/PhysRevLett.108.036801.

[29] Gonzalez-Lakunza, N. *et al.* Formation of dispersive hybrid bands at an organic-metal interface. *Phys. Rev. Lett.* **100**, 156805 (2008). URL https://link.aps.org/doi/10.1103/PhysRevLett.100.156805.

[30] Li, C. *et al.* Strong signature of electron-vibration coupling in molecules on Ag(111) triggered by tip-gated discharging. *Nat. Commun.* **14**, 5956 (2023). URL https://doi.org/10.1038/s41467-023-41601-2.

[31] Binnig, G., Rohrer, H., Gerber, C. & Weibel, E. Surface studies by scanning tunneling microscopy. *Phys. Rev. Lett.* **49**, 57–61 (1982).

[32] Binnig, G., Rohrer, H., Gerber, C. & Weibel, E. $7 \times 7$ Reconstruction on Si(111) Resolved in Real Space. *Phys. Rev. Lett.* **50**, 120–123 (1983). URL https://link.aps.org/doi/10.1103/PhysRevLett.50.120.

[33] NobelPrize.org. Nobel Prize Outreach AB 2023. The Nobel Prize in Physics 1986. https://www.nobelprize.org/prizes/physics/1986/summary/ (2023). Accessed: 2023-08-26.

[34] Diebold, U., Anderson, J. F., Ng, K.-O. & Vanderbilt, D. Evidence for the tunneling site on transition-metal oxides: $Tio_2(110)$. *Phys. Rev. Lett.* **77**, 1322–1325 (1996). URL https://link.aps.org/doi/10.1103/PhysRevLett.77.1322.

[35] Eigler, D. M. & Schweizer, E. K. Positioning single atoms with a scanning tunnelling microscope. *Nature* **344**, 524–526 (1990). URL https://doi.org/10.1038/344524a0.

[36] Crommie, M. F., Lutz, C. P. & Eigler, D. M. Confinement of electrons to quantum corrals on a metal surface. *Science* **262**, 218–220 (1993). URL https://doi.org/10.1126/science.262.5131.218.

[37] Tersoff, J. & Hamann, D. R. Theory of the scanning tunneling microscope. *Phys. Rev. B* **31**, 805–813 (1985). URL https://link.aps.org/doi/10.1103/PhysRevB.31.805.

[38] Wiesendanger, R. *Scanning Probe Microscopy and Spectroscopy* (Cambridge University Press, 1994). URL https://doi.org/10.1017/cbo9780511524356.

[39] Binnig, G., Rohrer, H., Gerber, C. & Weibel, E. (111) facets as the origin of reconstructed au(110) surfaces. *Surf. Sci. Lett.* **131**, L379–L384 (1983). URL https://www.sciencedirect.com/science/article/pii/0167258483903079.

[40] Kröger, J. *et al.* Surface state electron dynamics of clean and adsorbate-covered metal surfaces studied with the scanning tunnelling microscope. *Prog. Surf. Sci.* **80**, 26–48 (2005). URL https://doi.org/10.1016/j.progsurf.2005.10.002.

[41] Instruments, Z. White Paper: Principles ofl ock-in detection and the state of the art. https://www.zhinst.com/ch/en/resources/principles-of-lock-in-detection (2023). Accessed: 2023-08-31.

[42] Hamers, R. J. Atomic-resolution surface spectroscopy with the scanning tunnel-

ing microscope. *Annual Review of Physical Chemistry* **40**, 531–559 (1989). URL https://doi.org/10.1146/annurev.pc.40.100189.002531. https://doi.org/10.1146/annurev.pc.40.100189.002531.

[43] Heinrich, B. W., Pascual, J. I. & Franke, K. J. Single magnetic adsorbates on s-wave superconductors. *Prog. Surf. Sci.* **93**, 1–19 (2018). URL https://www.sciencedirect.com/science/article/pii/S0079681618300017.

[44] Ruby, M., Heinrich, B. W., Pascual, J. I. & Franke, K. J. Experimental Demonstration of a Two-Band Superconducting State for Lead Using Scanning Tunneling Spectroscopy. *Phys. Rev. Lett.* **114**, 157001 (2015). URL https://link.aps.org/doi/10.1103/PhysRevLett.114.157001.

[45] The Kavli Prize. 2016 KAVLI PRIZE IN NANOSCIENCE. https://www.kavliprize.org/prizes/nanoscience/2016 (2016). Accessed: 2023-09-21.

[46] Giessibl, F. J. Atomic Resolution of the Silicon (111)-(7×7) Surface by Atomic Force Microscopy. *Science* **267**, 68–71 (1995).

[47] Giessibl, F. J. Advances in atomic force microscopy. *Rev. Mod. Phys.* **75**, 949–983 (2003).

[48] Israelachvili, J. N. *Intermolecular and Surface Forces* (Elsevier, 2011), third edition edn.

[49] Giessibl, F. J. Forces and frequency shifts in atomic-resolution dynamic-force microscopy. *Phys. Rev. B* **56**, 16010–16015 (1997). URL https://link.aps.org/doi/10.1103/PhysRevB.56.16010.

[50] Olsson, L., Lin, N., Yakimov, V. & Erlandsson, R. A method for *in situ* characterization of tip shape in ac-mode atomic force microscopy using electrostatic interaction. *J. Appl. Phys.* **84**, 4060–4064 (1998).

[51] Sugimoto, Y. *et al.* Chemical identification of individual surface atoms by atomic force microscopy. *Nature* **446**, 64–67 (2007). URL https://doi.org/10.1038/nature05530.

[52] Gross, L. *et al.* Measuring the charge state of an adatom with noncontact atomic force microscopy. *Science* **324**, 1428–1431 (2009).

[53] Gross, L., Mohn, F., Moll, N., Liljeroth, P. & Meyer, G. The chemical structure of a molecule resolved by atomic force microscopy. *Science* **325**, 1110–1114 (2009).

[54] Chen, C. J. Theory of scanning tunneling spectroscopy. *J. Vac. Sci. Technol. A* **6**, 319–322 (1988). URL https://doi.org/10.1116/1.575444.

[55] Chen, C. J. Tunneling matrix elements in three-dimensional space: The derivative rule and the sum rule. *Phys. Rev. B* **42**, 8841–8857 (1990). URL https://link.aps.org/doi/10.1103/PhysRevB.42.8841.

[56] Gross, L. *et al.* Bond-order discrimination by atomic force microscopy. *Science* **337**, 1326–1329 (2012).

[57] Loth, S., Baumann, S., Lutz, C. P., Eigler, D. M. & Heinrich, A. J. Bistability in atomic-scale antiferromagnets. *Science* **335**, 196–199 (2012).

[58] Stepanow, S. *et al.* Giant spin and orbital moment anisotropies of a cu-phthalocyanine monolayer. *Phys. Rev. B* **82**, 014405 (2010). URL `https://link.aps.org/doi/10.1103/PhysRevB.82.014405`.

[59] Wäckerlin, C. *et al.* Two-dimensional supramolecular electron spin arrays. *Adv. Mater.* **25**, 2404–2408 (2013). URL `https://doi.org/10.1002/adma.201204274`.

[60] Gambardella, P. *et al.* Supramolecular control of the magnetic anisotropy in two-dimensional high-spin Fe arrays at a metal interface. *Nat. Mater.* **8**, 189–193 (2009). URL `https://doi.org/10.1038/nmat2376`.

[61] Pía, A. D. *et al.* Two-dimensional ketone-driven metal-organic coordination on Cu(111). *Chem-Eur J* **22**, 8105–8112 (2016).

[62] Hua, M. *et al.* Highly degenerate ground states in a frustrated antiferromagnetic kagome lattice in a two-dimensional metal–organic framework. *J. Phys. Chem. Lett.* **12**, 3733–3739 (2021).

[63] Mugarza, A. *et al.* Orbital specific chirality and homochiral self-assembly of achiral molecules induced by charge transfer and spontaneous symmetry breaking. *Phys. Rev. Lett.* **105**, 115702 (2010). URL `https://link.aps.org/doi/10.1103/PhysRevLett.105.115702`.

[64] Brune, H. & Gambardella, P. *Fundamentals of Picoscience*, chap. Atomic and Molecular Magnets on Surfaces, 447–470 (CRC Press, Boca Raton, 2013).

[65] Franke, K. J., Schulze, G. & Pascual, J. I. Competition of Superconducting Phenomena and Kondo Screening at the Nanoscale. *Science* **332**, 940–944 (2011). URL `https://doi.org/10.1126/science.1202204`.

[66] Li, R. *et al.* Tuning the spin-related transport properties of FePc on au(111) through single-molecule chemistry. *Chem. Commun.* **54**, 9135–9138 (2018).

[67] Stepanow, S., Lin, N. & Barth, J. V. Modular assembly of low-dimensional coordination architectures on metal surfaces. *J. Phys.: Condens. Matter* **20**, 184002 (2008). URL `https://dx.doi.org/10.1088/0953-8984/20/18/184002`.

[68] Gatteschi, D., Sessoli, R. & Villain, J. *Molecular Nanomagnets* (Oxford University Press, 2006).

[69] Lingenfelder, M. A. *et al.* Towards surface-supported supramolecular architectures: Tailored coordination assembly of 1, 4-benzenedicarboxylate and Fe on Cu(100). *Chem. Eur. J.* **10**, 1913–1919 (2004). URL `https://doi.org/10.1002/chem.200305589`.

[70] Lafferentz, L. *et al.* Controlling on-surface polymerization by hierarchical and substrate-directed growth. *Nat. Chem.* **4**, 215–220 (2012).

[71] Cai, J. *et al.* Atomically precise bottom-up fabrication of graphene nanoribbons. *Nature* **466**, 470–473 (2010).

# Bibliography

[72] Ruffieux, P. *et al.* On-surface synthesis of graphene nanoribbons with zigzag edge topology. *Nature* **531**, 489–492 (2016).

[73] Moreno, C. *et al.* Bottom-up synthesis of multifunctional nanoporous graphene. *Science* **360**, 199–203 (2018). URL `https://www.science.org/doi/10.1126/science.aar2009`.

[74] Kawai, S. *et al.* Atomically controlled substitutional boron-doping of graphene nanoribbons. *Nature Communications* **6**, 8098 (2015). URL `https://www.nature.com/articles/ncomms9098`.

[75] Clair, S. & de Oteyza, D. G. Controlling a Chemical Coupling Reaction on a Surface: Tools and Strategies for On-Surface Synthesis. *Chemical Reviews* **119**, 4717–4776 (2019). URL `https://doi.org/10.1021/acs.chemrev.8b00601`.

[76] Pawlak, R. *et al.* Bottom-up Synthesis of Nitrogen-Doped Porous Graphene Nanoribbons. *Journal of the American Chemical Society* **142**, 12568–12573 (2020). URL `https://doi.org/10.1021/jacs.0c03946`.

[77] Jacobse, P. H., van den Hoogenband, A., Moret, M.-E., Klein Gebbink, R. J. M. & Swart, I. Aryl radical geometry determines nanographene formation on Au(111). *Angew. Chem. Int. Ed.* **55**, 13052–13055 (2016).

[78] Han, P. *et al.* Self-assembly strategy for fabricating connected graphene nanoribbons. *ACS Nano* **9**, 12035–12044 (2015).

[79] de Oteyza, D. G. *et al.* Substrate-independent growth of atomically precise chiral graphene nanoribbons. *ACS Nano* **10**, 9000–9008 (2016).

[80] Simonov, K. A. *et al.* Synthesis of armchair graphene nanoribbons from the 10,10ʹ-dibromo-9,9ʹ-bianthracene molecules on ag(111): the role of organometallic intermediates. *Sci. Rep.* **8**, 3506 (2018).

[81] Jacobse, P. H. *et al.* One precursor but two types of graphene nanoribbons: On-surface transformations of 10,10ʹ-dichloro-9,9ʹ-bianthryl on Ag(111). *J. Phys. Chem. C* **123**, 8892–8901 (2019).

[82] Komeda, T. *et al.* Observation and electric current control of a local spin in a single-molecule magnet. *Nat. Commun.* **2**, 217 (2011). URL `https://doi.org/10.1038/ncomms1210`.

[83] Sessoli, R., Gatteschi, D., Caneschi, A. & Novak, M. A. Magnetic bistability in a metal-ion cluster. *Nature* **365**, 141–143 (1993). URL `https://doi.org/10.1038/365141a0`.

[84] Lieb, E. H. Two theorems on the hubbard model. *Phys. Rev. Lett.* **62**, 1201–1204 (1989).

[85] Wang, W. L., Yazyev, O. V., Meng, S. & Kaxiras, E. Topological frustration in graphene nanoflakes: Magnetic order and spin logic devices. *Phys. Rev. Lett.* **102**, 157201 (2009).

[86] Mishra, S. *et al.* Topological frustration induces unconventional magnetism in a

nanographene. *Nat. Nanotechnol.* **15**, 22–28 (2020). URL `https://www.nature.com/articles/s41565-019-0577-9`.

[87] Mishra, S. *et al.* Collective all-carbon magnetism in triangulene dimers. *Angew. Chem. Int. Ed.* **59**, 12041–12047 (2020).

[88] Sun, Q. *et al.* Coupled spin states in armchair graphene nanoribbons with asymmetric zigzag edge extensions. *Nano Lett.* **20**, 6429–6436 (2020).

[89] Cao, T., Zhao, F. & Louie, S. G. Topological phases in graphene nanoribbons: Junction states, spin centers, and quantum spin chains. *Phys. Rev. Lett.* **119**, 076401 (2017).

[90] Gröning, O. *et al.* Engineering of robust topological quantum phases in graphene nanoribbons. *Nature* **560**, 209–213 (2018).

[91] Rizzo, D. J. *et al.* Topological band engineering of graphene nanoribbons. *Nature* **560**, 204–208 (2018).

[92] Mishra, S. *et al.* Observation of fractional edge excitations in nanographene spin chains. *Nature* **598**, 287–292 (2021). URL `https://www.nature.com/articles/s41586-021-03842-3`.

[93] Kocić, N. *et al.* Periodic Charging of Individual Molecules Coupled to the Motion of an Atomic Force Microscopy Tip. *Nano Lett.* **15**, 4406–4411 (2015). URL `https://doi.org/10.1021/acs.nanolett.5b00711`.

[94] Scott, G. D. & Natelson, D. Kondo Resonances in Molecular Devices. *ACS Nano* **4**, 3560–3579 (2010).

[95] Kondo, J. Resistance minimum in dilute magnetic alloys. *Progress of Theoretical Physics* **32**, 37–49 (1964).

[96] Otte, A. F. *et al.* The role of magnetic anisotropy in the Kondo effect. *Nat. Phys.* **4**, 847–850 (2008).

[97] Ternes, M. Spin excitations and correlations in scanning tunneling spectroscopy. *New J. Phys.* **17**, 063016 (2015).

[98] Kouwenhoven, L. & Glazman, L. Revival of the Kondo effect. *Phys. World* **14**, 33 (2001). URL `https://dx.doi.org/10.1088/2058-7058/14/1/28`.

[99] Haldane, F. D. M. Theory of the atomic limit of the Anderson model. I. Perturbation expansions re-examined. *J. Phys. C: Solid State Phys.* **11**, 5015 (1978). URL `https://dx.doi.org/10.1088/0022-3719/11/24/030`.

[100] Frank, S. & Jacob, D. Orbital signatures of Fano-Kondo line shapes in STM adatom spectroscopy. *Phys. Rev. B* **92**, 235127 (2015).

[101] Gruber, M., Weismann, A. & Berndt, R. The Kondo resonance line shape in scanning tunnelling spectroscopy: instrumental aspects. *J. Phys.: Condens. Matter* **30**, 424001 (2018).

[102] Merino, J. & Gunnarsson, O. Simple model for scanning tunneling spectroscopy of

noble metal surfaces with adsorbed Kondo impurities. *Phys. Rev. B* **69**, 115404 (2004). URL https://link.aps.org/doi/10.1103/PhysRevB.69.115404.

[103] Nagaoka, K., Jamneala, T., Grobis, M. & Crommie, M. F. Temperature dependence of a single Kondo impurity. *Phys. Rev. Lett.* **88**, 077205 (2002). URL https://link.aps.org/doi/10.1103/PhysRevLett.88.077205.

[104] Jacob, D. Renormalization of single-ion magnetic anisotropy in the absence of the Kondo effect. *Phys. Rev. B* **97**, 075428 (2018).

[105] Hirjibehedin, C. F. *et al.* Large magnetic anisotropy of a single atomic spin embedded in a surface molecular network. *Science* **317**, 1199–1203 (2007).

[106] Dzialoshinskii, I. Thermodynamic theory of "weak" ferromagnetismin antiferromagnetic substances. *Sov. Phys. JETP* **5**, 1259–1272 (1957).

[107] Moriya, T. Anisotropic superexchange interaction and weak ferromagnetism. *Phys. Rev.* **120**, 91–98 (1960).

[108] Bode, M. *et al.* Chiral magnetic order at surfaces driven by inversion asymmetry. *Nature* **447**, 190–193 (2007). URL https://doi.org/10.1038/nature05802.

[109] Schlenhoff, A., Krause, S. & Wiesendanger, R. Step-edge-induced anisotropic chiral spin coupling in ultrathin magnetic films. *Phys. Rev. Lett.* **123**, 037201 (2019).

[110] Ruderman, M. A. & Kittel, C. Indirect exchange coupling of nuclear magnetic moments by conduction electrons. *Phys. Rev.* **96**, 99–102 (1954). URL https://link.aps.org/doi/10.1103/PhysRev.96.99.

[111] Kasuya, T. A theory of metallic ferro- and antiferromagnetism on Zener's model. *Prog. Theor. Phys.* **16**, 45–57 (1956). URL https://doi.org/10.1143/ptp.16.45.

[112] Yosida, K. Magnetic Properties of Cu-Mn Alloys. *Phys. Rev.* **106**, 893–898 (1957). URL https://link.aps.org/doi/10.1103/PhysRev.106.893.

[113] Zhou, L. *et al.* Strength and directionality of surface Ruderman–Kittel–Kasuya–Yosida interaction mapped on the atomic scale. *Nat. Phys.* **6**, 187–191 (2010). URL https://doi.org/10.1038/nphys1514.

[114] Bardeen, J., Cooper, L. N. & Schrieffer, J. R. Theory of superconductivity. *Phys. Rev.* **108**, 1175–1204 (1957).

[115] Onnes, H. K. *Commun. Phys. Lab. Univ. Leiden. Suppl.* **29** (1911).

[116] Meissner, W. & Ochsenfeld, R. Ein neuer Effekt bei Eintritt der Supraleitfähigkeit. *Die Naturwissenschaften* **21**, 787–788 (1933).

[117] Abrikosov, A. A. On the magnetic properties of superconductors of the second group. *Sov. Phys. JETP* **5**, 1174–1182 (1957).

[118] Fröhlich, H. Theory of the Superconducting State. I. The Ground State at the Absolute Zero of Temperature. *Phys. Rev.* **79**, 845–856 (1950).

[119] Kivelson, S. A. & Rokhsar, D. S. Bogoliubov quasiparticles, spinons, and spin-charge decoupling in superconductors. *Phys. Rev. B* **41**, 11693–11696 (1990).

[120] Dynes, R. C., Narayanamurti, V. & Garno, J. P. Direct measurement of quasiparticle-lifetime broadening in a strong-coupled superconductor. *Phys. Rev. Lett.* **41**, 1509–1512 (1978).

[121] Bogoliubov, N. N. A new method in the theory of superconductivity. *Sov. Phys. JETP* **34**, 41–46 (1958).

[122] Blonder, G. E., Tinkham, M. & Klapwijk, T. M. Transition from metallic to tunneling regimes in superconducting microconstrictions: Excess current, charge imbalance, and supercurrent conversion. *Phys. Rev. B* **25**, 4515–4532 (1982). URL `https://link.aps.org/doi/10.1103/PhysRevB.25.4515`.

[123] Pannetier, B. & Courtois, H. Andreev reflection and proximity effect. *J. Low Temp. Phys.* **118**, 599–615 (2000).

[124] McMillan, W. L. Tunneling model of the superconducting proximity effect. *Phys. Rev.* **175**, 537–542 (1968).

[125] Yu, L. BOUND STATE IN SUPERCONDUCTORS WITH PARAMAGNETIC IMPURITIES. *Acta Physica Sinica* **21**, 75 (1965). URL `https://doi.org/10.7498/aps.21.75`.

[126] Shiba, H. Classical spins in superconductors. *Progr. Theor. Phys.* **40**, 435–451 (1968). URL `https://doi.org/10.1143/ptp.40.435`.

[127] Rusinov, A. I. Superconductivity near a paramagnetic impurity. *ZhETF Pisma Redaktsiiu* **9**, 146 (1969).

[128] Rusinov, A. I. On the throey of gapless superconductivity in alloys containing paramagnetic impurities. *Sov. J. Exp. Theor. Phys.* **29**, 1101 (1969). URL `http://adsabs.harvard.edu/abs/1969JETP29.1101R`.

[129] Ji, S.-H. *et al.* High-resolution scanning tunneling spectroscopy of magnetic impurity induced bound states in the superconducting gap of pb thin films. *Phys. Rev. Lett.* **100**, 226801 (2008). URL `https://link.aps.org/doi/10.1103/PhysRevLett.100.226801`.

[130] Kezilebieke, S., Žitko, R., Dvorak, M., Ojanen, T. & Liljeroth, P. Observation of Coexistence of Yu-Shiba-Rusinov States and Spin-Flip Excitations. *Nano Lett.* **19**, 4614–4619 (2019). URL `https://doi.org/10.1021/acs.nanolett.9b01583`.

[131] Kamlapure, A. *et al.* Correlation of Yu–Shiba–Rusinov States and Kondo Resonances in Artificial Spin Arrays on an s-Wave Superconductor. *Nano Lett.* **21**, 6748–6755 (2021). URL `https://doi.org/10.1021/acs.nanolett.1c00387`.

[132] Ruby, M., Heinrich, B. W., Peng, Y., von Oppen, F. & Franke, K. J. Wave-Function Hybridization in Yu-Shiba-Rusinov Dimers. *Phys. Rev. Lett.* **120**, 156803 (2018). URL `https://doi.org/10.1103/physrevlett.120.156803`.

[133] Nadj-Perge, S., Drozdov, I. K., Bernevig, B. A. & Yazdani, A. Proposal for realizing

majorana fermions in chains of magnetic atoms on a superconductor. *Phys. Rev. B* **88**, 020407 (2013). URL `https://link.aps.org/doi/10.1103/PhysRevB.88.020407`.

[134] Pientka, F., Glazman, L. I. & von Oppen, F. Topological superconducting phase in helical Shiba chains. *Phys. Rev. B* **88**, 155420 (2013).

[135] Röntynen, J. & Ojanen, T. Topological Superconductivity and High Chern Numbers in 2D Ferromagnetic Shiba Lattices. *Phys. Rev. Lett.* **114**, 236803 (2015). URL `https://link.aps.org/doi/10.1103/PhysRevLett.114.236803`.

[136] Hatter, N., Heinrich, B. W., Ruby, M., Pascual, J. I. & Franke, K. J. Magnetic anisotropy in Shiba bound states across a quantum phase transition. *Nat. Commun.* **6**, 8988 (2015). URL `https://doi.org/10.1038/ncomms9988`.

[137] Matsuura, T. The Effects of Impurities on Superconductors with Kondo Effect. *Prog. Theor. Phys.* **57**, 1823–1835 (1977). URL `https://doi.org/10.1143/ptp.57.1823`.

[138] Liebhaber, E. *et al.* Quantum spins and hybridization in artificially-constructed chains of magnetic adatoms on a superconductor. *Nat. Commun.* **13**, 2160 (2022). URL `http://dx.doi.org/10.1038/s41467-022-29879-0`.

[139] Farinacci, L. *et al.* Tuning the coupling of an individual magnetic impurity to a superconductor: Quantum phase transition and transport. *Phys. Rev. Lett.* **121**, 196803 (2018).

[140] Fu, L. & Kane, C. L. Superconducting Proximity Effect and Majorana Fermions at the Surface of a Topological Insulator. *Phys. Rev. Lett.* **100**, 096407 (2008).

[141] Wang, M.-X. *et al.* The coexistence of superconductivity and topological order in the $Bi_2Se_3$ thin films. *Science* **336**, 52–55 (2012).

[142] Sato, M. & Ando, Y. Topological superconductors: a review. *Rep. Prog. Phys.* **80**, 076501 (2017).

[143] Lutchyn, R. M. *et al.* Majorana zero modes in superconductor–semiconductor heterostructures. *Nature Reviews Materials* **3**, 52–68 (2018). URL `https://www.nature.com/articles/s41578-018-0003-1`.

[144] Zhu, Z. *et al.* Discovery of segmented fermi surface induced by Cooper pair momentum. *Science* **374**, 1381–1385 (2021). URL `https://www.science.org/doi/10.1126/science.abf1077`.

[145] Beenakker, C. Search for Majorana Fermions in Superconductors. *Annu. Rev. Condens. Matter Phys.* **4**, 113–136 (2013). URL `https://doi.org/10.1146/annurev-conmatphys-030212-184337`.

[146] Elliott, S. R. & Franz, M. Colloquium: Majorana fermions in nuclear, particle, and solid-state physics. *Rev. Mod. Phys.* **87**, 137–163 (2015).

[147] Read, N. & Green, D. Paired states of fermions in two dimensions with breaking of parity and time-reversal symmetries and the fractional quantum Hall effect. *Phys. Rev. B* **61**, 10267–10297 (2000). URL `https://link.aps.org/doi/10.1103/PhysRevB.61.10267`.

[148] Sato, M. & Fujimoto, S. Topological phases of noncentrosymmetric superconductors: Edge states, Majorana fermions, and non-Abelian statistics. *Phys. Rev. B* **79**, 094504 (2009). URL `https://link.aps.org/doi/10.1103/PhysRevB.79.094504`.

[149] Jäck, B. *et al.* Observation of a majorana zero mode in a topologically protected edge channel. *Science* **364**, 1255–1259 (2019). URL `http://dx.doi.org/10.1126/science.aax1444`.

[150] Palacio-Morales, A. *et al.* Atomic-scale interface engineering of Majorana edge modes in a 2D magnet-superconductor hybrid system. *Sci. Adv.* **5**, eaav6600 (2019). URL `https://www.science.org/doi/10.1126/sciadv.aav6600`.

[151] Kezilebieke, S. *et al.* Topological superconductivity in a van der Waals heterostructure. *Nature* **588**, 424–428 (2020).

[152] Bazarnik, M. *et al.* Antiferromagnetism-driven two-dimensional topological nodal-point superconductivity. *Nat. Commun.* **14**, 614 (2023). URL `https://doi.org/10.1038/s41467-023-36201-z`.

[153] Soldini, M. O. *et al.* Two-dimensional Shiba lattices as a possible platform for crystalline topological superconductivity. *Nat. Phys.* 1–7 (2023). URL `https://doi.org/10.1038/s41567-023-02104-5`.

[154] Pawlak, R. *et al.* Gate-tunable topological superconductivity in a supramolecular electron spin lattice (2023). URL `https://arxiv.org/abs/2310.18134`.

[155] Li, J. *et al.* Two-dimensional chiral topological superconductivity in Shiba lattices. *Nat. Commun.* **7**, 12297 (2016). URL `https://www.nature.com/articles/ncomms12297`.

[156] Rachel, S., Mascot, E., Cocklin, S., Vojta, M. & Morr, D. K. Quantized charge transport in chiral Majorana edge modes. *Phys. Rev. B* **96**, 205131 (2017). URL `https://link.aps.org/doi/10.1103/PhysRevB.96.205131`.

[157] ScientaOmicron. LT STM III: Ultimate SPM Performance Below 5 K. `https://scientaomicron.com/Downloads/Brochures/SPM/LT_STM_III_SO_Brochure.pdf` (2021). Accessed: 2023-08-11.

[158] ScientaOmicron. TESLA JT SPM Low Temperatures and Variable Magnetic Fields. `https://scientaomicron.com/Downloads/Brochures/SPM/TESLA_JT_SPM_SO_Brochure.pdf`. Accessed: 2023-08-14.

[159] Balashov, T., Meyer, M. & Wulfhekel, W. A compact ultrahigh vacuum scanning tunneling microscope with dilution refrigeration. *Rev. Sci. Instrum.* **89**, 113707 (2018).

[160] Lide, D. R. & Frederikse, H. P. R. (eds.) *CRC Handbook of Chemistry and Physics* (CRC Press, 1997), 78 edn.

[161] Tomanic, T., Schackert, M., Wulfhekel, W., Sürgers, C. & v. Löhneysen, H. Two-band superconductivity of bulk and surface states in Ag thin films on Nb. *Phys. Rev. B* **94**, 220503 (2016). URL `https://link.aps.org/doi/10.1103/PhysRevB.94.220503`.

[162] Odobesko, A. B. *et al.* Preparation and electronic properties of clean superconducting

Nb(110) surfaces. *Phys. Rev. B* **99**, 115437 (2019). URL `https://link.aps.org/doi/10.1103/PhysRevB.99.115437`.

[163] Razinkin, A. S. & Kuznetsov, M. V. Scanning tunneling microscopy (STM) of low-dimensional NbO structures on the Nb(110) surface. *Phys. Met. Metall.* **110**, 531–541 (2010).

[164] Zhussupbekov, K. *et al.* Oxidation of Nb(110): atomic structure of the NbO layer and its influence on further oxidation. *Sci. Rep.* **10**, 3794 (2020).

[165] Reinert, F., Nicolay, G., Schmidt, S., Ehm, D. & Hüfner, S. Direct measurements of the *l*-gap surface states on the (111) face of noble metals by photoelectron spectroscopy. *Phys. Rev. B* **63**, 115415 (2001). URL `https://link.aps.org/doi/10.1103/PhysRevB.63.115415`.

[166] Rizzo, D. J. *et al.* Inducing metallicity in graphene nanoribbons via zero-mode superlattices. *Science* **369**, 1597–1603 (2020).

[167] Mishra, S. *et al.* Topological Defect-Induced Magnetism in a Nanographene. *JACS* **142**, 1147–1152 (2020). URL `https://doi.org/10.1021/jacs.9b09212`.

[168] Li, J. *et al.* Single spin localization and manipulation in graphene open-shell nanostructures. *Nat. Commun.* **10**, 200 (2019). URL `https://www.nature.com/articles/s41467-018-08060-6`.

[169] Río, E. C.-d. *et al.* Observation of Yu-Shiba-Rusinov States in Superconducting Graphene. *Adv. Mater.* **33**, 2008113 (2021). URL `https://onlinelibrary.wiley.com/doi/abs/10.1002/adma.202008113`.

[170] Högl, P., Frank, T., Kochan, D., Gmitra, M. & Fabian, J. Chiral Majorana fermions in graphene from proximity-induced superconductivity. *Physical Review B* **101**, 245441 (2020). URL `https://link.aps.org/doi/10.1103/PhysRevB.101.245441`.

[171] Schulz, F. *et al.* Precursor geometry determines the growth mechanism in graphene nanoribbons. *J. Phys. Chem. C* **121**, 2896–2904 (2017). URL `https://doi.org/10.1021/acs.jpcc.6b12428`.

[172] Neaton, J. B., Hybertsen, M. S. & Louie, S. G. Renormalization of Molecular Electronic Levels at Metal-Molecule Interfaces. *Phys. Rev. Lett.* **97**, 216405 (2006). URL `https://link.aps.org/doi/10.1103/PhysRevLett.97.216405`.

[173] Schneider, L. *et al.* Magnetism and in-gap states of 3d transition metal atoms on superconducting Re. *npj Quantum Materials* **4**, 1–8 (2019). URL `https://www.nature.com/articles/s41535-019-0179-7`.

[174] Küster, F. *et al.* Correlating Josephson supercurrents and Shiba states in quantum spins unconventionally coupled to superconductors. *Nature Communications* **12**, 1108 (2021). URL `https://www.nature.com/articles/s41467-021-21347-5`.

[175] Eichhorn, J. *et al.* On-Surface Ullmann Coupling: The Influence of Kinetic Reaction Parameters on the Morphology and Quality of Covalent Networks. *ACS Nano* **8**, 7880–7889 (2014). URL `https://doi.org/10.1021/nn501567p`.

[176] Ternes, M. Spin-Gui-1.0 (2015).

[177] Choi, T., Ruggiero, C. D. & Gupta, J. A. Tunneling spectroscopy of ultrathin insulating $Cu_2N$ films, and single Co adatoms. *J. Vac. Sci. Technol. B* **27**, 887–890 (2009). URL `http://dx.doi.org/10.1116/1.3010720`.

[178] Loth, S. *et al.* Controlling the state of quantum spins with electric currents. *Nat. Phys.* **6**, 340–344 (2010). URL `http://dx.doi.org/10.1038/NPHYS1616`.

[179] Czap, G. *et al.* Probing and imaging spin interactions with a magnetic single-molecule sensor. *Science* **364**, 670–673 (2019). URL `https://www.science.org/doi/abs/10.1126/science.aaw7505`. `https://www.science.org/doi/pdf/10.1126/science.aaw7505`.

[180] Verlhac, B. *et al.* Atomic-scale spin sensing with a single molecule at the apex of a scanning tunneling microscope. *Science* **366**, 623–627 (2019). URL `http://dx.doi.org/10.1126/science.aax8222`.

[181] Wäckerlin, C. *et al.* Role of the magnetic anisotropy in atomic-spin sensing of 1d molecular chains. *ACS Nano* **16**, 16402–16413 (2022). URL `http://dx.doi.org/10.1021/acsnano.2c05609`.

[182] Heinrich, B. W., Braun, L., Pascual, J. I. & Franke, K. J. Protection of excited spin states by a superconducting energy gap. *Nat. Phys.* **9**, 765–768 (2013).

[183] Vaxevani, K. *et al.* Extending the spin excitation lifetime of a magnetic molecule on a proximitized superconductor. *Nano Lett.* **22**, 6075–6082 (2022).

[184] Hoffman, S., Klinovaja, J., Meng, T. & Loss, D. Impurity-induced quantum phase transitions and magnetic order in conventional superconductors: Competition between bound and quasiparticle states. *Phys. Rev. B* **92**, 125422 (2015). URL `http://dx.doi.org/10.1103/PhysRevB.92.125422`.

[185] Kügel, J. *et al.* Relevance of Hybridization and Filling of 3d Orbitals for the Kondo Effect in Transition Metal Phthalocyanines. *Nano Lett.* **14**, 3895–3902 (2014). URL `http://dx.doi.org/10.1021/nl501150k`.

[186] Shockley, W. On the Surface States Associated with a Periodic Potential. *Phys. Rev.* **56**, 317–323 (1939). URL `https://link.aps.org/doi/10.1103/PhysRev.56.317`.

[187] Bürgi, L., Petersen, L., Brune, H. & Kern, K. Noble metal surface states: deviations from parabolic dispersion. *Surf. Sci.* **447**, L157–L161 (2000). URL `https://www.sciencedirect.com/science/article/pii/S0039602899011024`.

[188] Würde, K., Mazur, A. & Pollmann, J. Surface electronic structure of Pb(001), Pb(110), and Pb(111). *Phys. Rev. B* **49**, 7679–7686 (1994). URL `https://link.aps.org/doi/10.1103/PhysRevB.49.7679`.

[189] Ménard, G. C. *et al.* Two-dimensional topological superconductivity in Pb/-Co/Si(111). *Nat. Commun.* **8**, 2040 (2017). URL `https://www.nature.com/articles/s41467-017-02192-x`.

[190] Wang, Z. *et al.* Evidence for dispersing 1D Majorana channels in an iron-based super-

conductor. *Science* **367**, 104–108 (2020). URL `https://www.science.org/doi/10.1126/science.aaw8419`.

[191] Hapala, P. *et al.* Mechanism of high-resolution STM/AFM imaging with functionalized tips. *Phys. Rev. B* **90**, 085421 (2014). URL `https://link.aps.org/doi/10.1103/PhysRevB.90.085421`.

[192] Cohen, A. J., Mori-Sánchez, P. & Yang, W. Insights into current limitations of density functional theory. *Science* **321**, 792–794 (2008). URL `https://doi.org/10.1126/science.1158722`.

[193] Fernández-Torrente, I., Franke, K. J. & Pascual, J. I. Vibrational Kondo Effect in Pure Organic Charge-Transfer Assemblies. *Physi. Rev. Lett.* **101**, 217203 (2008). URL `https://link.aps.org/doi/10.1103/PhysRevLett.101.217203`.

[194] Teichmann, K. *et al.* Controlled Charge Switching on a Single Donor with a Scanning Tunneling Microscope. *Phys. Rev. Lett.* **101**, 076103 (2008). URL `https://link.aps.org/doi/10.1103/PhysRevLett.101.076103`.

[195] Fatayer, S. *et al.* Reorganization energy upon charging a single molecule on an insulator measured by atomic force microscopy. *Nat. Nanotechnol.* **13**, 376–380 (2018). URL `https://www.nature.com/articles/s41565-018-0087-1`.

[196] Li, H. *et al.* Imaging local discharge cascades for correlated electrons in WS2/WSe2 moiré superlattices. *Nat. Phys.* **17**, 1114–1119 (2021). URL `https://www.nature.com/articles/s41567-021-01324-x`.

[197] Liu, J.-C. *et al.* Proximity-Induced Superconductivity in Atomically Precise Nanographene on Ag/Nb(110). *ACS Mater. Lett.* **5**, 1083–1090 (2023). URL `https://doi.org/10.1021/acsmaterialslett.2c00955`.

[198] Kawai, S. *et al.* Three-dimensional graphene nanoribbons as a framework for molecular assembly and local probe chemistry. *Sci. Adv.* **6**, eaay8913 (2020). URL `https://doi.org/10.1126/sciadv.aay8913`.

[199] González, S. A. *et al.* Photon-assisted resonant Andreev reflections: Yu-Shiba-Rusinov and Majorana states. *Phys. Rev. B* **102**, 045413 (2020). URL `https://link.aps.org/doi/10.1103/PhysRevB.102.045413`.

[200] Peters, O. *et al.* Resonant Andreev reflections probed by photon-assisted tunnelling at the atomic scale. *Nat. Phys.* **16**, 1222–1226 (2020). URL `https://doi.org/10.1038/s41567-020-0972-z`.

# Nomenclature

## Symbols

### Latin letters

| | |
|---|---|
| $A$ | Oscillation amplitude |
| $A_H$ | Hamaker constant |
| $A_{mod}$ | Lock-in modulation amplitude |
| $A_{set}$ | Amplitude setpoint |
| $a, b$ | Lattice parameters |
| $D$ | Axial anisotropy |
| $d$ | Distance |
| $E$ | Energy / Transverse anisotropy |
| $E_{bond}$ | Bonding energy |
| $E_F$ | Fermi level |
| $e$ | Elementary charge |
| $e^-$ | Electron |
| $F$ | Force |
| $F_{chem}$ | Chemical bonding force |
| $F_{el}$ | Electrostatic force |
| $F_{ts}$ | Total tip-sample force |
| $F_{vdW}$ | Van der Waals force |
| $f_{mod}$ | Lock-in modulation frequency |
| $f_0$ | Eigenfrequency |
| $g$ | Gyromagnetic ratio |
| $H_c$ | Critical magnetic field |

## Nomenclature

| | |
|---|---|
| $I$ | Tunneling current |
| $I_t$ | Current setpoint |
| $J_K$ | Kondo coupling strength |
| $J_{ij}$ | Spin-spin coupling strength |
| $k_B$ | Boltzmann constant |
| $k_{ts}$ | Stiffness parameter |
| $m^*$ | Effective mass of electron |
| $R$ | Radius of curvature of the tip |
| $\vec{r}$ | Tip position |
| $\vec{r_0}$ | Initial tip position |
| $S_0$ | Spin ground state |
| $T$ | Temperature |
| $T_c$ | Critical temperature |
| $T_K$ | Kondo temperature |
| $t$ | Hopping exchange |
| $U$ | Electrostatic potential difference |
| $V$ | Bias voltage |
| $V_{LJ}$ | Lennard-Jones potential |
| $V_{thresh}$ | Discharging threshold voltage |
| $X$ | Coordinate of one horizontal axis in the sample surface plane |
| $Y$ | Coordinate of one horizontal axis in the sample surface plane |
| $Z$ | Coordinate of the vertical axis between tip and sample |
| $z$ | Tip-sample distance |

## Greek letters

| | |
|---|---|
| $\alpha$ | Lever arm |
| $\gamma_{ts}$ | Normalized frequency shift |
| $\Delta$ | Superconducting pairing strength |
| $\Delta f$ | Frequency shift |
| $\Delta Z$ | The offset of the tip height |
| $\epsilon_0$ | Vercuum permittivity |
| $\varepsilon$ | Energy position on a tunneling spectrum |
| $\kappa$ | Inverse decay length of the wavefunction in vacuum |

| | |
|---|---|
| $\lambda$ | Force interaction range |
| $\rho$ | Electron density of states |
| $\sigma$ | Equilibrium distance |
| $\phi$ | Work function |
| $\varphi$ | Surface wavefunction |
| $\xi$ | Coherence length |
| $\Psi$ | Electronic states |
| $\omega$ | Angular frequency of the oscillation |

# Abbreviations

| | |
|---|---|
| AC | Alternative current |
| AFM | Atomic force microscopy/microscope |
| AM | Amplitude-modulation |
| BCC | Body-centered cubic |
| BCS | Bardeen-Cooper-Schrieffer |
| CCM | Constant current mode |
| CHM | Constant height mode |
| DBBA | 10,10'-**dib**romo-9,9'-**b**ianthr**a**cene |
| DBTJ | Double barrier tunnel junction |
| DFT | Density functional theory |
| DMI | Dzyaloshinskii-Moriya interaction |
| DOS | Density of states |
| FCC | Face-centered cubic |
| FM | Frequency-modulation |
| GNR | Graphene nanoribbon |
| HOMO | Highest occupied molecular orbital |
| HWHM | Half width at half-maximum |
| LDOS | Local density of states |
| LUMO | Lowest unoccupied molecular orbital |

## Nomenclature

| | |
|---|---|
| MA | Magnetocrystalline anisotropy |
| MBS | Majorana bound state |
| ML | Monolayer |
| MPc | Metal phthalocyanine |
| MZM | Majorana zero mode |
| NG | Nanographene |
| OM | Organometallic |
| PLL | Phase-locked loop |
| PTO | **P**yrene-4,5,9,10-**t**etra**o**ne |
| QD | Quantum dot |
| qubit | Quantum bit |
| RF | Radio frequency |
| RKKY | Ruderman-Kittel-Kasuya-Yosida |
| SC | Superconducting |
| SMM | Single molecule magnet |
| SOC | Spin-orbit coupling |
| SOMO | Singly occupied molecular orbital |
| SPM | Scanning probe microscopy/microscope |
| STM | Scanning tunneling microscopy/microscope |
| STS | Scanning tunneling spectroscopy |
| SUMO | Singly unoccupied molecular orbital |
| TBTAP | 4,5,9,10-**t**etra**b**romo-1,3,6,8-**t**etra**a**za**p**yrene |
| TCNQ | Tetracyanoquinodimethane |
| TSC | Topological superconductivity |
| UHV | Ultra-high vacuum |
| YSR | Yu-Shiba-Rusinov |
| ZZ | Zigzag |
| 1D | One-dimensional |
| 2D | Two-dimensional |

# Acknowledgements

L AST but not least, I would like to thank all the people who have accompanied me through the four-year PhD study. Thank you for all the scientific discussion, excursion, adventures, and private talks. All of these make my journey in Switzerland unforgettable.

I would like to give a special thank to Prof. Ernst Meyer. Thank you for having me in your group. I really enjoyed working in such a pleasant environment. Through working in the SPM lab in the past four years, I became more certain about my interest in exploring science. I feel lucky to have you as a supervisor in my early stage of research. Being part of Nanolino group is the decision I have never regretted.

I also want to thank Dr. Rémy Pawlak, who closely supervised my PhD project. Thank you for being so patient with my questions and quest for scientific discussion. I really liked topics of experiments you prepared for me, they were versatile, having the potential to be extended and deepened. It was really enjoyable when doing these experiments. I want to thank you for proofreading my manuscript, and guiding me through the daunting process for publishing the first paper. Your encouraging words and patience have strengthened my confidence in academic work. You are not only a supervisor, but also a mentor and a friend. It was always pleasant to work with you.

I would like to thank Prof. Katharina J. Franke for accepting to be the external expert of my defense, and the evaluation of the dissertation. Also thank Prof. Martino Poggio for being my second supervisor, and completing the commission of the committee member.

I would further like to thank Prof. em. Dr. Silvio Decurtins and Dr. Shi-Xia Liu from University of Bern, who provide us interesting molecules to work on and feedback from the chemistry aspect. A thank also goes to Dr. Ping Zhou for synthesizing DBBA and PTO molecules for us. My PhD thesis could not be completed without your support.

## Acknowledgements

My great gratitude also goes to Prof. Wulf Wulfhekel from Karlsruhe Institute of Technology, who gave me the opportunity to use their microscope to improve my experimental results. Thank you for providing insightful advices in experiments and the reply to referees. I also want to thank Dr. Hongyan Chen for helping me finish the measurement with the millikelvin STM. I learned a lot of tips about sample preparation from you. The time we spent together in Karlsruhe was unforgettable.

I want to thank Yves Pellmont for building the RF heater, which made the development of Ag/Nb substrate possible. Also thanks to Roland Steiner for building the crane for assembling JT-STM/AFM. Without you, many of the measurements could not be done. The engineering support from you has relieved lots of burden in the research work.

Additionally, I want to thank Nataliia Voievoda, the former program manager of QUSTEC. Thank you for initiating the QUSTEC program, and organizing on-line and off-line activities throughout the pandemic. I have met many excellent fellows and friends through this program. My thank also goes to QUSTEC fellows who organized summer schools in Engelberg and in Freiburg. It was enjoyable to learn science and have fun with you all.

I would also like to express my thank to LT team. Thank you Dr. Carl Drechsel and Dr. Philipp D'Astolfo for introducing me to the LT-STM/AFM upon my arrival, and for your patience in showing me how to perform the measurement. I also want to mention Dr. Chao Li and Outhmane Chahib, my current colleagues in the LT lab. Thank you for the support in the laboratory work and the discussion in scientific questions.

A great thank of course goes to all the members in Nanolino group. Thank you Dr. Alexina Ollier for being such heart-warming and caring that I was able to integrate myself into the group in a short time. Thank you Dr. Fabien Sanchez for organizing many fun activities. Paul Hiret, thank you for the reminder of taking a rest. It was interesting to have some discussion in non-scientific topics with you. Also all the other group members, my life in Basel could not be so exciting without you. In addition, I would like to mention Germaine Weaver and Barbara Kammermann, thank you for managing my visa before my arrival, and answering my administrative questions.

With this opportunity, I want to express my thank to all the friends I have made during the past four years. It was a lot of fun joining those hikes, ski trips, barbecue, picnics, and drinks after work. I really enjoyed my "Adventure Time" in Switzerland.

Lastly, I would like to show my great gratitude to my family, which is my biggest support for this journey. I know I always have you at my back. Although we are now separated by 15 hours of flight, some warm messages or photos always brighten my day. Thank you for supporting my decision of pursuing a doctoral degree.

# List of Publications & Communications

## Peer-reviewed Journal Publications

1. Pawlak, R.; Liu, X.; Ninova, S.; D'Astolfo, P.; Drechsel, C.; **Liu, J.-C.**; Häner, R.; Decurtins, S.; Aschauer, U.; Liu, S.-X.; Meyer, E. On-Surface Synthesis of Nitrogen-Doped Kagome Graphene. *Angew. Chem. Int. Ed.* **60,** 15, 8370-8375 (2021). DOI: 10.1002/anie.202016469

2. Drechsel, C.; D'Astolfo, P.; **Liu, J.-C.**; Glatzel, T.; Pawlak, R.; Meyer, E. Topographic signatures and manipulations of Fe atoms, CO molecules and NaCl islands on superconducting Pb(111). *Beilstein J. Nanotechnol.* **13**, 1-3 (2022). DOI: 10.3762/bjnano.13.1

3. Pawlak, R.; Anindya, K.; Shimizu, T.; **Liu, J.-C.**; Sakamaki, T.; Shang, R.; Rochefort, A.; Nakamura, E.; Meyer, E. Atomically precise incorporation of BN doped rubicene into graphene nanoribbons. *J. Phys. Chem. C* **126**, 19726-19732 (2022). DOI: 10.1021/acs.jpcc.2c05866

4. **Liu, J.-C.**; Pawlak. R.; Wang, X.; D'Astolfo, P.; Drechsel, C.; Zhou, P.; Decurtins, S.; Aschauer, U.; Liu, S.-X.; Wulfhekel, W.; Meyer, E. Proximity-Induced Superconductivity in Atomically Precise Nanographene. *ACS Materials Lett.* **5**, 1083-1090 (2023). DOI: 10.1021/acsmaterialslett.2c00955

5. Li, C.; Kaspar, C.; Zhou, P.; **Liu, J.-C.**; Chahib, O.; Glatzel, T.; Häner, R.; Aschauer, U.; Decurtins, S.; Liu, S.-X.; Thoss, M.; Meyer, E.; Pawlak, R. Strong signature of electron-vibration coupling in molecules on Ag(111) triggered by tip-gated discharging *Nat. Commun.* **14**, 5956 (2023). DOI: 10.1038/s41467-023-41601-2

6. Pawlak, R.; **Liu, J.-C.**; Li, C.; Hess, R.; Chen, H.; Drechsel, C.; Zhou, P.; Häner, R.; Aschauer, U.; Glatzel, T.; Decurtins, S.; Loss, D.; Klinovaja, J.; Liu, S.-X.; Wulfhekel, W.; Meyer, E. Gate-tunable topological superconductivity in a

supramolecular electron spin lattice. *Under review.* arXiv: 2310.18134v2

7. Chahib, O.; Yin, Y.; **Liu, J.-C.**; Li, C.; Glatzel, T.; Ding, F.; Yuan, Q.; Meyer, E.; Pawlak, R. Probing charge redistribution at the interface of self-assembled cyclo-P5 pentamers on Ag(111). *Under review* arXiv: 2401.12612

8. **Liu, J.-C.**; Li, C.; Chahib, O.; Wang, X.; Zhou, P.; Häner, R.; Decurtins, S.; Aschauer, U.; Liu, S.-X.; Meyer, E.; Pawlak, R. Spin-flip Excitations in Organometallic Chains. *Paper under preparation.*

# Talks

1. Graphene Nanoribbon Synthesis on the Superconducting Ag/Nb(110) substrate. **Liu, J.-C.**; Pawlak. R.; Wang, X.; D'Astolfo, P.; Drechsel, C.; Zhou, P.; Decurtins, S.; Aschauer, U.; Liu, S.-X.; Wulfhekel, W.; Meyer, E. *QCQT seminar*, 2020-12-15, virtual.

2. On-surface synthesis of graphene nanoribbons on the superconducting Ag/Nb(110) substrate. **Liu, J.-C.**; Pawlak. R.; Wang, X.; D'Astolfo, P.; Drechsel, C.; Zhou, P.; Decurtins, S.; Aschauer, U.; Liu, S.-X.; Wulfhekel, W.; Meyer, E. *Joint Annual Meeting of ÖPG and SPS 2021*, 2021-08-30, Innsbruck, Austria.

3. On-surface synthesis of magnetic organometallic chains on the superconducting Ag/Nb(110) substrate. **Liu, J.-C.**; Li, C.; Chahib, O.; Wang, X.; Zhou, P.; Häner, R.; Decurtins, S.; Aschauer, U.; Liu, S.-X.; Meyer, E.; Pawlak, R. *DPG Fall Meeting: Condensed Matter Section 2021*, 2021-09-26, virtual.

4. On-surface Chemistry on Proximity-induced Superconductors. **Liu, J.-C.**; Pawlak. R.; Wang, X.; D'Astolfo, P.; Drechsel, C.; Zhou, P.; Decurtins, S.; Aschauer, U.; Liu, S.-X.; Wulfhekel, W.; Meyer, E. *molCH 2022*, 2022-06-10, Bern, Switzerland.

5. Proximity-Induced Superconductivity in Atomically Precise Nanographene. **Liu, J.-C.**; Pawlak. R.; Wang, X.; D'Astolfo, P.; Drechsel, C.; Zhou, P.; Decurtins, S.; Aschauer, U.; Liu, S.-X.; Wulfhekel, W.; Meyer, E. *Novel 2D materials explored via scanning probe microscopy & spectroscopy*, 2022-06-20, San Sebastian, Spain.

6. Proximity-Induced Superconductivity in Atomically Precise Nanographene. **Liu, J.-C.**; Pawlak. R.; Wang, X.; D'Astolfo, P.; Drechsel, C.; Zhou, P.; Decurtins, S.; Aschauer, U.; Liu, S.-X.; Wulfhekel, W.; Meyer, E. *The 23$^{rd}$ International Conference on Non-contact Atomic Force Microscopy*, 2022-08-01, Nijmegen, the Netherlands.

7. Proximity-induced superconductivity in magnetic molecules. **Liu, J.-C.**; Li, C.; Chen, H.; Drechsel, C.; Zhou, P.; Häner, R.; Aschauer, U.; Glatzel, T.; Decurtins, S.; Liu, S.-X.; Loss, D.; Klinovaja, J.; Wulfhekel, W.; Meyer, E.; Pawlak, R. *QCQT seminar*, 2022-10-18, Basel, Switzerland.

8. A two dimensional array of radical molecules on Pb(111). **Liu, J.-C.**; Li, C.; Chen, H.; Drechsel, C.; Zhou, P.; Häner, R.; Aschauer, U.; Glatzel, T.; Decurtins, S.; Liu, S.-X.; Loss, D.; Klinovaja, J.; Wulfhekel, W.; Meyer, E.; Pawlak, R. *DPG Spring Meeting: Condensed Matter Section 2023*, 2023-03-27, Dresden, Germany.

9. Spin-flip Excitation in Organometallic Chains. **Liu, J.-C.**; Li, C.; Chahib, O.; Wang, X.; Zhou, P.; Häner, R.; Decurtins, S.; Aschauer, U.; Liu, S.-X.; Meyer, E.; Pawlak, R. *The 24$^{th}$ International Conference on Non-contact Atomic Force Microscopy*, 2023-09-25, Singapore.

10. Spin-flip Excitation in Organometallic Chains. **Liu, J.-C.**; Li, C.; Chahib, O.; Wang, X.; Zhou, P.; Häner, R.; Decurtins, S.; Aschauer, U.; Liu, S.-X.; Meyer, E.; Pawlak, R. *DPG Spring Meeting: Condensed Matter Section 2024*, 2024-03-18, Berlin, Germany.

## Posters

1. On-surface synthesis of graphene nanoribbons on the superconducting Ag/Nb(110) substrate. **Liu, J.-C.**; Pawlak. R.; Wang, X.; D'Astolfo, P.; Drechsel, C.; Zhou, P.; Decurtins, S.; Aschauer, U.; Liu, S.-X.; Wulfhekel, W.; Meyer, E. *DPG Spring Meeting: Surface Science 2021*, 2021-03-01, virtual.

2. On-surface synthesis of graphene nanoribbons on the superconducting Ag/Nb(110) substrate. **Liu, J.-C.**; Pawlak. R.; Wang, X.; D'Astolfo, P.; Drechsel, C.; Zhou, P.; Decurtins, S.; Aschauer, U.; Liu, S.-X.; Wulfhekel, W.; Meyer, E. *Swiss NanoConvention 2021*, 2021-06-24, virtual.

3. Fabrication of Kondo Lattice via On-surface Reactions. **Liu, J.-C.**; Li, C.; Chahib, O.; Wang, X.; Zhou, P.; Häner, R.; Decurtins, S.; Aschauer, U.; Liu, S.-X.; Meyer, E.; Pawlak, R. *SAOG Meeting 2023*, 2023-02-03, Fribourg, Switzerland.

4. Fabrication of magnetic lattice via on surface reactions. **Liu, J.-C.**; Li, C.; Chahib, O.; Wang, X.; Zhou, P.; Häner, R.; Decurtins, S.; Aschauer, U.; Liu, S.-X.; Meyer, E.; Pawlak, R. *DPG Spring Meeting: Condensed Matter Section 2023*, 2023-03-27, Dresden, Germany.